TECHNISCHE UNIVERSITÄT WIEN

DIPLOMARBEIT

Synthesis and electrochemical characterization of mesoporous Nb_2O_5 films

Ausgeführt am Institut für
Materialchemie
der Technischen Universität Wien

unter der Anleitung von Univ.Prof. Mag.rer.nat. Dr.rer.nat. Dominik Eder, Univ.Prof. Dipl.-Phys. Dr.rer.nat. Jürgen Fleig und Projektass.(FWF) Dipl.-Ing. Maximilian Morgenbesser

durch
Ralf Jagenteufel, BSc

Wien, am 6. November 2019

_____
Unterschrift (Student)

Acknowledgement

First of all, I would like to thank Dominik Eder who gave me the possibility to work in his great research group and to write my master thesis about this interesting topic. Thanks for supervising the preparative part of my work and coming up with ideas I should investigate in more detail as well as improving my written thesis. I am also very grateful for the opportunity to work as a tutor and for your patience with my slow writing progress.

Furthermore I want to thank Jürgen Fleig for the collaboration with his research group, providing the possibility to conduct electrochemical test as well as for the interpretation and help in analyzing the generated data. Another person I would greatly like to thank is my supervisor for the electrochemical part of my work, Max Morgenbesser, for guiding me through the electrode preparation, measurement setup design and electrochemical characterization. I am also very thankful for the time spent together discussing the data, the written text of my thesis and formulations. Thanks for reading my thesis more than three times and discussing it in detail to improve not only the data preparation and comprehensibility but also style and readability.

I would also like to thank Annette Foelske-Schmitz for the opportunity to use the Profilometer, Hinrich Grothe for the cooperation to measure contact angle, Richard Barna for the fabrication and analysis of the batches D, E, F and G, Leonie Deilmann for helping me with my first syntheses, Ariane Giesriegl for the TEM measurements, Jia Wang and Paolo Rudatis for the SEM measurements and the whole research group for the spirit of community, apparent when eating together at lunchtime and passing on relevant information as well. In addition, I appreciate all the small conversations, which brightened my days, especially those with Jasmin Schubert.

Without my family in the background, helping me financially and encouraging me to take a break long enough to rehabilitate my health when my body showed me my physical boundaries, I would not be standing at the end of my studies now.

Finally, to finish my thesis I am very grateful for the feedback and correction of my thesis by Paolo Rudatis and Sebastian Steiner and of my presentation by Hanna Gureczny, who is always there when I need her, brightening up my days with her smile and her love.

Contents

Nomenclature

3D	Three-dimensional
Al_2O_3	Aluminum oxide, sapphire single crystal
Au	Gold
BSE	Backscattered electrons
DIC	Differential interference contrast
Ea	Activation energy
EISA	Evaporation-induced self-assembly
EIS	Electrochemical impedance spectroscopy
EJ/yr	exajoule per year (1 EJ is roughly 24 Mtoe)
EO	Ethylene oxide, C_2H_4O
EtOH	Ethanol, C_2H_5OH
FTO	Fluorine doped tin oxide
IEA	International energy agency
magn.	Magnificatioin
$mbar$	$Millibar, 10^{-3}bar$
Mg	Magnesium
$MgCl_2$	Magnesium chloride
MgO	Magnesium oxide
μm	Micro meters, 10^{-6} m
Mtoe	million tons of oil equivalents
Na	Sodium
$NaCl$	Sodium chloride
nm	Nano meters, 10^{-9} m
Nb	Niobium
P123	Pluronic® P-123 triblock copolymer $EO_{20}PO_{70}EO_{20}$
PO	Propylene oxide, C_3H_6O
RH	Relative humidity

rpm	Rounds per minute
R	Resistance
RT	Room temperature
s	Seconds
SC	Spin coating
SDA	Structure directing agent
SDGs	Sustainable development goals
SEM	Scanning electron microscopy
SE	Secondary electrons
σ	Effective conductivity
TEM	Transmission electron microscopy
TGA	Thermal gravimetric analysis
T	Temperature

Abstract

Fundamental investigations on photochemical and electronic properties of photocatalytically active electrodes require well-defined model systems. We designed ordered mesoporous thin films with uniform pore size distributions and homogeneous pore structures by combining a sol-gel process with evaporation induced self assembly (EISA) and spin coating to synthesize mesoporous Nb_2O_5 thin films on substrates for electrochemical characterization. The thin film production was optimized tuning the precursor solution and parameters like spin coating speed, relative humidity level during solvent evaporation and furnace temperature.

The main aim of this work and the reason for using mesoporous films was to eliminate contact resistance with the electrode while allowing a maximum interface with the surrounding gas phase. This concept could be proved by impedance spectra featuring one semicircle solely.

We found that temperatures above 350 °C led to a linear increase of resistance over time. According to our hypothesis this is due to a diffusion process of oxygen vacancies $V_{O_{Surf}}^{\bullet\bullet}$ originally located at the surface into the bulk material as well as due to the surface reaction $4e^- + V_O^{\bullet\bullet} + O_{2_{(g)}} = O_O + O_{(ads)}^{2-}$[62]. By consuming electrons as well as oxygen vacancies the amount of free charge carriers is reduced, thus increasing the measured impedance. By altering the measurement conditions we found that UV-irradiation, p_{O_2} variation and humidity level strongly influence σ_{eff}. This opens not only the field of photocatalytically active electrodes but also humidity and gas sensing as possible fields of application for the studied material.

1 Introduction

Over the last fifty years the global population has reached new maxima both in numbers and growth. The global footprint network [46] recently found that the global ecological footprint correlates with these figures, as can be seen in figure 1. The green line shows the amount of resources the earth can renew within one year due to the planets biological capacity. This mark has been surpassed in the early 1970ies.

In 2009, J. Rockström et al. defined nine planetary boundaries within which they expected that humanity can oparate safely [55]. Steffen et al. updated the data in 2015 and implemented a zone of uncertainty with increasing risk between the safe green zone and the red zone of high risk [56]. This revised graph can be seen in figure 2.

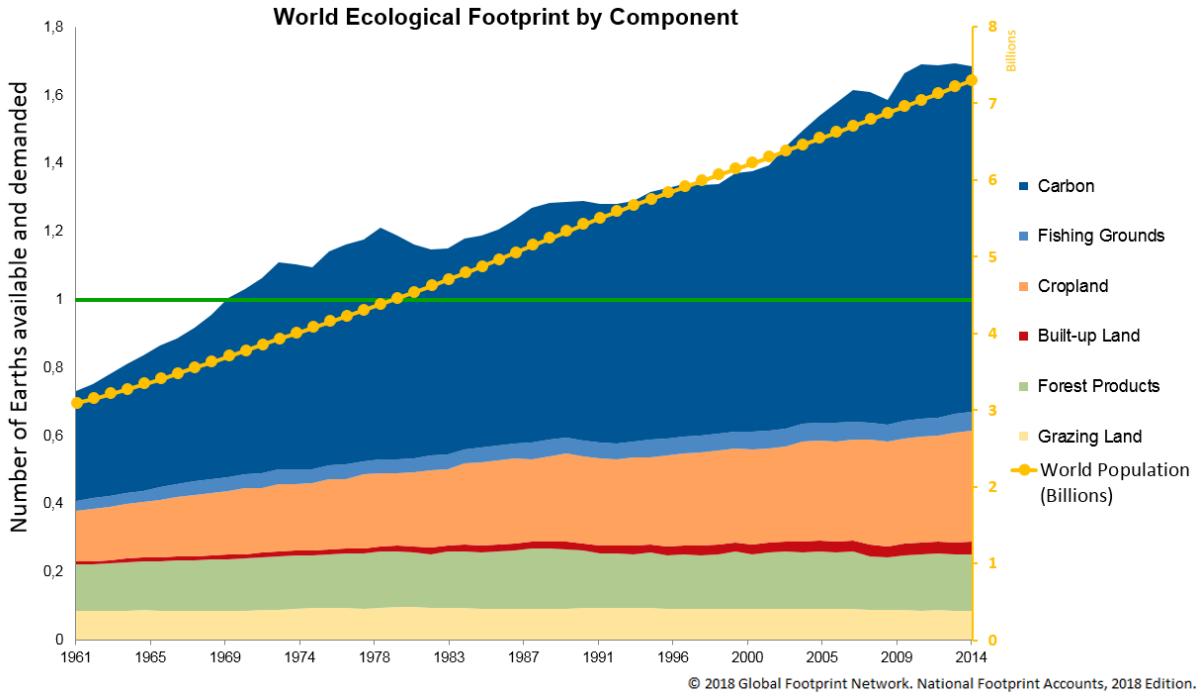

Figure 1: The global ecological footprint is rising alongside the population growth. [46]

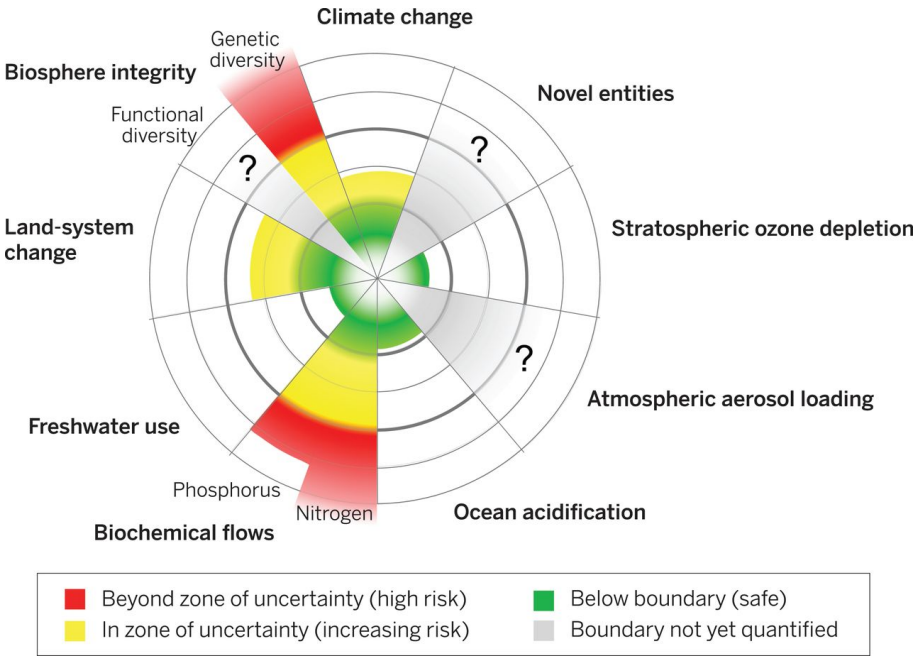

Figure 2: The nine planetary boundaries according to Steffen et al. [56]

To overcome the problem of crossing planetary boundaries while ensuring that all people have the possibility to fulfill their needs, Kate Raworth developed the "Doughnut of social and planetary boundaries" [52] in 2012, presented in figure 3 along with the update in 2017, where the current status of our planet by Steffen et al. is displayed simultaneously.

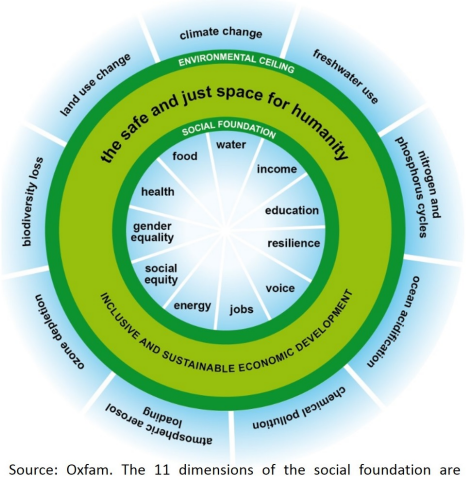

Source: Oxfam. The 11 dimensions of the social foundation are illustrative and are based on government's priorities for Rio+20. The nine dimensions of the environmental ceiling are based on the planetary boundaries set out by Rockström et al (2009b)

(a) a first illustration by Kate Raworth in 2012 [52]

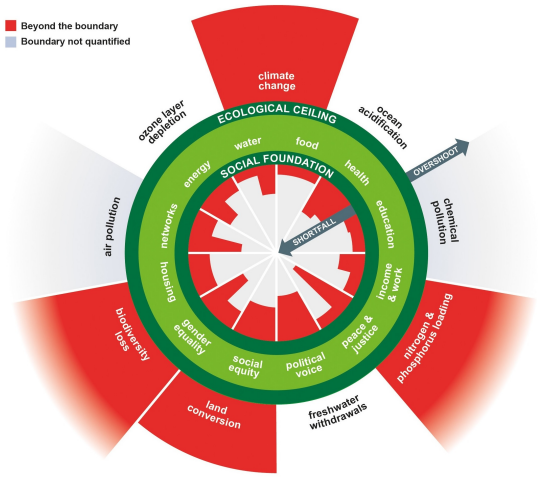

Image: Kate Raworth and Christian Guthier/The Lancet Planetary

(b) status quo of april 2017 [8]

Figure 3: A safe and just space for humanity to thrive in

Figure 3 b illustrates, that we are currently not facing climate change as a single challenge, but many problems at the same time, especially on the social sector. Therefore, the

United Nations Development Programme formed 17 individual Sustainable Development Goals (SDGs) in 2015 as successor of the Millenium Development Goals [5] as a call for action to all countries in the world, see figure 4.

Figure 4: The 17 Sustainable Development Goals, adopted by all United Nations member states in 2015 [5].

1.1 SDG #7 - affordable and clean energy

The subgoal number seven aims for universal access to affordable, reliable and modern energy services for everyone by 2030 by substantially increasing the share of renewable energy in the global energy mix and by improving energy efficiency [4]. The International Energy Agency (IEA) created a model of the future energy system which meets the total primary energy demand as well as the SDGs. The graph presented in figure 5 illustrates that a tremendous increase of renewable energy production has to take place within the next decade.

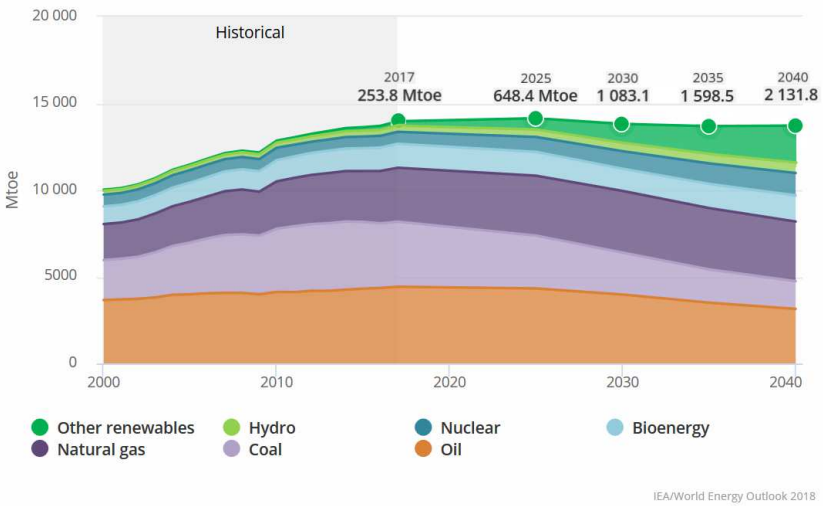

Figure 5: World total primary energy demand in the Sustainable Development scenario (million tons of oil equivalents, Mtoe) [7].

Renewable energy sources include bioenergy, oceanic activity, hydropower, geothermal energy, wind power and solar energy. According to the renewables global futures report [53], the renewable energy supply would exceed the primary energy demand of 2007 by a factor of 1.5 or higher (up to 50) if the total technical potential is used, see

the shades of grey in figure 6. The conversion factor of exajoule to million tons of oil equivalents is roughly 24 [1].

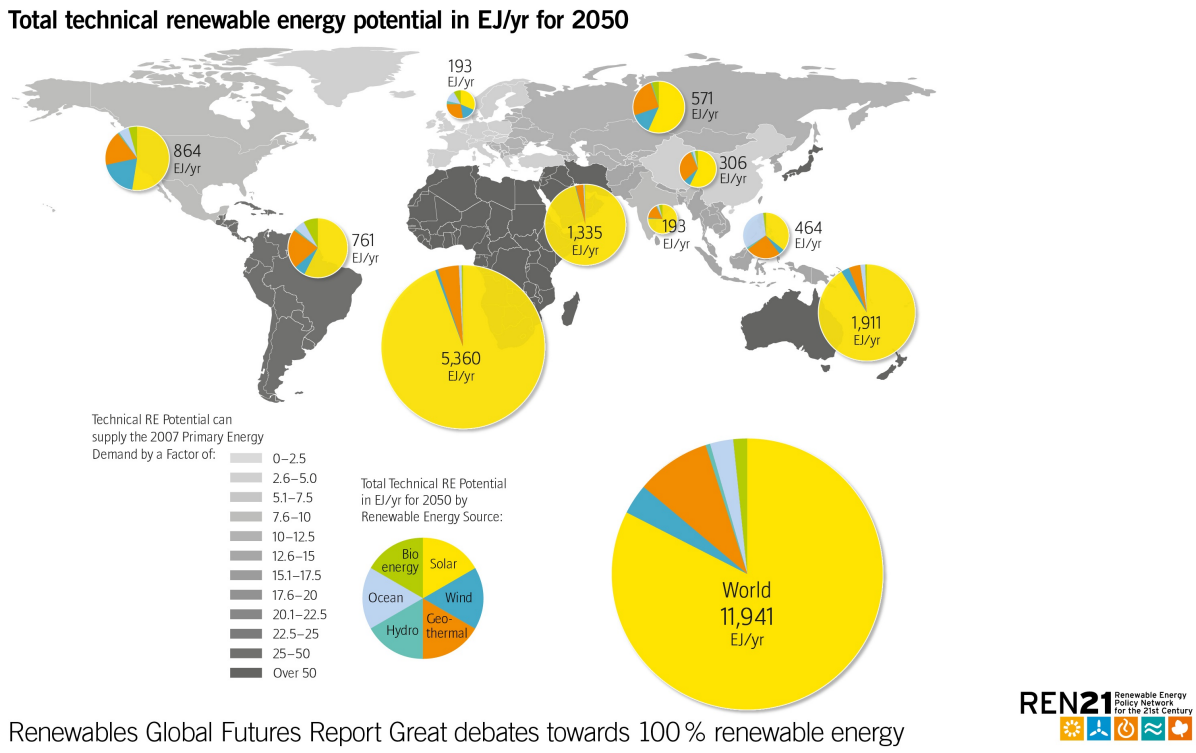

Source: IPCC-SRREN, Figure 10.19 I (Preceding pages)
Note:[2] The technical RE potentials reported here represent total worldwide and regional potentials based on a review of studies published before 2009 by Krewitt et al. (2009). They do not deduct any potential already utilized for energy production. Due to methodological differences and accounting methods among studies, these estimates cannot be strictly compared across technologies and regions, nor in terms of primary energy demand. Technical RE potential analyses published after 2009 show higher results in some cases but are not included in this figure. Some RE technologies may compete for land, possibly lowering the overall RE potential. Scenario data: IEA WEO 2009 Reference scenario (International Energy Agency (IEA), 2009; Teske et al., 2010), ReMIND-RECIPE 450ppm Stabilization Scenario (Luderer et al., 2009), MiniCAM EMF22 1st-best 2.6 W/2 Overshoot Scenario (Calvin et al., 2009), Advanced Energy (R)evolution 2010 (Teske et al., 2010).

Figure 6: Total technical renewable energy potential in exajoule per year (EJ/yr) for 2050 [53].

Figure 6 illustrates that the majority of the energy can be harvested by using the solar source. Besides the improvement of the well known techniques of solar thermal power plants and photovoltaic systems, the research interest nowadays focuses on the approach of storing energy in chemical bonds. This opens the field of artificial photosynthesis and photocatalysis (described in chapter 1.2) among others [20], as can be seen in figure 7.

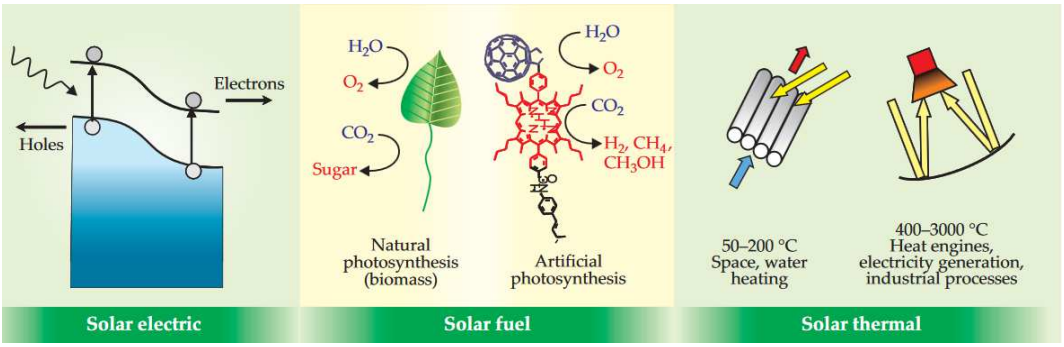

Figure 7: Solar energy conversion [20]

1.2 Photocatalysis

The term artificial photosynthesis is generally used for the various approaches of mimicking natural photosynthesis to use photo-generated electrons and holes to drive chemical reactions, thus converting solar energy into chemical energy [65]. The products can range from solar fuels like hydrogen, methane or methanole to more complex organic compunds with higher value and price. The concepts currently studied include complete inorganic mechanisms as well as biochemistry using microorganisms [15].

According to Gust et. al., artificial photosynthetic fuel production systems "require antenna/reaction center complexes to harvest sunlight and generate electrochemical potential, catalysts for oxidation of water or other electron sources, and catalysts for reduction of precursors to hydrogen or reduced carbon." [34] Therefore, the solar fuel production can be achieved in separate devices like photovoltaic electricity generation and electrocatalytic hydrogen evolution or in one device like photocatalytic water splitting or the combination called photoelectrocatalysis, illustrated in figure 8.

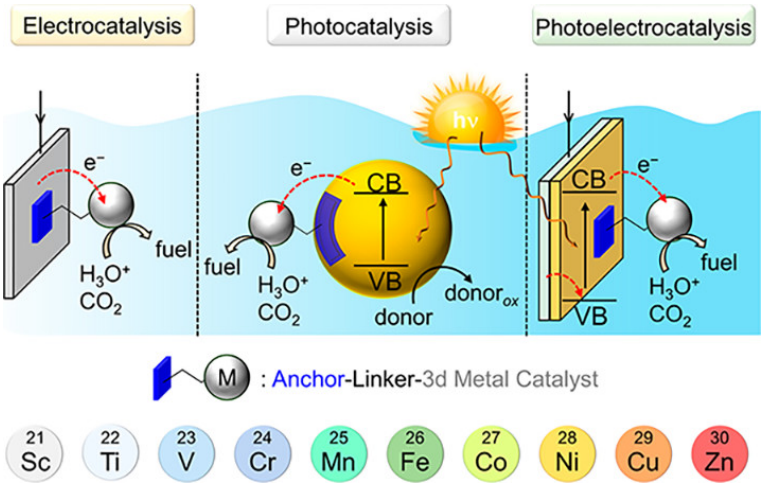

Figure 8: Solar fuel production by electrocatalysis, photocatalysis and photoelectrocatalysis [21].

Apart from fuel production, photocatalysis can be used in any field, as it is generally considered as the catalysis of a photochemical reaction at a solid surface, usually a semiconductor [26] with suitable band gap. Catalysis itself was defined by Ostwald in 1894 [49] as acceleration of a slow reaction by the presence of a foreign material, the catalyst **C**, which is not consumed. The acceleration is achieved by providing an alternative reaction pathway via intermediate I', presented in figure 9 (a), thus reducing the activation energy.

In a photocatalyzed reaction R→P, figure 9 (c), the non-consumed photocatalyst **C** is effective only in the excited state (**C***) and activates reagent **R** through a chemical reaction, such as transfer of an atom or an electron. Therefore, **C*** reacts to **C** and an intermediate **I** is formed (a radical or radical ion), which regenerates **C**, giving **I'** before building the end product **P** [51].

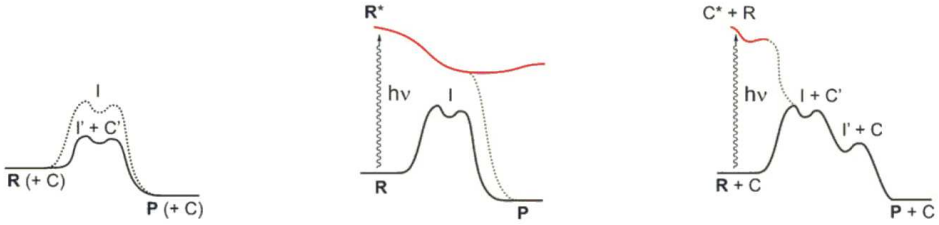

(a) Thermal catalyis (b) Photochemical reaction (c) Photocatalysis

Figure 9: Energy paths followed (a) in a thermal reaction (R→P) catalyzed by **C** via intermediate **I'**; (b) in a photochemical reaction (the chemical reaction starts from the excited state surface of the reagent **R***); (c) in a photocatalyzed reaction (the catalyst **C** is active only after being excited to state **C***) [51].

1.3 Motivation & Aim

In artificial photosynthesis and photocatalysis a high surface area is crucial to achieve high efficiency through high yields, respectively activity and rates. High surface can be accomplished by inducing pores and reducing particle size. In most cases, the formation of nanoparticles yields powdered samples that are dispersed in the reaction medium to drive the photocatalytic processes. Such powder-based systems suffer from several limitations. For example, they tend to agglomerate to minimize surface energies, thus reducing the accessible surface area for catalytic turn-over; furthermore, their recovery from solution is impeded by their small size. One strategy to overcome these challenges is to support the nanoparticles on substrates, ideally in the form of thin, porous films.

Another challenge is to control and tune particle size, defect structure and morphology of particulate systems. In particular fundamental investigations of photochemical and electronic properties as well as unravelling of kinetic details and mechanistic steps require well-defined model systems.

Ordered mesoporous thin films with uniform pore size distributions and homogeneous pore structures can serve as ideal model systems

In the present work, I aimed to grow such systems directly on substrates for subsequent fundamental electronic and electrochemical investigations and focused on Nb_2O_5 as a promising photocatalytically active electrode.

In more detail, my objective was to uncover the key parameters/processes responsibe for the formation of fissures, e.g. precursor solution, coating procedure, solvent evaporation, heating conditions, type of furnace and atmosphere. I further aimed to design thin films on substrates suitable for electrochemical studies, where the internal interface is negligible small compared to the surface-gas-interface (surface conduction), thus eliminating the contact resistance with the electrode. I aimed to evaluate these films for their potential application in sensors or photocatalysis, using a measurement setup for impedance spectroscopy [38] to study the samples under different conditions like vacuum, UV and p_{O_2} variation.

1.4 Terminology

Within the current work I used the following terms according to Merriam-Webster dictionary [3] to describe the different shapes and sizes of cracks in thin films:

Fracture	the result of breaking - the complete separation of the parts, here wide cracks extending from one end of the sample to the other
Crack	a break without complete separation of parts, here small cracks not penetrating the whole sample
Fissure	a narrow opening or crack of considerable length and depth, here narrow cracks, starting at a crack nucleation point and ending in a small distance
Crack-free	a film of good quality without any fractures, cracks or fissures
Slit	a long narrow cut or opening, here the space between the electrodes
Scratch	a mark or injury produced by scratching, here the cracks produced by the tweezer in order to measure the film thickness by profilometry

2 Theory

2.1 Mesoporous materials

The pores of solids materials can be classified in macropores (bigger than 50 nm), mesopores (between 2 nm and 50 nm) and micropores (smaller than 2 nm), according to IUPAC [35].

Nowadays, mesoporous materials are used for many applications in everyday life like batteries [43] or solar cells [32]. These can be produced by a wide variety of preparation methods, for example sonochemical, microwave, electrochemical, hydrothermal and sol-gel, among others [39]. According to M. E. Davis, uniformity within the pore size, shape and volume in porous materials is crucial for the respective application [23].

2.1.1 Structure directing agent vs. hard templates

Hard templates In **hard templating** usually macroscopic structures like fibers, films, powders, porous monolithic objects or discrete particles are filled or coated with the precursor, as decribed in figure 10 [50]. Examples for hard templates include (nano)carbons, SiO_2, Al_2O_3, zeolites and many more.

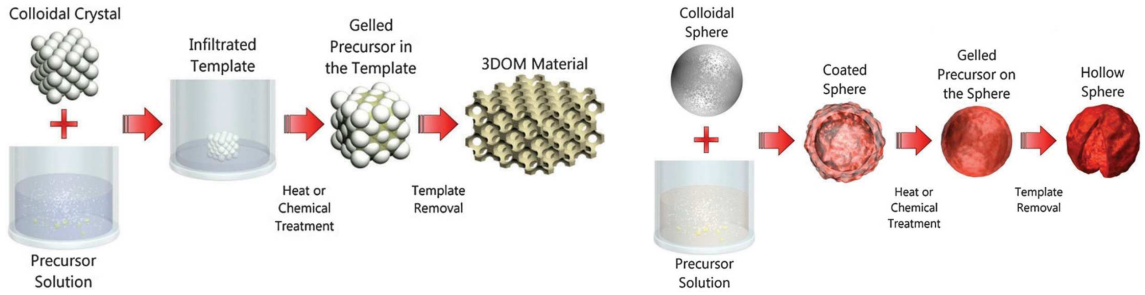

(a) Hard templating using an infiltration process

(b) Hard templating conducted via a coating process

Figure 10: Schemes detailing two examples of hard templating processes [50].

For the transformation of the precursor into a solid-phase material via sol-gel process, a chemical or thermal treatment is performed, usually followed by a consolidation step at temperatures above 300 °C in order to increase the degree of condensation and remove residual solvent. Generally, a shrinkage of roughly 20-40 % takes place and some metal oxides crystallize. Subsequently, the template is removed either thermally or by dissolution in acids or organic solvents, depending on the material. [50] While hard templating produces the exact replica of the template with good control of the pore size and relatively low pore shrinkage, it is limited to relatively small pore sizes and difficulties like incomplete infiltration or template residues even after multiple etching steps can be challenging.

Soft templates The **soft templating** route via structure directing agents (SDA) is based on the self-assembly of a solution containing micelle-creating surfactants, precursor, and solvent molecules. Self-assembly is described as a spontaneous process, where noncovalent interactions like electrostatic forces, Van der Waals forces, $\pi - \pi$ interactions, hydrogen bonding, etc. are the driving force [17].

Above the critical micelle concentration, micelles are formed, whose shape are dependent on the structure of the surfactant molecule, in the case of amphiphilic block copolymers on the relative volume fraction of the hydrophilic and hydrophobic polymer blocks, illustrated in figure 11.

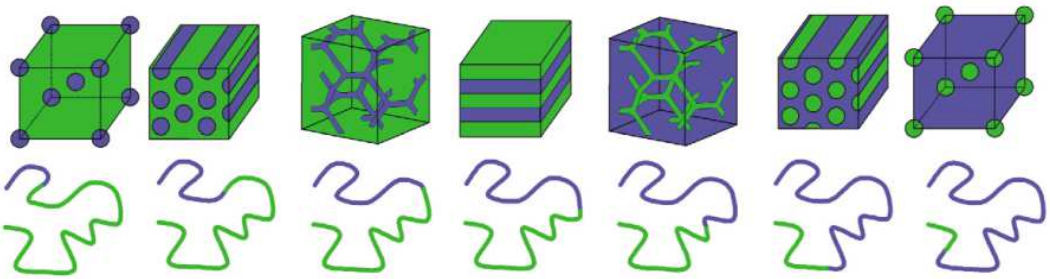

Figure 11: Different structures formed by a AB block copolymer according to the approximate chain length (volume fraction) of the A and B block. [61]

The micelle structures can be tuned by external alterations like addition of salts (NaCl, MgCl, ...) which influence the packing parameter or by dissolving hydrocarbons that cause the micelle cores to swell [50] as well as by the ratio of precursor to surfactant itself, as presented in figure 12.

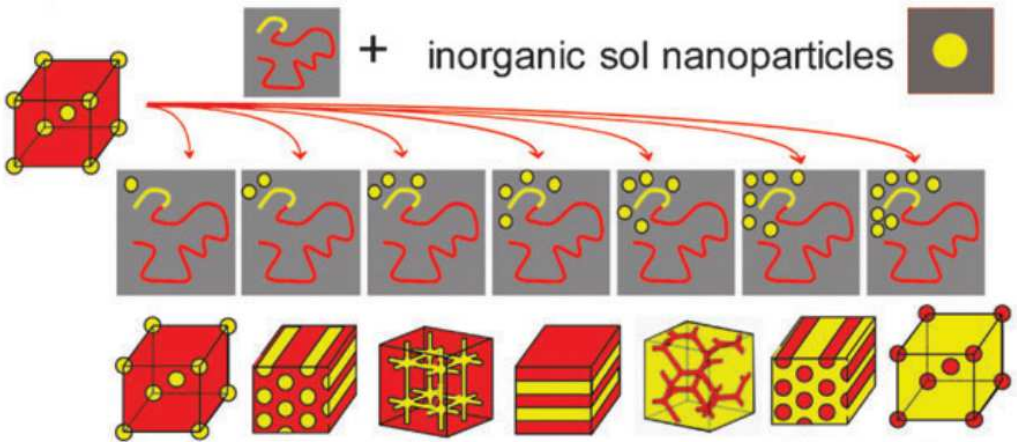

Figure 12: Different structures formed by the same AB block copolymer according to the amount of inorganic sol nanopartices selectively swelling one block of the copolymer. [48]

The mesostructure formation either occurs via the simultaneous assembly of the precursor and surfactant (coopearative assembly), or involving the formation of a liquid crytalline phase before the condensation of the inorganic network (true liquid crystal templating), or is driven by the evaporation of a volatile solvent (evaporation-induced self-assembly, EISA) [25]. The three main soft templating pathways are presented in figure 13.

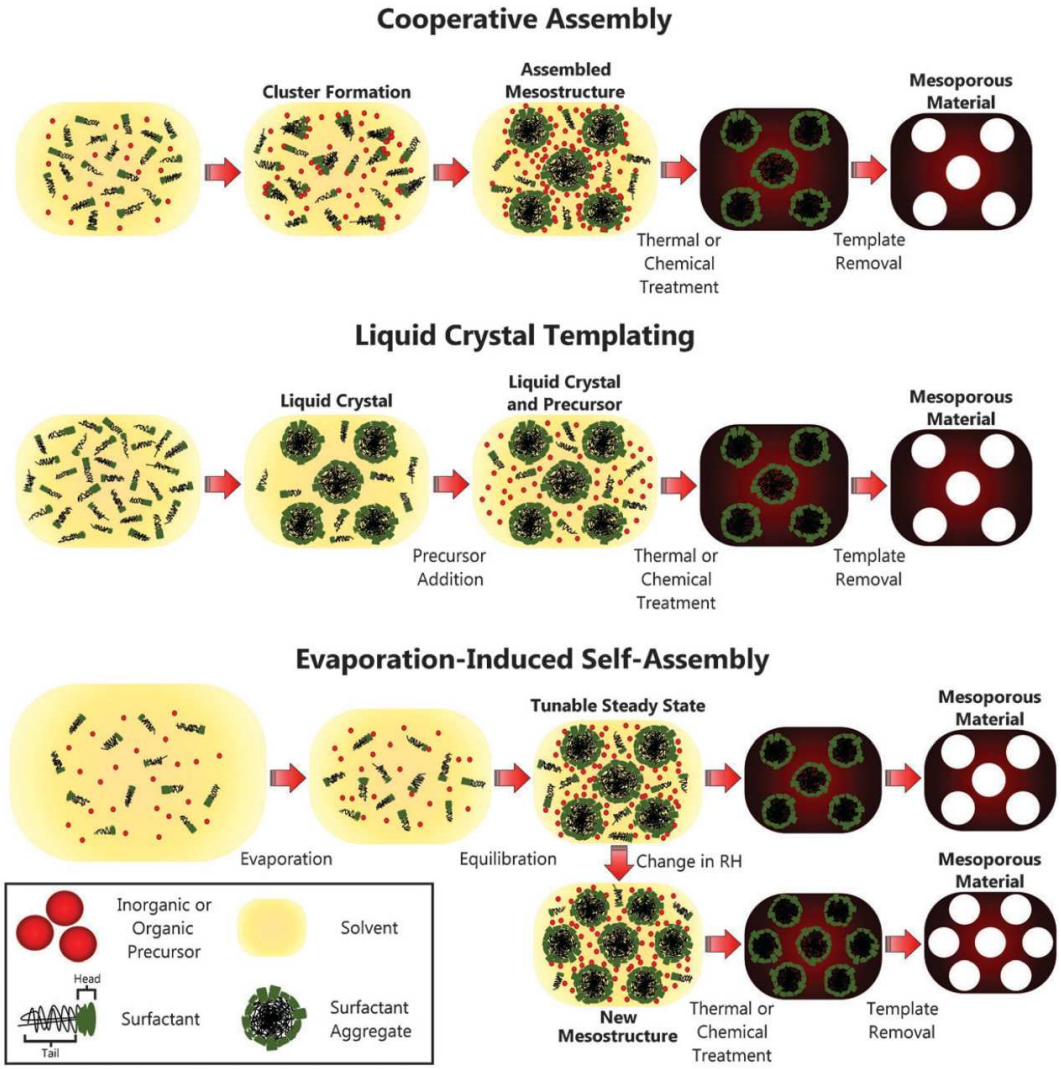

Figure 13: Schemes detailing the soft templating processes "cooperative assembly" (top), "liquid crystal templating" (middle) and "evaporation-induced self-assembly" (bottom) [50].

After the transformation and optional consolidation, similar to hard templating, the template is removed by a low-temperature chemical treatment, combustion (calcination) or depolymerization (pyrolysis) with the consequence of pore shrinkage and crystallite

growth [50]. Shrinkage in soft templating is usually stronger compared to hard templating and can be decreased for example by combined assembly by soft and hard chemistries (CASH) [42]. While commercially available surfactants like Pluronic® are limited to pore sizes around 4-7 nm, with special tailored polymers pore sizes up to 40 nm and advanced 3D structures like gyroids can be produced [24]. With SDAs it is more challenging to obtain uniform pore diameters, but soft templating routes are more flexible in diameter range, pore structure and choice of material.

In this thesis a soft templating synthesis route with EISA is used, where the amphiphilic triblock copolymer Pluronic® P123 $EO_{20}PO_{70}EO_{20}$ serves as SDA. For the EISA process the polymer is dissolved in a volatile solvent, since the evaporation is slowly increasing the polymer precursor concentration, which leads to the formation of micelles above the critical micelle concentration. In this manner, a three-dimensional (3D) network is formed, according to the relative volume fraction of the PEO and PPO blocks, due to the interaction of (enthalpic) interfacial energy and (entropic) chain stretching forces [61]. The assembly and evaporation kinetics are very sensible to the solvent vapor pressure which makes the process very complex but tuneable in many ways.

According to the phase diagram presented in figure 14, the micelles assemble in a hexagonal geometry in the region of 40 to 80 wt% in pure P123 diluted in water, but as mentioned the addition of inorganic sol shifts the geometries to lower weight fractions.

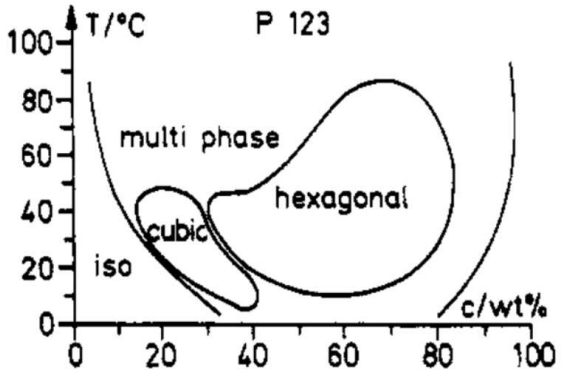

Figure 14: Phase diagram of the Pluronic® P123 surfactant ($EO_{20}PO_{70}EO_{20}$) [60]

2.2 Niobium pentoxide Nb_2O_5

Niobium oxides exist in various stochiometries with different polymorphs. According to Bauer et al. the different niobium oxides NbO, NbO_2 and Nb_2O_5 are stable in small homogeneous regions, for example Nb_2O_5-$Nb_2O_{4.8}$ [16]. While pure stoichiometric Nb_2O_5 is an insulator, the slightly reduced $Nb_2O_{5-\delta}$ is classified as a metal-excess, n-type semiconductor with an activation energy of 1.65 eV [33]. Greener et al. investigated the oxygen partial pressure of the conductivity and found the following empirical relation $\sigma = p_{O_2}^{-0.24\pm0.01}$ in

the temperature range of 300 to 900 °C of specimen sintered at 1300 °C [33]. The temperature treatment leads to the formation of one of the many different crystallographic modifications, presented in figure 15, depending on the synthesis procedure.

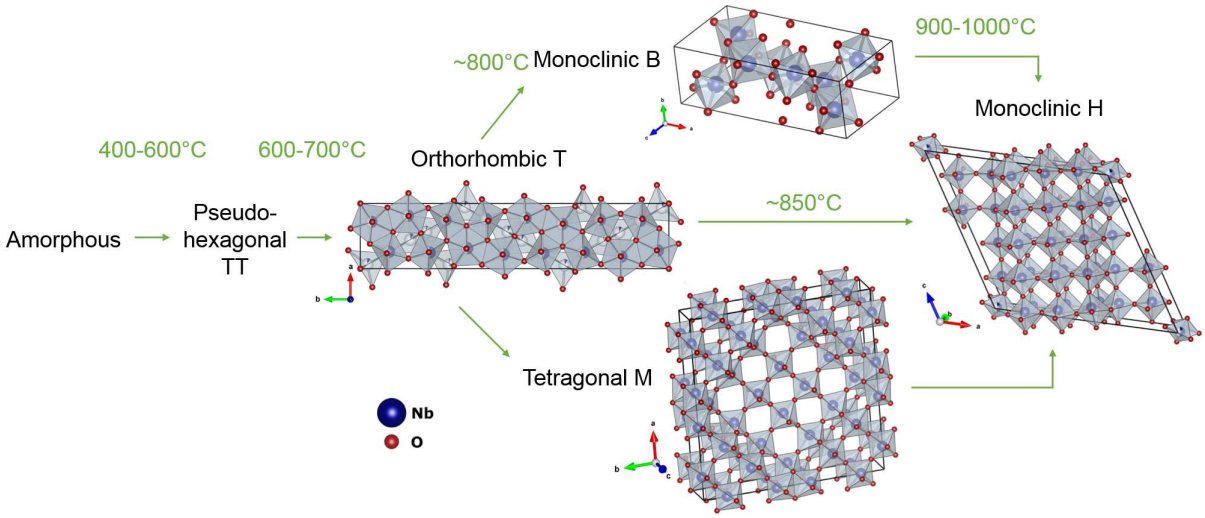

Figure 15: Temperature evolution of the most important crystalline phases of Nb_2O_5 according to [10] and [47].

The different structures and stoichiometries determine the physical properties of the generally low toxic and chemically stable niobium pentoxide, therefore it is used in various applications including dye-sensitized solar-cells, catalysis, humidity sensors, electrochemicals biosensors and lithium batteries [47].

2.3 Conduction in solids

The ideal niobia crystal without any defects, which could only theoretically be observed at 0 K, would be a perfect insulator. Ionic and electronic charge carries are present in every material at higher temperature due to defects. These defects range from missing atoms or impurities (0D or point defects) to more complex defects, such as dislocations (1D), grain boundaries or surfaces (2D) and volume defects (3D) [59].

Usually, the Kröger-Vink notation [40] is used for the nomenclature of point defects, where A = chemical symbol or V for vacancy, S = chemical symbol of the atom/ion which normally occupies this site or i for interstitial and C = relative charge:

$$A_S^C$$

The relative charge C is calculated by the charge on the current position minus the charge on the original position. Positive relative charges are indicated by dots $^\bullet$, negative charges by slashes $'$ and relatively neutral defects are indicated with ^{x}. To maintain overall neutrality of the crystal, the relative charge is compensated by other defects, which means that defects appear in pairs. In figure 16 an example for the point defects vacancy V_M and interstitial $M_i$in a monoatomic crystal of an element M are displayed [59].

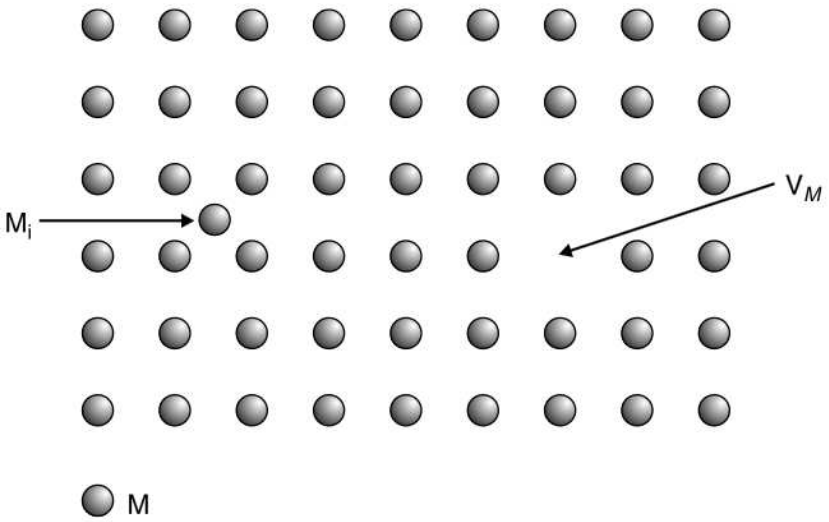

Figure 16: Point defects vacancy V_M and interstitial M_i in a monoatomic crystal of an element M [59].

Besides ionic defects, electrons e' and holes $h^\bullet$ as electronic defects are the charge carriers enabling electric conductivity in ceramic materials. The conductivity σ due to charge carriers of type i moving through a solid is given by equation (1) where σ_i = conductivity [S/cm], c_i = number of charged particles per unit volume [$^1/_{cm^3}$], q_i = charge of the charge carrier [C] and μ_i = mobility [$^{cm^2}/_{s*V}$].

$$\sigma = \sum \sigma_i \, with \, \sigma_i \; = \; c_i * q_i * \mu_i \tag{1}$$

The formation of charge carriers can be intrinsically (within the material) or extrinsically (by doping). The intrinsic defect formation is thermally activated, which means that higher temperature increases the amount of charge carriers and consequently the conductivity:

$$nil \leftrightarrow h^\bullet + e'$$

$$nil \leftrightarrow V_X^{\bullet\bullet} + V''_{cation} \, (Schottky \, disorder)$$

The formation of oxygen vacancies $V_O^{\bullet\bullet}$ is furthermore depending on the oxygen partial pressure p_{O_2}: oxygen vacancies are formed at low p_{O_2} and high oxygen partial pressure leads to the formation of electron holes. The general dependency of the defect concentration on the p_{O_2} is presented by the so-called Brouwer diagram in figure 17 [59].

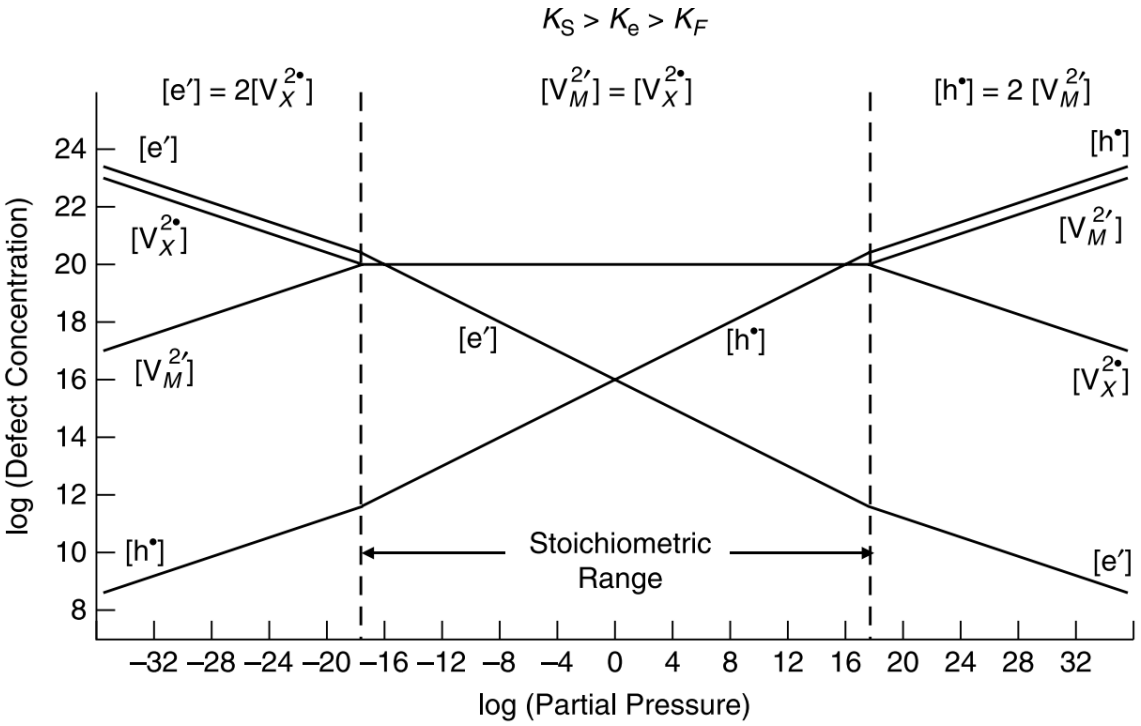

Figure 17: Brouwer diagram for a phase MX in which Schottky defects are the main point defect type [59].

2.3.1 Conduction mechanisms in Nb_2O_5

In 1961 Greener et al. explained the conductivity of sintered $\alpha - Nb_2O_5$ specimen by a defect controlled mechanism due to their experiments in the temperature range of 300 to 900 °C [33].

Chen and Swalin studied $\alpha - Nb_2O_5$ single crystals grown by plasma torch fusion and annealing in 1966, they identified singly ionized oxygen vacancies as predominant defects for electrical conductivity above 800 °C. For temperatures below 800 °C however they found an activation energy of 0.4 eV (compared to 1.4 eV) and explained it by a surface reaction controlled conduction mechanism: $^1/_2 O_{2_{(g)}} + e^- = O^-_{(s)}$ [19]

In 2017 Atta et al. studied 1-6 µm thick Nb_2O_5 films produced by RF sputtering on quartz and glass substrates and annealing. They linked the conductivity in the temperature region of 50-90°C to Mott's variable range hopping conduction process (with an E_A of 0.16 eV) and in the temperature region 100-210 °C to the phonon-assisted hopping model given by Mott (0.87 eV).

This literature survey demonstrates different conduction mechanisms in the same material depending on the sample production mechanism and studied temperature region.

2.4 Impedance

Impedance (Z) is the complex representation of potential difference divided y the complex representation of the current [2]. Therefore, the impedance of a material is dependent on the type of charge transport responsible for the current. For motion of free charge carries (Faradayic current), the resistance is calculated by dividing the geometric dimensions by the cunductivity, equation (2), where R = resistance [Ω], σ = conductivity [S/cm], l = length [cm] and A = area [cm²].

$$Z = R = \frac{1}{\sigma} * \frac{l}{A} \tag{2}$$

For charge being transported via displacement, e.g. due to dielectric polarization, the impedance is caused by the dielectric or capacitive properties of the material. The impedance can then be calculated using the permittivity ε, equation (3), where i = imaginary unit, ω = frequency [Hz], C = capacitance [F] and ε = permittivity [F/m].

$$Z = \frac{1}{i\omega C} \; with \; C = \varepsilon * \frac{A}{l} \tag{3}$$

2.4.1 Electrochemical impedance spectroscopy (EIS)

According to Barsoukov et. al. [13] the most common and standard EIS experiment is to measure impedance by applying a single-frequency voltage or current to the interface and measuring the response - the real and imaginary parts or the phase shift and amplitude of the resulting current. This procedure is repeated in a frequency range of roughly 1 MHz to 1 mHz in order to generate the typical Nyquist plot, where the impedance data is plotted in a complex plane with $Re(Z) \equiv Z'$ on the x-axis and $-Im(Z) \equiv Z$" on the y-axis or the so called Bode diagram, which plots $log(\mid Z \mid)$ versus $log(f)$.

The interpretation of such impedance spectra is normally carried out by modeling the sample with an equivalent circuit and fitting the data. Processes dissipating energy are represented by a resistance $Z_R = R$ in the equivalent circuit and energy storage is usually modeled by a capacitance $Z_C = \frac{1}{i\omega C}$ [44]. If these processes take place in the same material, they are modelled parallel as RC element. The impedance of the RC element is calculated according to equation (4), where R = resistance [Ω], $\omega = 2\pi f$ $[s^{-1}]$, f = frequency [Hz] and i = imaginary unit (representing the phase shift between current and voltage).

$$Z_{RC} = \frac{R}{1 + i\omega RC} \tag{4}$$

In the Nyquist plot, the impedance data of an RC element corresponds to a semicircle, for example see the equivalent circuit and corresponding plot in Figure 18, where the arrows show the direction of increasing frequency. The peak frequency $\omega_p = \frac{1}{RC} = \frac{\sigma}{\epsilon}$ is a material constant of the examined sample and can be utilized to differentiate between different materials. With impedance spectroscopy one can obtain the resistance values of each resistor separately, while using direct current only the DC resistance $R_1 + R_2$ of RC elements in series could be measured.

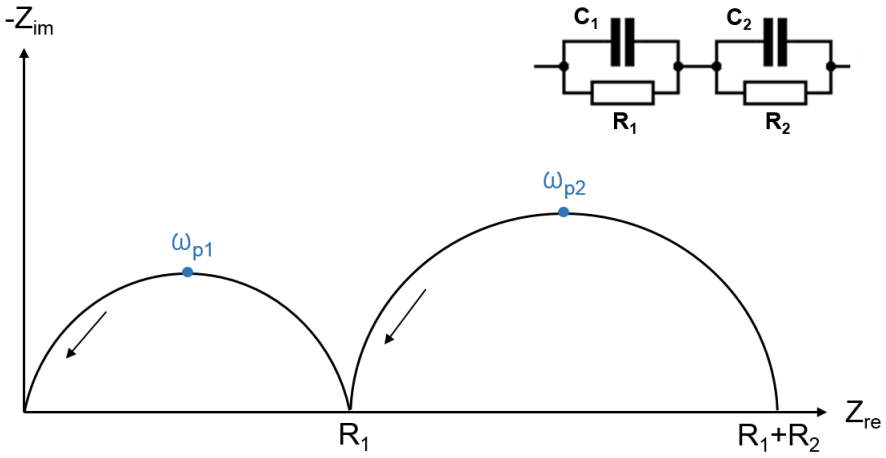

Figure 18: Nyquist plot for two resistor-capacitor circuits in series

By this means, the double layer capacitance of the electrode-sample interface can be separated from the sample as well as for example bulk conductivity from grain boundaries. Moreover, the technique of impedance spectroscopy can be used to determine parameters like charge carrier density and mobility, activation energy for diffusion mechanisms, charge transfer potential, polarization resistance, among others.

3 Materials & Methods

3.1 Chemicals and substrates

An overview of all materials used during the practical work for my diploma thesis are summarized in tables 1 to 3.

Table 1: List of chemicals

Name	Chemical formula	CAS Nr.	Purity	Supplier	Used for
2-Propanol	$(CH_3)_2 CHOH$	67-63-0	technical	Donau Chem	Cleaning agent
Acetone	C_3H_6O	67-64-1	technical	Donau Chem	Cleaning agent
Destilled water	H_2O	7732-18-5	technical	-	Cleaning agent
Ethanol denatured	C_2H_5OH	64-17-5	technical	Australco	Cleaning agent
Ethanol absolute	C_2H_5OH	64-17-5	99%	Chem-Lab NV	Solvent
Magnesium-chloride (anh.)	$MgCl_2$	7786-30-3	-	-	Cation source in precursor
Niobium(V)-chloride	$NbCl_5$	10026-12-7	99%	Sigma Aldrich	Precursor for Nb_2O_5
Pluronic® P123	$EO_{20}PO_{70} EO_{20}$	9003-11-6	-	Sigma Aldrich	Soft template
Potassium-acetate (extra pure)	CH_3COOK	127-08-2	99%	Merck	Adjustment of rel. humidity
Sodium-chloride	$NaCl$	7647-14-5	-	-	Adjustment of rel. humidity

Table 2: List of substrates

Substrate	Chemical formula	Characteristica	Supplier	Used for
Microscope alides	SiO_2 (72.2%), Na_2O (14.3%), CaO (6.4%), MgO (4.3%), Al_2O_3 (1.2%), K_2O (1.2%), SO_3 (0.3%), Fe_2O_3 (0.03%)		Thermo scientific Menzel-Gläser	substrate study, thin film optimization
FTO glasses	SnO_2/F	Pilkington NSG TEC™ 15	Sigma Aldrich	substrate study, thin film optimization, electrochemical samples
FTO backside	mainly SiO_2	Pilkington NSG TEC™ 15	Sigma Aldrich	substrate study, thin film optimization
Silicon Wafer	Si	one side polished	Sigma Aldrich	substrate study
Magnesium oxide single crystal	MgO	one side polished	CrysTec	substrate study, conductivity measurements
Sapphire single crystal	Al_2O_3	one side polished	CrysTec	substrate study, conductivity measurements

Table 3: List of machines

Machine	Details	Supplier
Scale	M-Power Professional	Sartorius Soehnle
Centrifuge	1-6P	Sigma
Spin coater for thin film production	-	Built by the university of Münster
Hot plate	RCT basic safety control	IKA
Muffle furnace	L3/11/S27 Program Controller S27	Nabertherm
Tube furnace	EWS JK 120926	University of Münster
Optical microscope	Imager.M1m	ZEISS
TGA	TGA 8000	PerkinElmer
SEM	Quanta 200F	FEI
TEM	TECNAI F20 at 200 kV	FEI
Profilometer	Dektak XT	Bruker
Contact angle	DSA100	KRÜSS
Sputter machine	MED 020 Coating System	BAL-TEC
Microscope of II-Pott "Prometheus"	FS70Z-S	Mitutoyo
Furnace of II-Pott "Prometheus"	Linkam TS 1000	Linkam Scientific Instruments Ltd
UV lamp of II-Pott "Prometheus"	LZ4-00U600, 11W 365nm	Led Engin
Vacuum pump of II-Pott "Prometheus"	rotary vane pump TRIVAC D 4 B;	Oerlikon Leybold Vakuumtechnik
Impedance analyzer	Alpha-A High Performance Frequency Analyzer and 2/4 Wire High ImpedanceTest Interface	Novocontrol Technologies

3.2 Manufacturing methods

In our study, we optimized the precursor solution composition and sample preparation method, as decribed in chapter 4.2, to suit our need of producing homogeneous mesoporous thin films. This led to the standard composition mentioned in table 4 and the standard method illustrated in figure 19. Each single method of the sample preparation will be described in the following section.

Table 4: Precursor solution composition for the sample preparation

Solvent	Polymer	Metal precursor	Cation
43 mmol EtOH	0.02 mmol P123	0.70 mmol $NbCl_5$	5 µmol NaCl

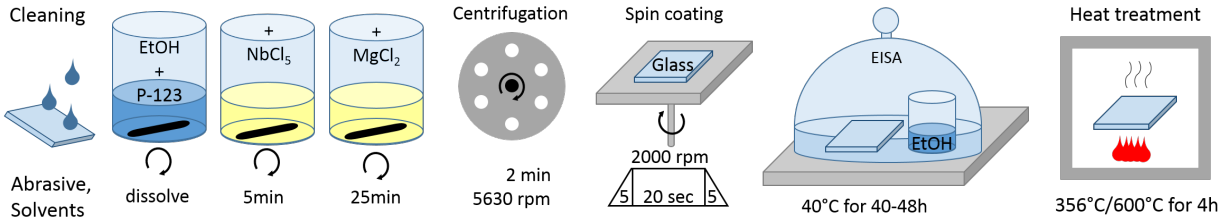

Figure 19: Sample preparation steps including precursor mixing, spin coating and EISA-process

3.2.1 Substrate preparation

The substrates which were not available in suitable sizes (silicon wafer and microscope slides) were cut to the dimensions of 5 x 5 mm and cleaned of glass residues using pressurized air. The standard cleaning procedure thereafter is listed in table 5.

Table 5: Standard cleaning procedure to prepare the substrates for spin coating

	Step	Solvent	Details
1	Rubbing	Abbrasive emulsion	DenkMit Scheuermilch
2	Rinsing	Tap water	
3	Rinsing	Distilled water	
4	Rinsing	Ethanol	
5	Ultra sonication	1 water : 1 ethanol : 1 acetone	30 min
6	Rinsing	Iso-propanol	
7	Ultra sonication	Iso-propanol	30 min
8	Drying	Pressurized nitrogen	

3.2.2 Centrifugation

Centrifugation is a technique where the sedimentation of particles in a solution, respectively fluids or particles of different density, viscosity, size or shape, is sped up by the replacement of gravitation by centrifugal acceleration. This is achieved by mounting the sample on a rotor which is spun at high rotation speeds. Consequently, denser material moves in radial direction and is accumulated at the bottom of centrifuge sample tubes [58].

Here, a laboratory centrifuge was used to clear the precursor solution from particles and suspended matter by spinning at 5630 rpm for two minutes. The transparent liquid was transferred in a new sample tube using a pipette to repeat the treatment, thus achieving a good separation.

Within my work I varied the amount of centrifugation steps from zero to two.

3.2.3 Spin coating, hot-spin coating and drop casting

In the **spin coating** process the coating material is applied to the center of a substrate, which is then accelerated to a determined rotation speed. Due to the centrifugal force, the liquid is forced radially to the edges of the substrate, where excess fluid is ejected. The film is thinning according to the angular speed and due to evaporation of volatile compounds in the coating solution. A mathematical description of the complex spin coating process can be found in a review by Bornside et. al [14]. In the present work the spin coating rotation speed was varied from 1,000 to 15,000 rmp which was held for 20 sec, the standard procedure was 2,000 rpm. The acceleration and deceleration took place within five seconds.

Hot-spin coating is differing from spin coating solely by applying the coating material to the already spinning substrate. Consequently, the coating time at 2,000 rpm was slightly shorter than 20 sec.

For the **drop casting** procedure, the coating solution is applied to the center of a substrate and dried through solvent evaporation.

3.2.4 Evaporation-induced self-assembly (EISA)

We used the amphiphilic triblock copolymer Pluronic® P123 $EO_{20}PO_{70}EO_{20}$ as soft template, ethanol as volatile solvent and niobium chloride $NbCl_5$ as inorganic precursor, which selectively entered the hydrophilic part (PEO) of the micelles, where the hydrolysis and condensation process is taking place. In order to retrieve good film qualities the evaporation process had to take place as slowly as possible, starting with 4 wt% P123. Therefore the substrates with spin coated sol were kept at 40 °C for 40-48 h according to Hashemzadeh et. al. [36] under a dome with an additional solvent. After the aging time, the dome was opened and the samples dried for four hours at 40 °C to obtain the gel.

In this thesis, we varied the following parameters: relative humidity (RH), air flow during EISA and pre-heated (oversaturated) EISA atmosphere. We also tested the addition of $NaCl$ and $MgCl_2$ salts.

3.2.5 Polymer removal and calcination

The mesoporous niobium oxide structure was obtained by burning the SDA in a heat treatment step, denoted as polymer removal. We varied the temperature for polymer removal between 250 °C and 420 °C and used Thermal gravimetric analysis (TGA) to determine the main oxidation- and side-processes such as solvent evaporation and crystallization, see chapter 4.2.1.

3.2.6 Sputtering

Sputtering or sputter coating is a process used to cover samples with a thin layer of conducting material [29]. Under high vacuum condition a gas plasma is produced between two electrodes using high voltage. The glow discharge leads to ion bombardment of the cathode, resulting in the erosion of the cathode material. The sputtered atoms are deposited on the surface of the whole vacuum chamber, thus covering the sample with a thin film of the cathode material [9].

In our study gold was used as a cathode material and the sample was covered with a mask to produce separated electrodes on the surface. The sputtering parameters, leading to roughly 100 nm thick electrodes (to guarantee high stability for mechanical contacting) are listed in table 6.

Table 6: Parameters used to sputter gold electrodes

Cathode material	Current	Pre sputtering	Sputtering time	Gas	Pressure
Gold	150 mA	30 s	125 s	Argon	$2 * 10^{-2} mbar$

3.3 Characterization methods

3.3.1 Microscopy

In optical microscopy a system of lenses is used to magnify the image of a sample, which is illuminated by visible light [37]. Modern microscopes are equipped with two light sources to switch between transmitted light mode, where the optical path is led through the sample, and reflected light mode. While the sample has to be transparent or very thin for the transmission mode, the reflection mode can be used to investigate all kinds of samples, but with the limit of only retrieving information about the surface. Due to diffraction, visible light microscopes operating with a wavelenth of 400 to 700 nm have a resolution limit of 200 nm [30]. For higher resolution the respective electron microscopy type has to be used, since electons can achieve wavelengths up to 0.001 nm.

In **scanning electron microscopy (SEM)** the focused electron beam is accelerated by a voltage between 1 keV and 30 keV and secondary electrons (SE), backscattered electrons (BSE), X-rays and auger electrons are recorded [30]. Each signal is produced by a different interaction of the primary electrons and therefore incorporates different information. BSE are scattered back from the sample surface according to the electron

density, consequently heavy atoms appear brighter than lighter ones in the generated image. SE are excited electrons from the sample escaping the surface and are used to produce an image with topological and morphological information. Characteristic X-Rays bearing information about the elemental composition are produced by inelastic collisions of the primary electrons with the electrons of the inner atomic shell of the sample. Auger electrons are generated by the relaxation of an excited atom and are deriving from the top most layer of the sample, thus providing surface information.

For **transmission electron microscopy (TEM)** the sample thickness has to be low enough for the electrons to pass through, usually around 100 nm [22]. The primary electrons are usually accelerated by 100 keV to 400 keV and are scattered by the sample accordint to the electron density, thus depending on the chemical composition and thickness, or penetrate the specimen unscattered.

3.3.2 Thermal gravimetric analysis (TGA)

TGA is a method to study the mass change of a sample as the temperature increases (dynamic measurement) as well as over time at constant temperature (isothermal measurement) [27]. The technique is used to determine phase transitions, thermal decomposition or physisorption/chemisorption processes. According to the gas environment used, oxidation or reduction reactions can be studied as well. The measurement setup exists of a precision balance encapsulated in a tube furnace, where the gas flow and temperature can be controlled. In order to perform a measurement the sample is simply put on a tared crucible, usually made of aluminium oxide, and hooked on the balance.

3.3.3 Contact angle

The contact angle measurement is a method to determine the wettability of a solid surface by a liquid by measuring the angle of the three-phase contact line of a droplet [28]. The contact angle is dependent on the chemical composition of the liquid and the topography and composition of the surface and can be related to the three interfacial free energies (solid-vapor, liquid-vapor and solid-liquid) by Young's equation. In order to measure the contact angle, a drop is placed on a sample surface and illuminated from one side. On the opposing side a camera records the image, which can be processed electronically by analysis software.

In our study, we used a KRÜSS DSA100 which featured a software-controlled dosing unit to set the drop size to 10 µl and the flow rate of the dosing system to 195 µl/min. For each substrate a minimum of eight images was taken and the tangential method T2 of the drop shape analysis software DSA v 1.90.0.14 was used to determine the respective contact angle. Figure 20 illustrates the used T2 method, where the three-phase contact point is fitted by a polynomial. Alternative methods would have been T1 where the drop is fitted by a conic section, CIR (circle fitting), HW (rectangle) and sessile drop (Young-Laplace), but these methods did not coincide that good with the liquid-vapor interface.

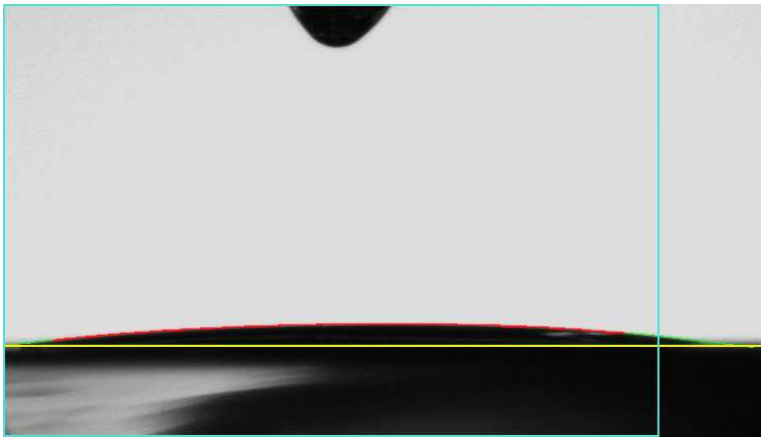

Figure 20: T2 method to fit the contact angle with DSA software

3.3.4 Profilometry

Profilometry is a method of measuring the topography of a sample, for example to determine the surface roughness. In a classic stylus profilometer the sample is placed on a stage for X-Y translation and moved under a diamond tip which is pressed with a certain force to the surface [18]. Variations of the sample height are detected very sensitively and processed by the analysis software to generate a 2 D depth profile in case a line scan was perfomed or a 3 D graph if the whole surface was mapped.

In our analysis, we scratched the sample and performed line scans perpendicular to the scratch using a stylus profilometer DektakXT. With the Vision64 operation and analysis software we controlled the parameters (1 mg force, 6.5 µm range) and evaluate the results by calculating the height difference. Figure 21 shows a typical result of a line scan, displayed by the analysis software. In the left part at 100 µm we can identify the scratch by the form of a crater and in the right part we see a crack at 420-470 µm with the characteristic vertical edges. The red part (R) in the middle (200-350 µm) is used to calculate the average thickness of the thin film as a reference to the depth of the crack, highlighted by the green layer (M). For each sample a minimum of nine measurements was performed in order to calculate the average and avoid statistical errors.

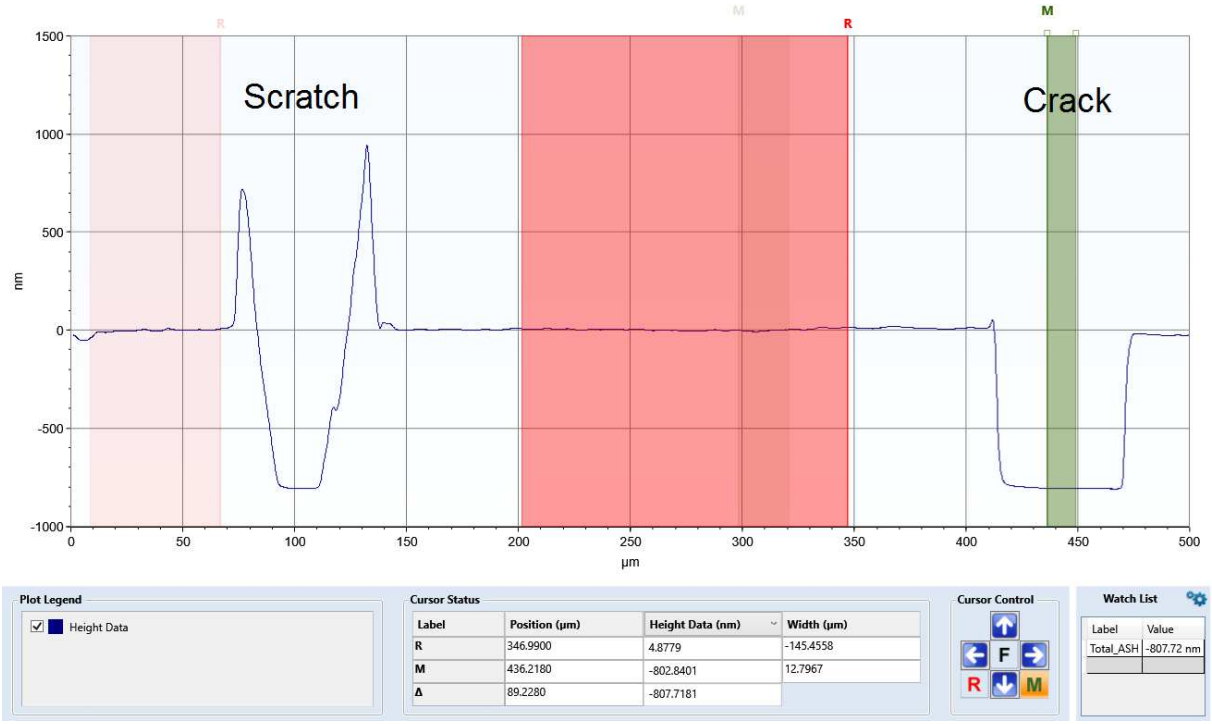

Figure 21: Example of a profilometry measurement showing a scratch and a crack

In terms of surface roughness the samples were very diverse. Due to the spin coating process ditches of different depth were spread over the whole sample surface. Sometimes they were visible under the microscope, like for sample RJ_K_FTO2. Profilometry revealed, that the surface roughness was about 10-15 nm, see figure 22. In relation to the calcines sample thickness of roughly 300 nm the surface roughness was below 5 % of the sample thickness.

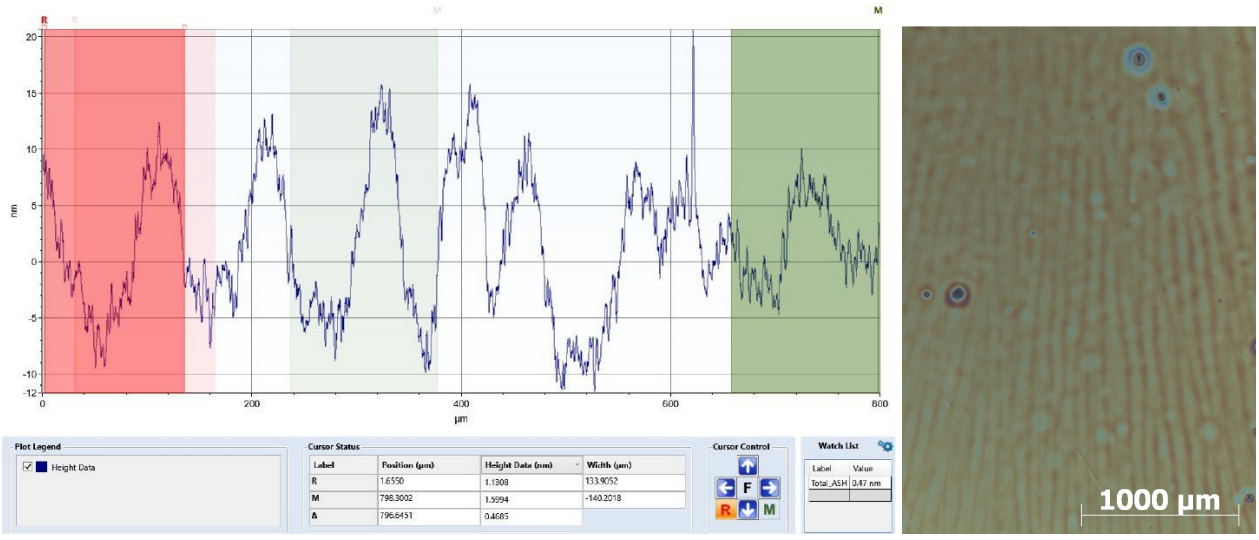

Figure 22: Profilometry measurement showing the surface roughness and image of sample RJ_K_FTO2

3.3.5 Electrochemical impedance spectroscopy (EIS)

In our analysis, we utilized two different sample architectures for cross-plane (figure 23) and in-plane (figure 24) measurements. The samples were investigated in the asymetrically heated measurement setup called II-POTT, presented in figure 25, which featured fast heating and changing of the contacted electrode [38]. The parameters used to program the impedance analyzer are presented in table 7.

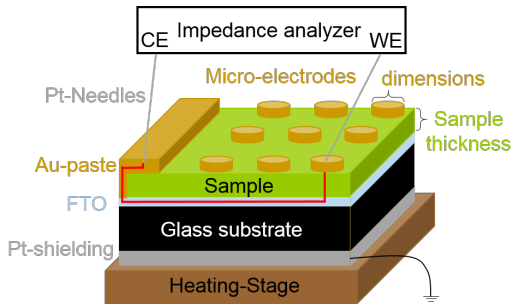

Figure 23: Sample architecture for cross-plane measurements (FTO substrate)

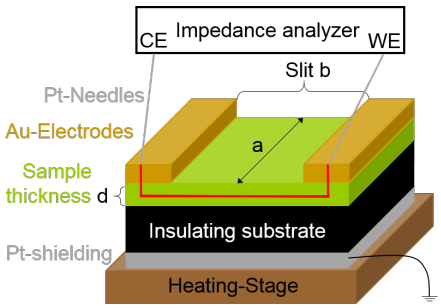

Figure 24: Sample architecture for in-plane measurements (sapphire substrate)

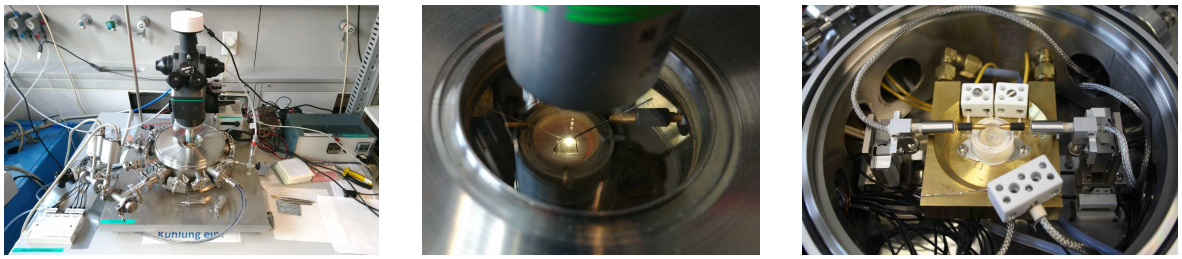

(a) Measurement setup II-POTT (b) During measurement (c) Open measurement chamber

Figure 25: Asymmetrically heated measurement set-up II-POTT [38]

Table 7: EIS measurement parameters

Parameter	Start frequency	Stop frequency	Output voltage	Bias voltage
Value	$1.5 \cdot 10^6$ Hz	1.0 Hz	0.01 V	0.0 V

We used the program ZView to perform an iterative fit for each single impedance spectrum and exported the result to excel-sheets. After determining the average resistance of the ten individual measurements, the effective conductivity σ_{eff}[1] was calculated according to equation (5) for in-plane measurements, where b = slit between the electrodes

[1] We did not have access to the actual surface and amount of material, so only the geometric dimensions could be used to calculate the effecive conductivity rather than the conductivity depending on pores, active surface (fissures) and amount of material used.

$[cm]$, A = cross sectional area $[cm^2]$ (thickness d of the mesoporous films · sample length a) and R = resistance $[\Omega]$, calculated by fitting the in-plane impedance measurements.

$$\sigma_{eff} = \frac{b}{R \cdot A} \; [S/cm] \tag{5}$$

To calculate the activation energy E_A for each studied sample, the slope of the regression line of the Arrhenius plot in figure 63 and equation (6) were used, where 2.3 = Conversion of log to ln, $k_B = 1.38 \cdot 10^{-23} \frac{J}{K}$ Boltzmann constant and $e = 1.602 \cdot 10^{-19} C$ elementary charge.

$$E_A = \frac{2.3 \cdot Slope \cdot 1000 \cdot k_B}{e} \; [eV] \tag{6}$$

4 Device manufacturing

Available substrates for the thin film production were conventional microscope slides [6], conductive substrates featuring a fluorine doped tin oxide (FTO) layer on one side, the backside of the conductive substrates (FTO backside), silicon wafers, magnesium oxide single crystals (MgO) and sapphire single crystals (Al_2O_3).

According to Nico et al. [47] the conductivity of amorphous Nb_2O_5 can vary between 10^{-10} and $10^{-13} S/cm$ at room temperature, therefore, the resistance of our mesoporous thin film of 1 µm on a 10 x 4 mm substrate was expected to be around 10^7 to $10^{10}\,\Omega$. To check the conductivity of our 10 x 10 mm substrates, silver electrodes were sputtered (see section 3.2.6) using a 4 mm spacer to create samples usable for impedance measurements described in section 3.3.5. All these samples are presented in figure 26 and the related resistance values measured are listed in table 8. When the resistance at room temperature (RT) was low, the measurement at 550 °C was redundant.

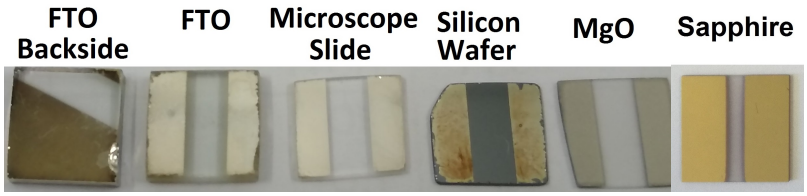

Figure 26: Samples for the impedance measurements to check the conductivity of all possible substrates for the production of mesoporous Nb_2O_5 films

Table 8: Resistance of the substrates, measured with EIS

Substrate	Resistance at RT [Ω]	Resistance at 550 °C set [Ω]
Microscope Slides	-	$5 * 10^4$
FTO	$20 - 30$	-
FTO backside	10^9	$4 * 10^4$
Silicon wafer	$4 * 10^7$	-
MgO	-	$>10^{11}$
Sapphire	-	$>10^{11}$

The substrate study revealed that only MgO and sapphire were sufficiently insulating substrates for the in-plane measurements described in chapter 3.3.5. All the other studied materials had too low resistances, which would complicate the distinction between substrate conductivity and the conductivity of the studied mesoporous layer.

In order to optimize the film quality in respect of homogeneity and fissures, we optimized the synthesis conditions using microscope slides, prior to manufacturing samples on MgO for the electrochemical characterization. Therefore, the sample batches RJ_A to RJ_G (batch overview listed in table 11) were produced on microscope slides.

- According to the substrate study FTO is suitable for cross-plane measurements while MgO and sapphire can be used as substrates for in-plane measurements.

4.1 General thin film synthesis

According to the literature study [63, 12, 36, 64, 41], the parameters for spin coating and EISA aging time were chosen to be 2,000 rpm and a minimum of 40 h at 40 °C. The precursor solution composition had to be varied and studied due to different procedures mentioned in literature. Thus, in batch RJ_A, different compositions were applied to substrates and the recipe leading to the best results was used for the further experiments.

In table 9 the main parameters for batch RJ_A are listed. The samples were subdivided into three groups of four samples with four different polymer (P123) to metal (Nb) ratios. The precursor solution for the first group (NB01-NB04) did not contain sodium cations (NaCl), the one for group 2 (NB05-NB08) contained sodium and a comparable amount of solvent (EtOH) and the precursor solution for the third group was diluted with EtOH.

Table 9: Precursor solutions for batch RJ_A to determine the best composition

	Sample name	EtOH [ml]	P123 / EtOH [mg/ml]	$NbCl_5$/ EtOH [mg/ml]	Ratio P123:Nb	NaCl [µmol]
Group 1	RJ_A_NB01	1.2	83.33	221.67	0.376	0
	RJ_A_NB02	1.2	100.00	190.00	0.526	0
	RJ_A_NB03	1.2	116.67	158.33	0.737	0
	RJ_A_NB04	1.5	133.33	126.67	1.053	0
Group 2	RJ_A_NB05	1.3	76.92	204.62	0.376	5
	RJ_A_NB06	1.1	90.91	172.73	0.526	5
	RJ_A_NB07	1.3	107.69	146.15	0.737	5
	RJ_A_NB08	1.6	125.00	118.78	1.053	5
Group 3	RJ_A_NB09	1.8	55.56	147.78	0.376	5
	RJ_A_NB10	1.6	63.5	118.75	0.526	5
	RJ_A_NB11	1.8	77.78	105.56	0.737	5
	RJ_A_NB12	2.1	95.24	90.48	1.053	5

The samples were prepared as described in section 3.2 and examined with the optical microscope three times: after EISA, polymer removal and calcination. The parameters for polymer removal and calcination in the muffle furnace are listed in table 10.

Table 10: Batch A parameters for polymer removal and calcination in the muffle furnace

Procedure	heating rate	T_{set}	T_{real}	holding time	cooling condition
Polymer removal	1 °C/min	350 °C	280 °C	4 h	default
Calcination	1 °C/min	500 °C	443 °C	1 h	default

The obtained films showed very distinctive homogeneity, for some were partially covered, others had large fractures and some films were pretty uniform. Some examples are presented in figure 27. The best results with only little fissures were obtained with the procedures highlighted in table 9, on sample NB03, NB06, NB07, NB08 and NB11. Since three of the best samples were found applying the procedure from group 2 and the best sample of the other groups had the polymer to metal ration of 0,737 the procedure of sample NB07 was chosen to be used for the following experiments to further improve the film quality in respect of uniformity and fissures.

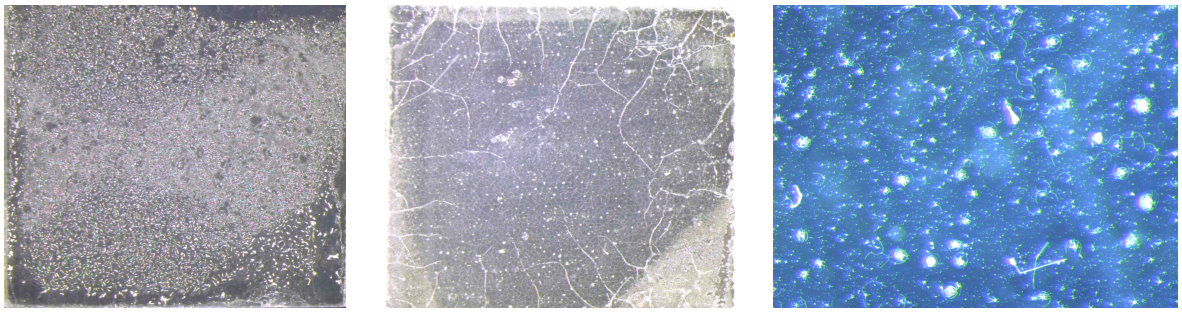

(a) NB01 after polymer removal, magn. x 8 (b) NB10 after polymer removal, magn. x 8 (c) NB11 after calcination, magn. x 50

Figure 27: Samples of batch RJ_A

- The Precursor solution variation led to the conclusion that a P123:Nb ratio of 0,737 leads to good substrate coverage and little fissures.

4.2 Optimization of synthesis conditions

Based on the results of batch RJ_A the precursor solution and other parameters were tuned to produce fully covered samples with little homogeneous fissures and controllable thickness. According to Lee et al [41] the addition of a small amount of cations dramatically improves the mesoporous structure, for example worm-like structures can be changed to highly ordered 3D hexagonal structures. Therefore, we replaced $NaCl$ by $MgCl_2$ and attempted to fix the concentration of Mg^{2+} to 0.05 M. In table 11 the parameters for the batches RJ_B1 to RJ_G are summarized. The precursor solution composition was only altered by doubling the amount of solvent from batch RJ_D onward, thus cutting the concentrations of polymer and metal in half. The other parameter changes are listed in the first column of table 11 and are discussed within this chapter.

Table 11: Purpose and precursor solutions for batches RJ_B1 to RJ_G

Purpose	Batch	Sample names	EtOH [ml]	P123/ EtOH [mg/ml]	$NbCl_5$/ EtOH [mg/ml]	Ratio P123:Nb	$MgCl_2$ [µmol]
Desired parameters				107.69	146.15	0.737	
SC vs. drop casting	RJ_B1	S1-S6 D1-D6	1.3	121.54	144.62	0.840	5
SC vs. hot-SC & muffle vs. tube furnace	RJ_B2	S10-S16 HS10-HS13	1.3	110.00	152.31	0.722	5
remove particles => centrifuge	RJ_C	S20-S26	0.7	111.23	155.38	0.716	2.5
varying EISA-environment	RJ_D	S31-S39	2.5	58.00	78.80	0.736	5
varying spin coating speed	RJ_E	S41-S49	2.5	58.00	78.80	0.736	5
varying spin coating speed	RJ_F	S50-S59	2.5	58.00	78.80	0.736	5
Humidity above RH70%	RJ_G	S61-S65	2.5	58.00	78.80	0.736	5

4.2.1 Thermal treatment

In our study, we used TGA to determine the decomposition temperature of P123. In a first scan, a dynamic measurement was performed at a constant heating rate of 10 °C/min under air, see figure 28. In order to get more detailed results the heating rates were adjusted and combined with an isothermal measurement, which led to the graph presented in figure 29 (the detailed procedure is described within the graph). Hereby, we could observe, that the majority of the decomposition takes place between 200 °C and 264 °C, respectively 300 °C. The rest of organic residues is removed around 460 °C, where the crystallization of Nb_2O_5 already starts [54].

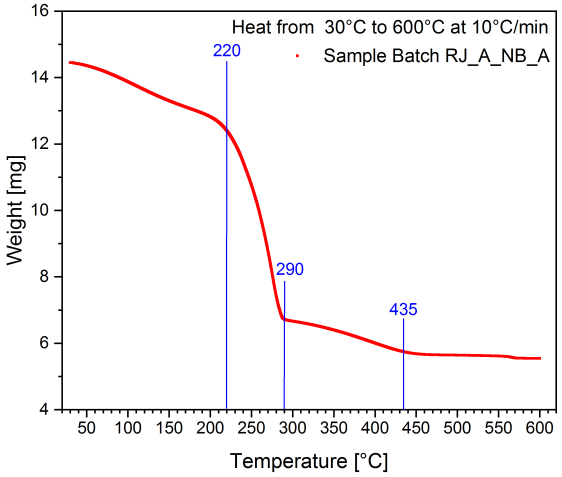

Figure 28: Dynamic TGA measurement of first sample batch

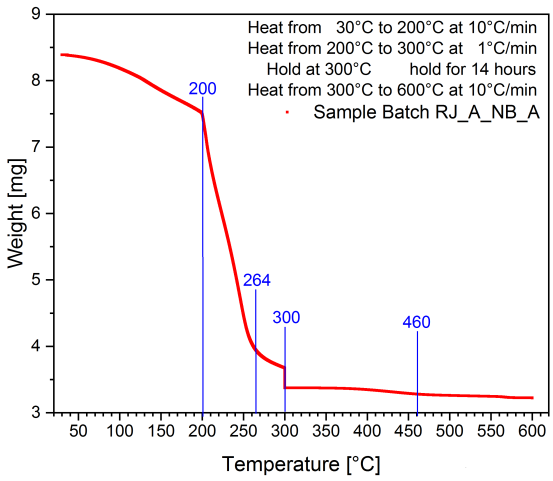

Figure 29: More detailed TGA measurement of Batch RJ_A_NB_A

After the TGA study the heat treatment denoted as polymer removal (section 3.2.5) was performed at 356 °C to guarantee amorphic structure and almost complete polymeric decomposition. In order to keep the stress low to avoid cracks in the thin film, the heating rate of 1 °C/min was chosen. The optimized parameters for the polymer decomposition and calcination in the muffle furnace, which led to the best samples, are listed in table 12.

Table 12: Optimized furnace parameters for polymer removal and calcination in the muffle furnace

Procedure	Heating rate	T_{set}	T_{real}	Holding time	Cooling condition
Polymer removal	1 °C/min	420 °C	356 °C	4 h	default
Calcination	1 °C/min	645 °C	600 °C	4 h	default

- After this study the standard thermal treatment for polymer removal was performed in a muffel furnace at 356 °C with a heating rate of 1 °C/min and a holding time of 4 h.

4.2.2 Effect of coating procedure

In sample batch RJ_B1 six samples were produced by spin coating and six by drop casting as described in section 3.2.3. The drop casted films had fractures already after the EISA and drying process, see figure 30. The thickness was varying between 33 µm and 42 µm.

The spin coated films had thicknesses of roughly 1,0 µm, appeared crack free after EISA and drying and were therefore calcined. After calcination small fissures were distributed all over the samples and were always located around black particles, see figure 31.

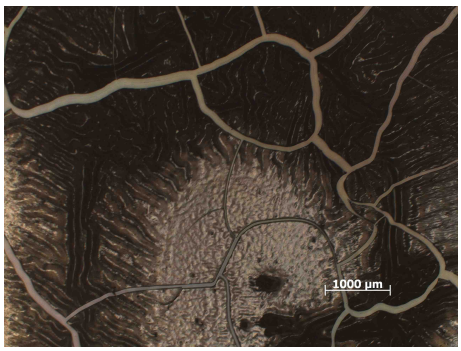

Figure 30: Drop casted sample RJ_B1_D2 after EISA, x 25

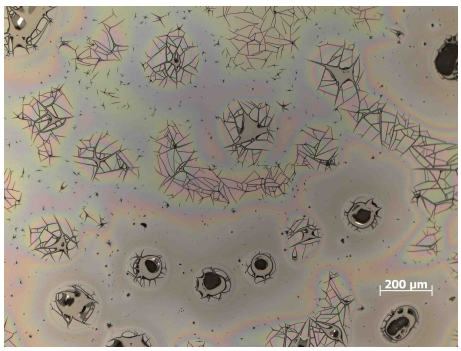

Figure 31: Spin coated sample RJ_B1_S6 (2,000 rpm) after calcination, x 100

Drop casting led to unsuitable films, too thick and showing large fractures. In batch RJ_B2 seven samples were produced by spin coating and four by hot-spin coating as described in section 3.2.3. By observing the samples with the microscope, all layers appeared crack free after EISA and drying step and were in the thickness range of 0.5 µm to 1.8 µm.

Respecting the spin coating procedure, the hot-spin coated samples featured non-uniform thickness, e.g. thinner films in the middle or only partially covered edges. Hence, applying the solution prior to starting the spin coating table was chosen as standard procedure for the further sample production.

- Drop casting appears to be an unsuitable coating procedure to obtain films with uniform thickness and little fissures.
- Spin coating led to better films compared to hot-spin coated films and was therefore chosen as standard procedure.

4.2.3 Heating conditions, type of furnace and atmosphere

In Order to test the effect of furnace conditions, the samples of batch RJ_B2 were distributed to three different polymer removal conditions. To the muffle furnace a beaker with 50 ml of EtOH was added, four samples were put into the tube furnace (dry) without air flow and the valves remained open. The last four samples were put into the tube furnace (wet), ventilated with pressurized air piped through a gas washing bottle filled with EtOH. The furnace parameters are listed in table 13.

Table 13: Furnace parameters for polymer removal and calcination for the different batches

Batch	Procedure	heating rate	T_{set}	T_{real}	holding time	cooling condition
RJ_B1	Polymer removal	0.4 °C/min	250 °C	172 °C	4 h	default
	Calcination	1 °C/min	500 °C	443 °C	1 h	default
RJ_B2	Polymer removal muffle furnace + EtOH	0.9 °C/min	350 °C	280 °C	6 h	default
	Polym. removal tube furnace dry & wet	1 °C/min	350 °C	317 °C	6 h	default
	Calcination muffle furnace	1 °C/min	550 °C	498 °C	1 h	default
RJ_C	Polymer removal	0.7 °C/min	420 °C	356 °C	4 h	default
	Calcination	1.2 °C/min	600 °C	551 °C	1 h	default
RJ_D, E, F, G	Polymer removal	0.7 °C/min	420 °C	356 °C	4 h	default
	Calcination	10 °C/min	645 °C	600 °C	4 h	default
RJ_H, J, K, L	Polymer removal & Calcination	1.2 °C/min	645 °C	600 °C	4 h	default

In figure 32, three typical images of the spin coated samples are displayed, one for each furnace condition. As the fissure distribution and size appeared similar for the tested furnace conditions, the most convenient one, the muffle furnace without extra solvent, was chosen as standard procedure for the further sample production.

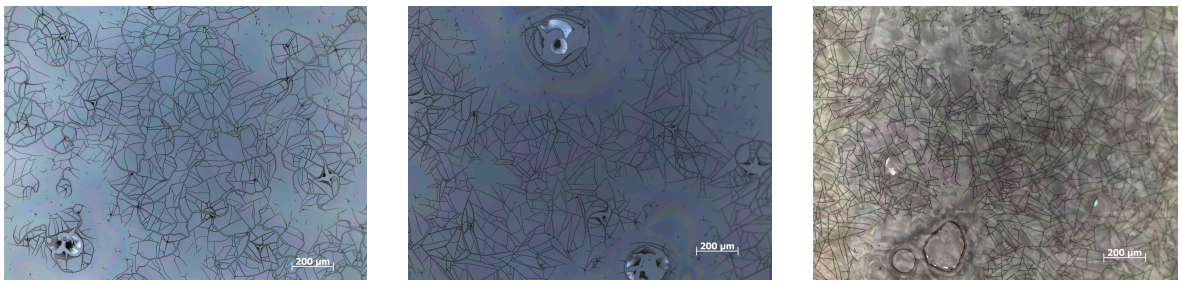

(a) S13 muffle furnace (b) S14 tube furnace wet (c) S15 tube furnace dry

Figure 32: Samples of batch RJ_B2, magn. x 100. The results of the different furnace conditions were similar, so the most convenient one (muffle furnace) was chosen.

To decrease the amount of particles present in all samples studied so far and possibly acting as crack nucleation point, the centrifugation step described in chapter 3.2 was added to the procedure for all following batches. In figure 33, two representative samples of Batch RJ_C are displayed. Due to the centrifugation step, there were significantly fewer particles and cracks found, the remaining fissures resulted to be longer.

The colored artifacts, visible in figure 33, are most probably deriving from residues of the precursor solution on the backside of the substrates and from surface roughness caused by solvent droplets compacting the film during the EISA process. To find the source of these droplets, variations of the EISA process were examined in the following batch RJ_D.

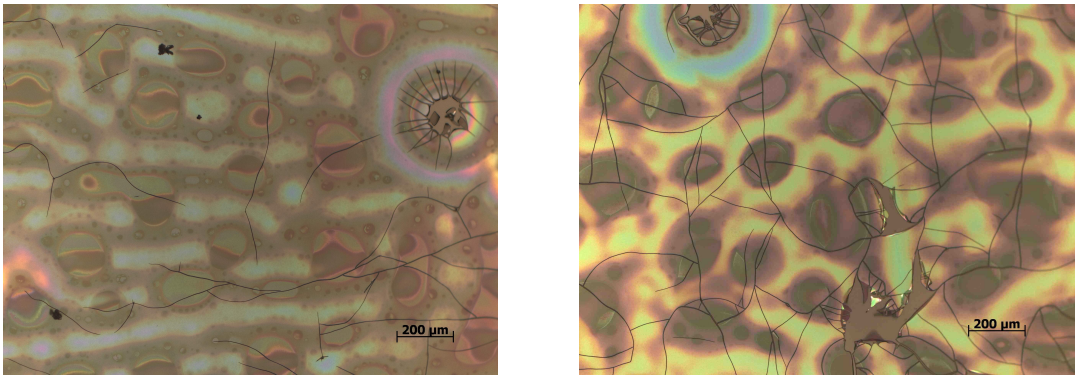

(a) S24 (b) S25

Figure 33: Samples of batch RJ_C after calcination, magn. x 100. Due to the centrifugation step the amount of particles and cracks could be decreased significantly.

- The variation of furnace conditions had no significant impact on the film quality.
- The film quality could be improved by adding a centrifugation step prior to spin coating and by diluting the precursor solution (using the double amount of EtOH).

4.2.4 Variation of EISA method

Batch RJ_D was intended to study the effect of different variations of the EISA process. Apart from the method described in section 3.2.4 (here called saturated atmosphere) the spin coated substrates were put under a glass dome with a pre-heated container of EtOH (oversaturated atmosphere) or put into the tube furnace with constant nitrogen flow, piped through a gas washing bottle filled with EtOH. All samples were kept at 40 °C for 41 hours and were then dried under air (opened dome, respectively tube furnace) for 1-2 h before they were observed with the optical microscope. In figure 34, samples of the three EISA variations are presented after drying and after calcination.

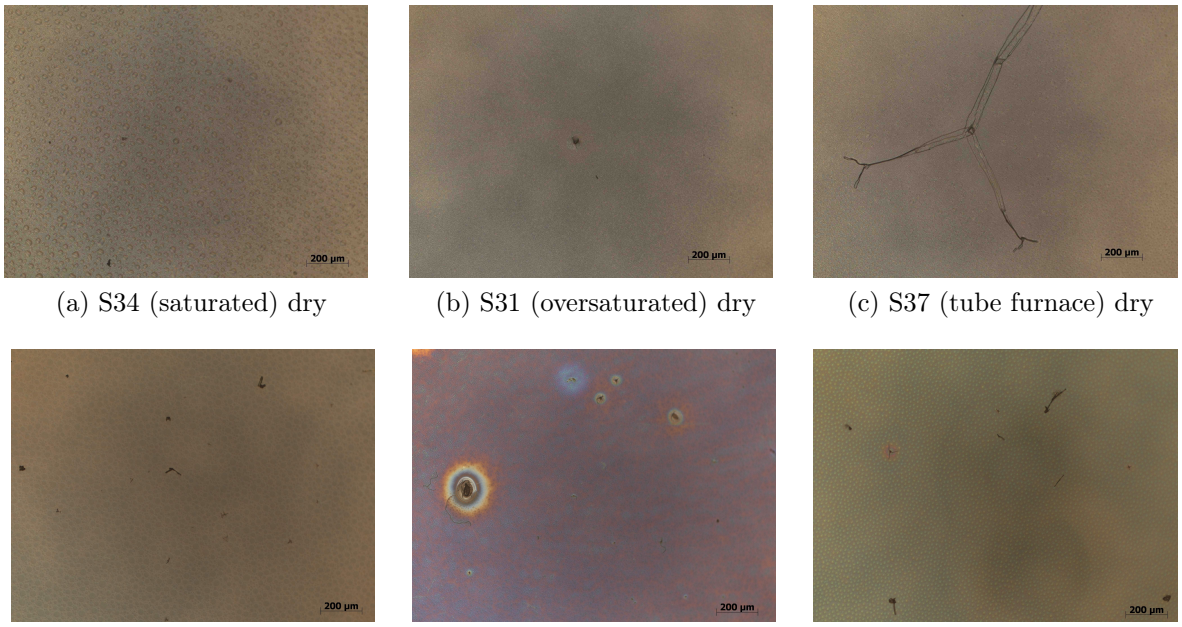

(a) S34 (saturated) dry (b) S31 (oversaturated) dry (c) S37 (tube furnace) dry

(d) S34 (saturated) calcined (e) S31 (oversaturated) calcined (f) S37 (tube furnace) calcined

Figure 34: Samples of batch RJ_D, magn. x 100. The different EISA methods studied did not lead to significant deviations in the film quality. By altering the precursor solution (double amount of EtOH) the fissures could almost be eliminated.

Similar to the samples of earlier batches, droplets of different size formed on the spin coated films, which caused the formation of dents during the EISA process. Such droplets were found on all samples after drying, which resulted in the color variations visible in the images of the calcined samples. Since the different EISA method variations did not show a correlation with the droplet formation, the standard EISA method (saturated atmosphere) remained unchanged for the following batches. Probable parameters affecting the droplet formation include fluctuations in relative humidity (discussed in chapter 4.2.6), room temperature and hotplate temperature. To minimize the mentioned effects and increase reproducibility, the working place was changed from the ordinary laboratory exhaust hood to a closed humidity box and the manual hotplate was replaced by one featuring digital temperature control.

Compared to the earlier batches, we observed a significant decrease of fissures in the samples of batch RJ_D, which could be linked to the change in the precursor solution described above (double amount of EtOH). While the few exisiting fissures were formed during the polymer removal at 350 °C around particles serving as crack nucleation point, the calcination heat treatment did not cause further crack propagation.

In batch RJ_D the film thickness was not only measured after the drying process but also after polymer removal and after calcination. Therefore, the shrinkage during the thermal treatments could be calculated. As presented in figure 35, the film thickness was varying between 740 nm and 950 nm after drying, however, after the average shrinkage of 55 ± 4 % during polymer removal, the thickness was varying only slightly around the average thickness of 365 ± 25 nm. The thermal treatment at 600 °C for the calcination caused another shrinkage of around 10 %.

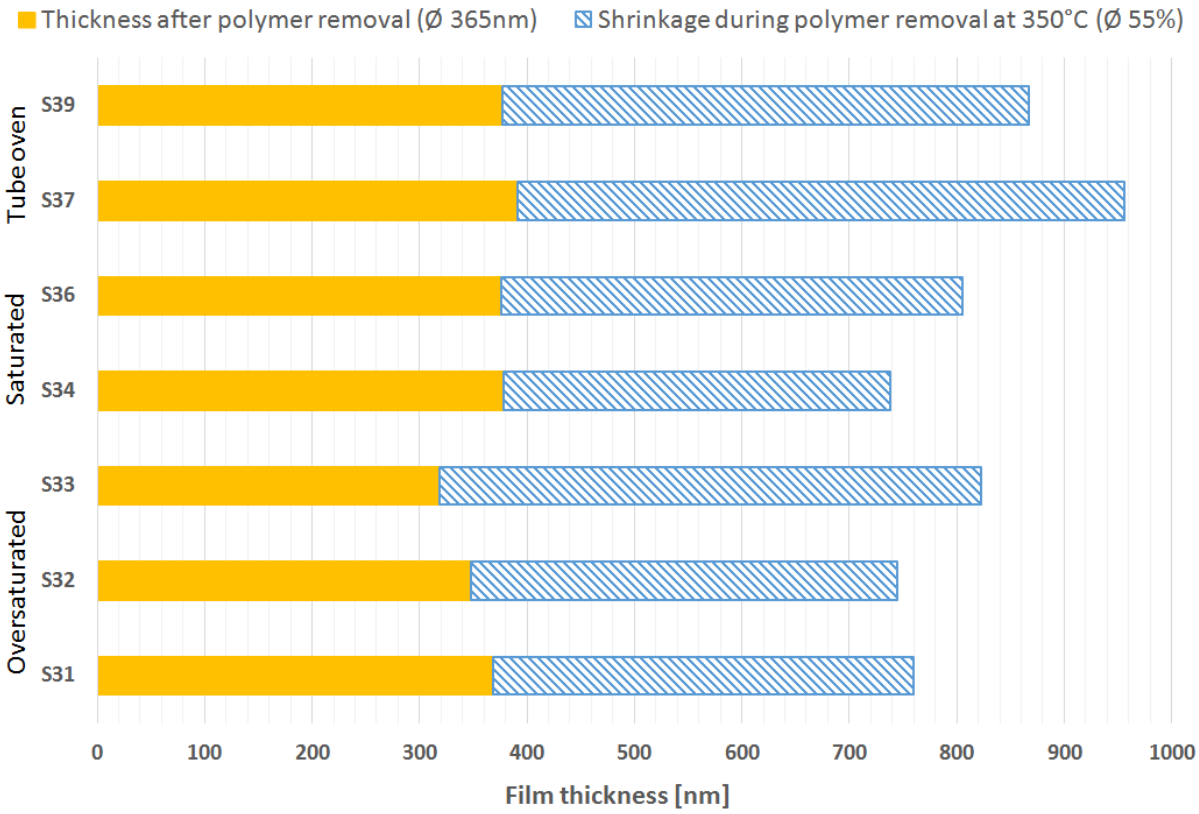

Figure 35: Film thickness and shrinkage during the heat treatment at 350 °C (batch RJ_D)

- The variation of the EISA method had no significant impact on film quality (droplet formation at the surface resulting in dents) or thickness.
- Fluctuations of relative humidity are influencing the evaporation induced self assembly process.
- The average shrinkage during polymer removal at 356 °C was found to be 55±4 %, during calcination at 600 °C another 13 ± 8 %.

4.2.5 Impact of spin coating speed

In the case of batch RJ_E and RJ_F the samples were prepared in the closed humidity box where the relative humidity (RH) was kept at a nominal value of 25 % using a saturated aqueous solution of potassium acetate [57]. We varied the spin coating speed from the minimum of the machine, 1,000 rpm, to the maximum, 15,000 rpm, while we kept the acceleration and deceleration times constant at 5 s.

In figure 36, a film coated at 1,000 rpm is displayed. On the heat-treated sample, color variations can be seen, indicating alterations in the film thickness. According to the bulge observed at the edges of the substrate, the centrifugal force at 1,000 rpm is not strong enough to sling away the excess precursor solution within 20 s, thus leading to an uneven film thickness and fractures at the outermost part of the substrate.

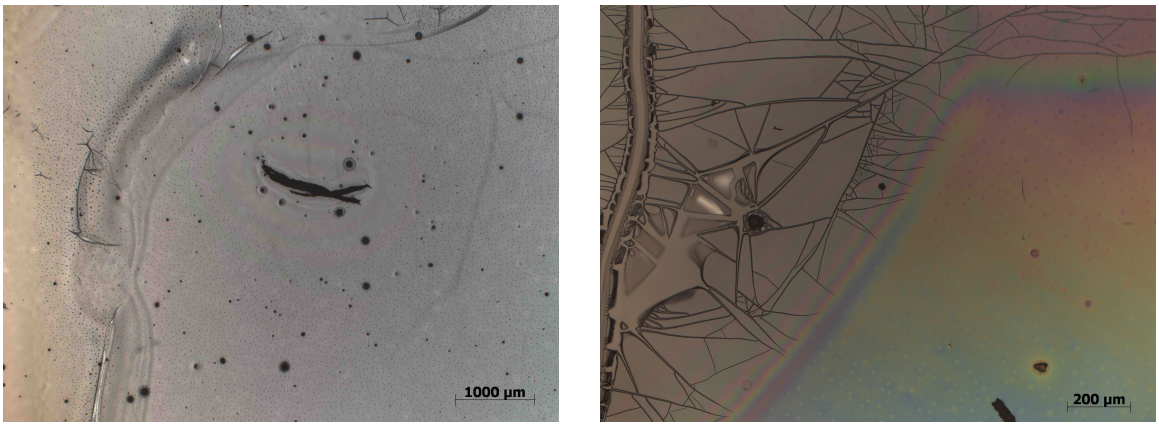

(a) after EISA, magn. x 25 (b) after 350 °C, magn. x 100

Figure 36: Sample RJ_E_S43, coated at 1,000 rpm, with non-uniform film thickness at the edges of the substrate.

At 8,000 rpm, figure 37, we observed the formation of air bubbles, which accumulated at the substrate edges. We did not observe the same phenomenon for other utilized speeds, hence we considered that speed as an aberrant date of our analysis.

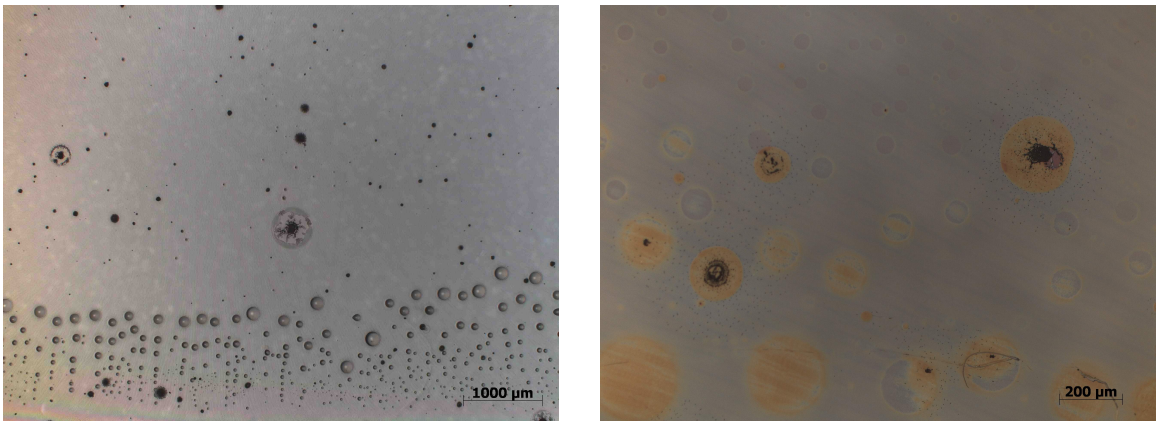

(a) after EISA, magn. x 25 (b) after 350 °C, magn. x 100

Figure 37: Sample RJ_E_S46, coated at 1,000 rpm, featuring air bubbles accumulated at the substrate edges and color changes around big particles after the heat treatment.

Another artifact observed in the samples of batch RJ_E after heat treatment were color changes around big particles, as presented in figure 38. After 350 °C the particles were still visible in the center of the colored area, after 600 °C only the outline of the former particle was visible in the image, figure 39. Also as seen in the SEM image in figure 40, the fragments of a former particle, consisting of an element with higher atomic number than the background, were visible, appearing like white crystallites. The source of these artifacts are probably already oxidized niobium particles present in the niobium chloride precursor, which were not successfully removed by centrifugation. These particles seem to have decomposed at elevated temperature and diffused into the film, thus vanishing from sight.

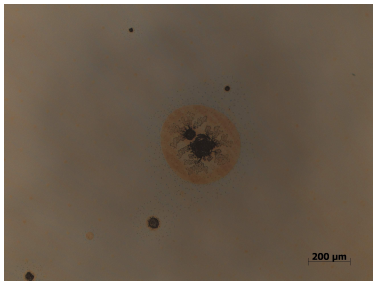

Figure 38: Sample S45 after polymer removal, magn.x 100

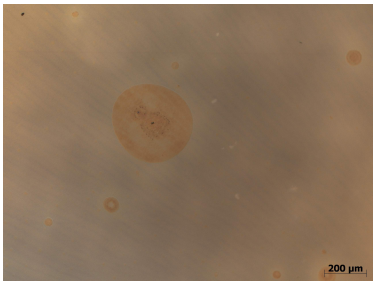

Figure 39: S45 after calcination, magn.x 100

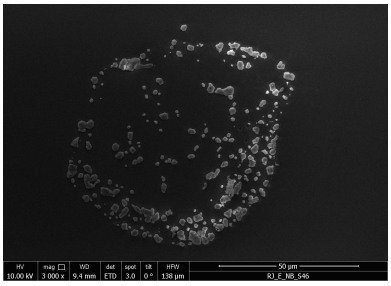

Figure 40: SEM image of S45, magn.x 3,000

In order to study the impact of spin coating speed on the film thickness, the average thicknesses were calculated for each speed and plotted into the graph presented in figure 41. As expected, faster rotation led to thinner films. Nevertheless, when the error bars are taken into account, the rotation at 1,000 rpm is not suitable for thickness control. The difference in film thickness between 2,000 rpm and 4,000 rpm is 25 %, but for all speeds above 4,000 rpm the difference is smaller than the error bars.

As a reference, the thicknesses obtained in batch RJ_D with spin coating at relative humidity of roughly 36 % are included in figure 41. The difference of humidity also lies in the range of the error bars, and the shrinkage percentages (55 % vs. 59 %) are very similar as well.

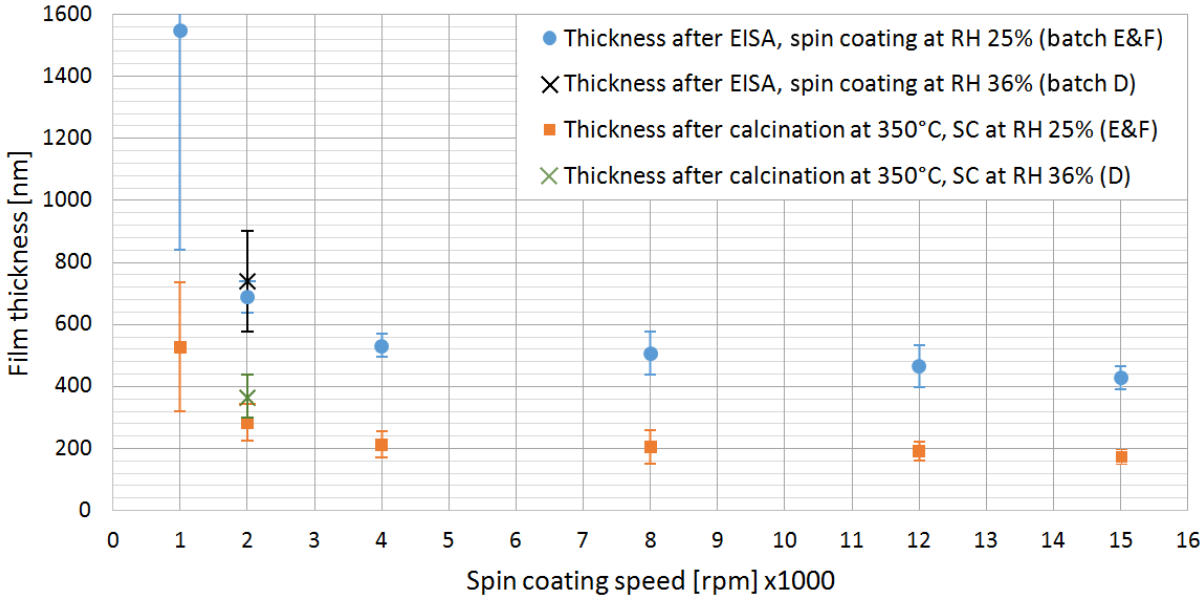

Figure 41: Film thickness depending on the spin coating speed (batch D, E & F)

- In the range of 2,000 rpm to 4,000 rpm the the film thickness is decreasing with increasing spin coating speed.
- 1,000 rpm was unsuitable for uniform films and speeds exceeding ,4000 rpm did not lead to significantly thinner films.

4.2.6 Effect of humidity

According to Lin Ye et al. [63] the relative humidity during the preparation is a critical factor affecting the structural selectivity of the mesoporous structure formed. It is reported that relative humidity above 50 % or below 30 % leads to the formation of worm-like or hexagonal mesoporous niobium oxides, see figure 42. Experimentally, in the samples produced at RH 25 % we confirmed what was reported in literature, see figure 43. However, due to calcination at 600 °C to improve the conductivity fo the film, the worm-like structure and porosity was lost due to grain growth up to 20 nm, visible in figure 44.

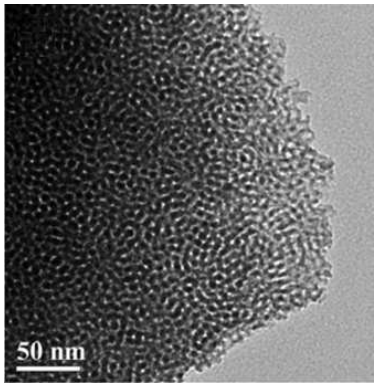

Figure 42: Wormlike Nb_2O_5 reported by Lin Ye et al [63]

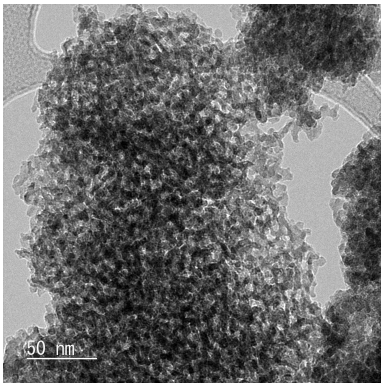

Figure 43: TEM image of RJ_F_S50 amorph, RH 25 %

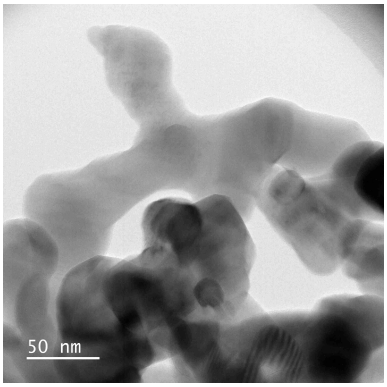

Figure 44: TEM image of RJ_F_S51 calcined, RH 25 %

In the SEM images presented below the impact of the calcination temperature on the obtained grain size is clearly visible. Sample RJ_F_S51 (RH 25 %) (figure 44&45) was calcined at 600 °C and has larger grains and pores compared to sample RJ_B_HS13 (RH 50 %), which was calcined at 500 °C (figure 46).

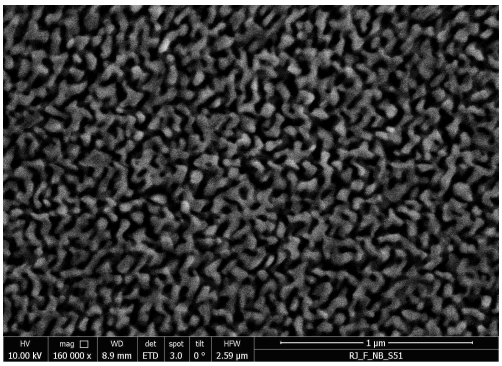

Figure 45: SEM image of RJ_F_S51 (RH 25 %), calcined at 600 °C

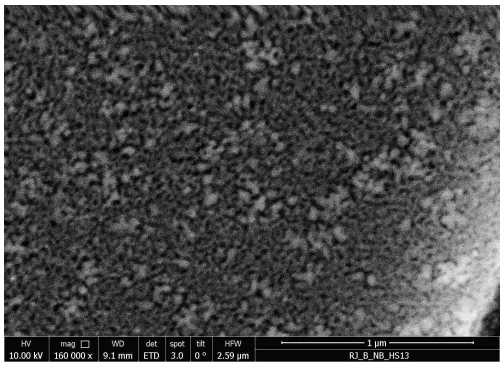

Figure 46: SEM image of RJ_B_HS13 (RH 50 %), calcined at 500 °C

To obtain an overview of the spin coating and aging parameters, the values for the according batch are listed in table 14.

Table 14: Parameter overview for batches RJ_B2 to RJ_G, where humidity, spincoating speed and EISA method were varied.

Batch	Sample names	RH	SC-speed [rpm]	Centri-fuga-tion	EISA at 40 °C	drying at 40 °C	Thickness dry [nm]	Thickness amorph [nm]
RJ_B2	S10-S16 HS10-HS13	50 %	2,000	-	45 h	1 h	1,260 ± 500	-
RJ_C	S20-S26	-	2,000	1 x	49 h	1 h	400 ± 80	-
RJ_D	S31-S49	36 %	2,000	1 x	41 h	1-2 h	740 ± 160	365 ± 25
RJ_E	S41-S49	25 %	1-15,000	1 x	41 h	2 h	400 - 1900	160 - 600
RJ_F	S50-S59	25 %	2-12,000	2 x	70 h	3,5 h	450 - 700	180 - 300
RJ_G	S61-S65	75 %	1-15,000	2 x	-	-	-	-

We equipped the humidity box with a saturated aqueous solution of sodium chloride to stable the RH level at a nominal value of 75 % [57] for the preparation of batch RJ_G, for the purpose of testing the behavior of the mesoporous niobium oxide films at high relative humidity. Optical microscopy after EISA and drying revealed uneven layers, featuring dark spots in the middle of the substrates, presented in figure 47. Therefore, the samples were not further characterized or heat treated. Obviously, the relative humitiy level was too high to form stable films and the maximum level is lying probably far below RH 75 %.

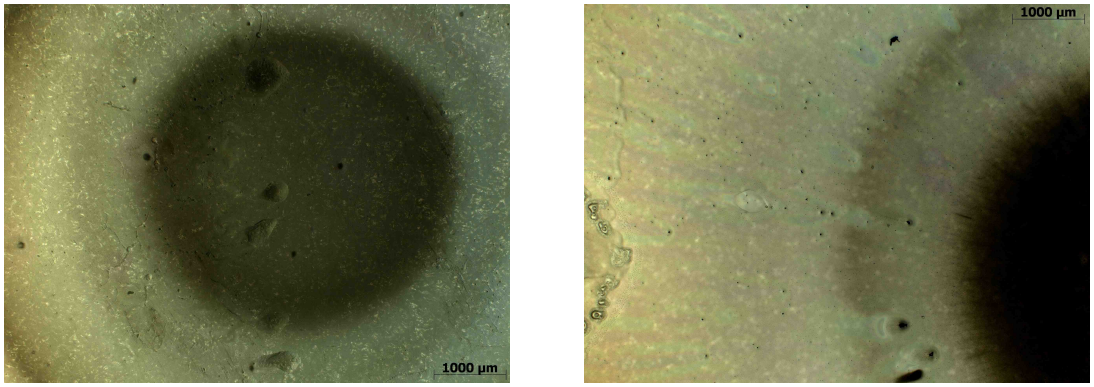

(a) S62 (b) S65

Figure 47: Samples of batch RJ_G, produced at RH 75 %, after EISA, magn. x 25, showing a dark spot in the centre due to uneven thin films

- We managed to produce uniform films at RH levels of 25 %, 36 % and 50 %.
- The humidity level of 75 % led to uneven thin films.
- Worm-like [63] structures could be observed for amorphous samples produced at a RH level of 25 %.
- The calcination process led to loss of porosity and grain growth in our samples.

4.3 Preparation of samples for electrochemical characterization

4.3.1 Transfer from glass to MgO-substrate

After optimizing the preparation, we identified the best procedure and listed them in table 15. These were applied to batch RJ_H1, using FTO slides and MgO single crystals as substrates.

Table 15: Parameter overview for batches RJ_H1 to RJ_L

Batch	RJ_H1	RJ_H2	RJ_J	RJ_K	RJ_L
Purpose	Change from FTO to MgO	Change from FTO to MgO	Apply to Al_2O_3	Samples on Al_2O_3 for EC	Samples on Al_2O_3 for EC
Sample names	FTO1-FTO4, MgO1, MgO2	FTO5-FTO8, MgO3, MgO4	FTO1-FTO3, Saph01, Saph02	FTO1-FTO6, Saph1, Saph2	L_Saph, L_MgO
EtOH [ml]	1.3	1.3	5	2.5	2.5
P123/EtOH [mg/ml]	56.56	56.08	56.00	56.80	56.00
$NbCl_5$/EtOH [mg/ml]	80.00	80.00	76.00	76.00	76.80
Ratio P123:Nb	0.707	0.701	0.737	0.747	0.729
$MgCl_2$[µmol]	2.5	2.5	10	5	5
RH [%]	~51	~51	36-46	43-55	43-55
SC-speed [rpm]	2,000				
Centrifugation	1x	1x	2x	2x	**1x**
EISA at 40 °C	41 h	-	73 h	-	68 h
Drying at 40 °C	4 h	1 h	**88 h 25 °C**	**20 min**	**4 h**
Polymer removal & calcination at 600 °C (heating rate 1.2 °C/min) for 4 h					

During the EISA process, we observed that the MgO samples did not reach a suitable dry state, yet the dome was opened and the samples dried at 40 °C for four hours as usual. The observation under optical microscopy confirmed that the procedure led to good samples on FTO slides, but the MgO substrates still had a droplet of EtOH covering a layer with fissures and particles in the case of sample RJ_H_MgO1 (figure 48). Sample RJ_H_MgO2 was subjected to a manufacturing mistake and therefore was not taken into account.

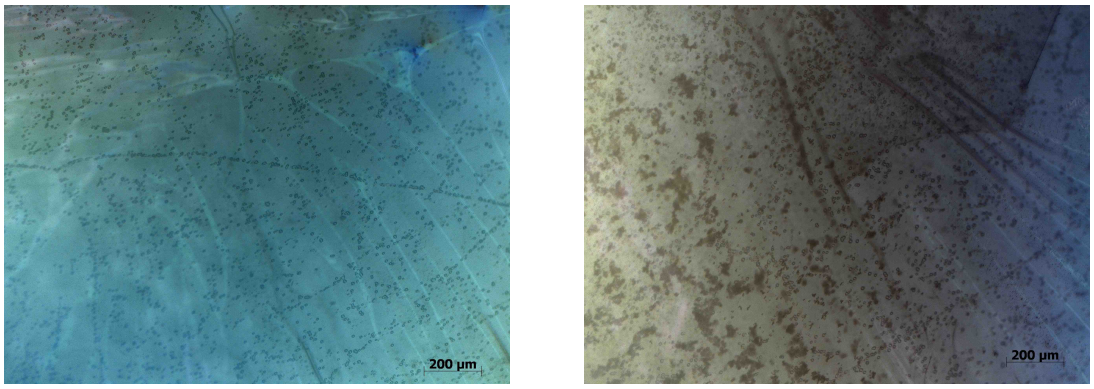

(a) (b)

Figure 48: Sample RJ_H1_MgO1 after EISA, two spots with magn. x 100 using a DIC-filter

The MgO substrates were thoroughly cleaned, as described in table 5, and re-used for the reiteration experiment batch RJ_H2, where the EISA process was skipped and all samples were dried for one hour at 40 °C. Microscopy revealed that the FTO samples showed more fissures due to the rapid drying process and also the MgO samples dried under the formation of fractures, see figure 49.

(a) RJ_H2_MgO3 calcined (b) RJ_H2_MgO4 after EISA

Figure 49: Samples on MgO substrate, magn. x 25, showing fractures.

- The EISA process did not work using MgO as substrate since the spin coated film did not dry but accumulate solvent at the surface which built a droplet covering the whole substrate.
- By skipping the EISA process the spin coated film could be forced to dry, but large fractures in the dimension of 100 µm were formed.

4.3.2 Contact angle study of FTO, MgO and Al_2O_3-substrates

To obtain insight of the surface qualities, contact angle measurements were performed on all substrates using pure ethanol as solvent, as described in section 3.3.3. Besides MgO, also two sapphire single crystals were used for the study, one was utilized as-manufactured, without pre-treatment, the other one was cleaned like described in section 3.2.1.

In figure 50, one representative image of each substrate is displayed to illustrate the appearance of the drop 15 seconds after the sessile drop was formed.

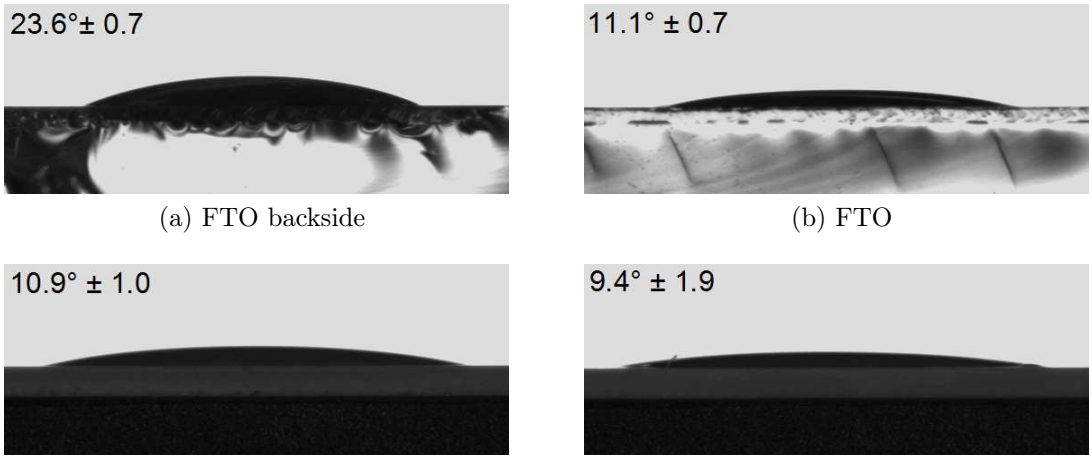

(a) FTO backside (b) FTO

(c) sapphire cleaned (d) sapphire as-manufactured

Figure 50: Contact angle measurements, images taken 15 seconds after drop formation

We see a change in the contact angle from 26.3° to 9.4° which is according to our conclusion due to a change in the wetting behavior.

In the case of MgO, three more images are included, see figure 51, since the EtOH drop wetted the whole surface within 90 seconds.

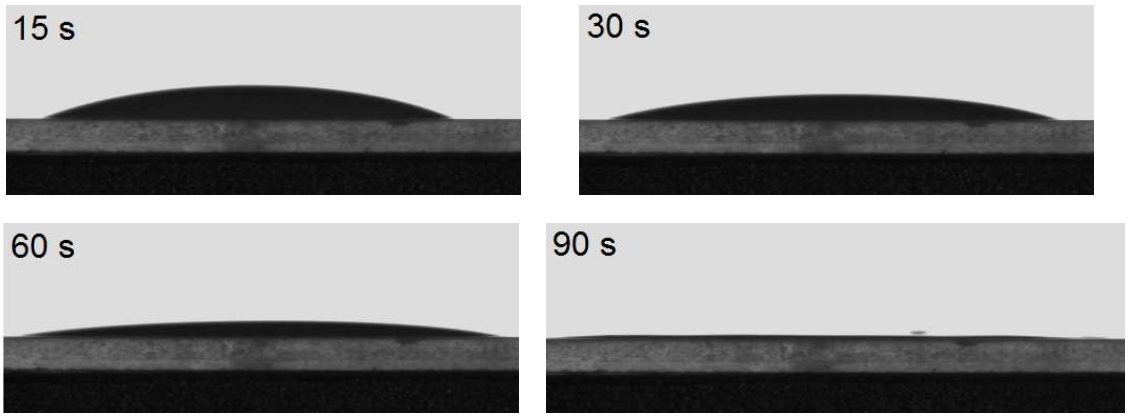

Figure 51: Contact angle measurements of MgO

The contact angle study confirmed the observation during the EISA process - MgO substrate is not suitable due to its **high hygroscopicity**. Therefore, we chose sapphire substrate for the production of samples for the electrochemical in-plane measurements.

- Due to its high hygroscopicity the contact angle of the MgO substrate could not be measured and MgO resulted to be unsuitable for the spin coating and EISA process.
- The hygroscopicity of the sapphire substrate could be reduced by cleaning. Therefore, a study of different cleaning procedures is proposed to further improve the surface conditions.

4.3.3 Transfer from glass to Al_2O_3-substrate

In batch RJ_J (for parameters see table 15), we spincoated three FTO glasses and two sapphire single crystals. After 41 h the sapphire substrates appeared to be wet, hence, the EISA process was prolonged to 73 h and the substrates were dried at room temperature for 88 h.

Optical analysis revealed that the FTO samples were not fully covered and the sapphire samples were covered with droplets and fractures, see figure 52. Therefore, the sapphire single crystals were cleaned and re-used in batch RJ_K while the FTO samples were calcined. Afterwards, the calcined FTO samples showed cracks.

We also tried to produce macro-samples, Nb_2O_5-pellets with a diameter of 5 mm, which we intended to use free-standing for measurements without substrates. Therefore, the excess precursor solution of batch RJ_J was filled into four teflon cups, the EISA process was carried out for 41 h, hence the macro-samples were dried for 88 h at 40 °C and afterwards in the vacuum furnace at 125 °C. After calcination, the macro-samples were not robust enough to be used. Since they were too thin, they broke even when they were handled very carefully with the tweezer.

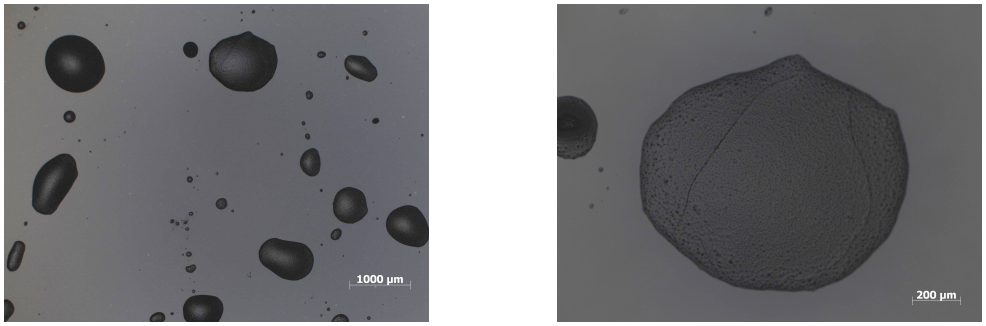

(a) droplets, magn. x 25 (b) fractured droplet, magn. x 100

Figure 52: Sample RJ_J_Saph01 calcined was covered with droples rather than by a film.

In batch RJ_K, the double amount of precursor solution (40 µl) was used for spin coating to overcome the problem of incomplete coverage. The EISA step was skipped completely, tolerating that the porosity order was lost, and the samples were dried for 20 min at 40 °C. The optical analysis after calcination revealed that all samples on FTO substrate as well as on saphhire looked alike and were covered with some particles, see figure 53. Hence, sample RJ_K_FTO1, having the least particles, was used as sample for electrochemical cross-plane measurements (described in section 4.3.4) and the two samples on sapphire substrate were used for the in-plane measurements described in section 4.3.5.

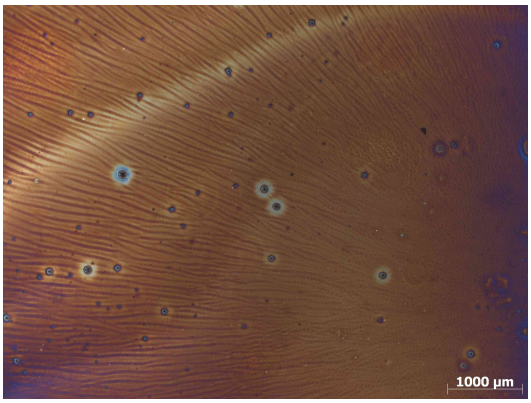

(a) Saph1

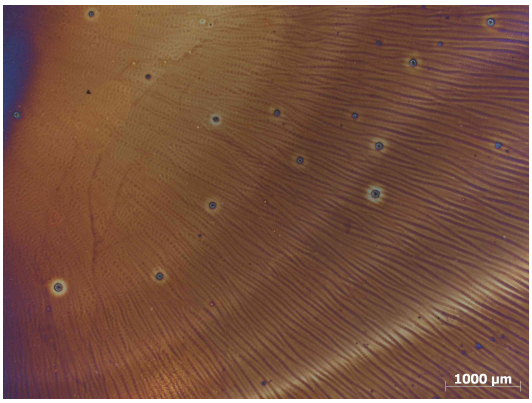

(b) Saph2

Figure 53: Samples of batch RJ_K after calcination, magn. x 25

In order to try to produce a sample for the electrochemical characterization with ordered porosity, in batch RJ_L the EISA process was conducted for 68 h at 40 °C and thereafter sample RJ_L_Saph was dried at 40 °C for four hours. Although the sample showed cracks, it was calcined, which resulted in enlargement of the fissures, see figure 54. Despite the openings, gold electrodes were sputtered and the sample was used for electrochemical in-plane measurements.

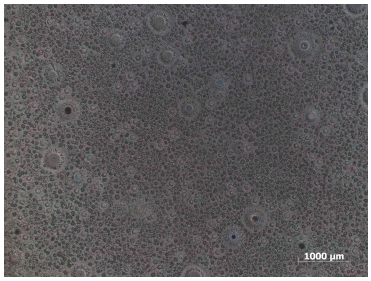

(a) after EISA, magn. x 25

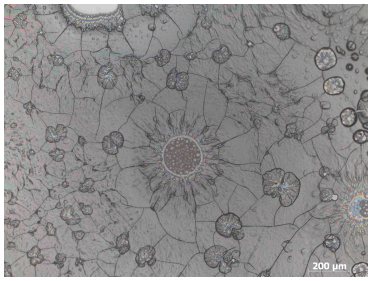

(b) after EISA, magn. x 100

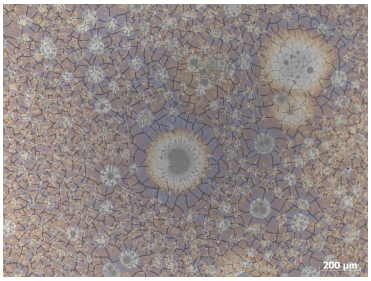

(c) after calcination, magn. x 100

Figure 54: Sample RJ_L_Saph showing cracks already after EISA which widened during calcination.

- The first trial on sapphire (batch J) led to droplets instead of a film, probably the cleaning procedure was not intense enough to prepare the surface properly
- Skipping the EISA process (batch K) led to samples with crack free films which could be used for the electrochemical characterization.
- The last trial (batch L) confirmed that thin films can be produced on sapphire substrate also with EISA, but the film quality was low - probably due to only one centrifugation step instead of two. The sample was used in the electrochemical characterization only for the temperature variation to create an Arrhenius plot.

4.3.4 Cross-plane measurements

In order to conduct cross-plane measurements, setup described in section 3.3.5, conductive substrates were required, so the samples with the best Nb_2O_5- films on FTO substrate were used. Since RJ_H1_FTO4 and RJ_K_FTO1 had almost no macroscopic fissures and only very few particles, they were selected for these measurements. So, circular gold electrodes with a diameter of 1 mm were sputtered according to the procedure described in section 3.2.6, using a 3D-printed mask. In figure 55, the samples are plotted before and after sputtering.

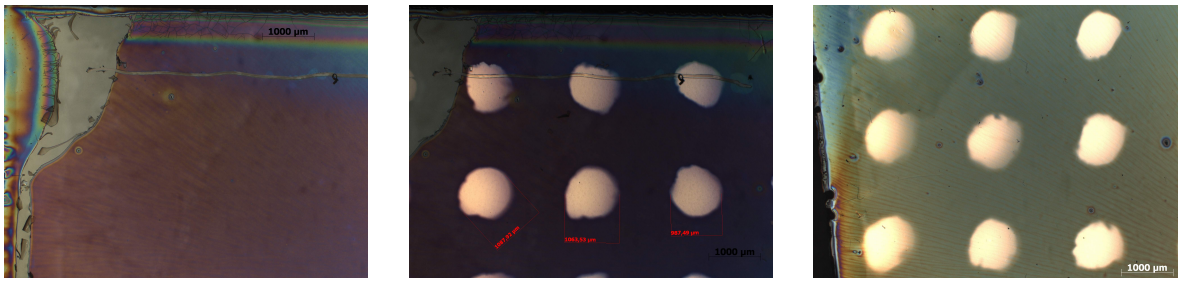

(a) RJ_H1_FTO4 after calcination (b) RJ_H1_FTO4 with electrodes (c) RJ_K_FTO1 with electrodes

Figure 55: Samples for cross-plane measurements, magnification x 25

Electrodes sputtered on top of an opening or a particle were directly connected to the FTO layer, which was used as a counter electrode, causing a short circuit. Hence, each single electrode was contacted at room temperature and the resistance was measured using the impedance analyzer. By this means, the electrodes which had short circuits were sorted out, which resulted to be 70 % in the case of sample RJ_H1_FTO4 and 45 % in the case of RJ_K_FTO1.

After screening, the samples were heated to 350 °C and contacted again, in order to measure the resistance of the Nb_2O_5- film. Although the Pt-needles were mounted on a spring and they were moved with the slowest speed of the setting motor, it was impossible to measure reproducible values. In case the optical microscope confirmed that the needle did not pierce through the niobium film, the resistance remained higher than $10^6\,\Omega$. When the resistance was lower, usually between 16 Ω and 1,000 Ω, on average 311 Ω (at 350 °C set), the microscope revealed that the film was pierced.

Due to this behavior, it was impossible to measure the resistance of the mesoporous Nb_2O_5- films using sputtered gold elctrodes.

In order to overcome the problem of electrode piercing, gold-paste was utilized to make electrodes on sample RJ_K_FTO3. Since the gold-paste showed higher stability, there was no problem of electrode piercing, and interestingly, not a single electrode had a short circuit. Probably the paste is too viscous to fill the small fissures.

At room temperature, the resistance of nine individual gold-paste electrodes, with slightly differing size, varied between $8 * 10^3\,\Omega$ and $8 * 10^7\,\Omega$, with an average of $10^5\,\Omega$. At measurement temperature (350 °C set) the paste tended to stick to the needles when they

were lifted off the surface, thus destroying the electrode. Hence, reproducible impedance measurements at elevated temperatures could not be performed.

In conclusion, neither the sputtered gold electrodes nor the gold-paste electrodes were suitable for cross-plane measurements. Therefore, the focus was laid on in-plane measurements, discussed in the following chapter 4.3.5.

- There were two challenges concerning sputtered micro-electrodes:
  1. 45-70 % of them were connected to the counter electrode and could therefore not be used.
  2. Although the thickness of the gold electrodes was roughly 235 nm the Pt-needles easily pierced the electrodes, thus destroying them.
- Gold-paste electrodes showed higher stability and no short circuits, but easily detached from the thin film.
- In order to conduct cross-plane measurements, the setup and electrode design has to be improved.

4.3.5 In-plane measurements

In the case of in-plane measurements (figure 57) the slit width b between the electrodes is the main parameter influencing the measured resistance. Simple 3D-printed masks were used to produce samples with only two electrodes and a slit inbetween. In this manner, the electrochemical samples presented in figure 56 were produced with the sample dimensions listed in table 16. It has to be noted, that sample S-0.5 was produced by sputtering a new gold layer on top of sample S-3.2 using a smaller mask. Therefore, the outlines of the 3.2 mm slit are visible at the same time as the 0.5 mm slit in figure 56. The scratches in the corners were produced to determine the film thickness using profilometry.

Table 16: Overview of all samples for the electrochemical characterization and new nomenclature

Substrate	Electrodes	Slit width b [mm]	New sample name	Film thickness d	Sample length a
RJ_K_Saph1	Au-sputtered	1.895 mm	S-1.9	0.386 µm	9.39 mm
RJ_K_Saph2	Au-sputtered	3.174 mm	S-3.2	0.557 µm	9.08 mm
RJ_K_Saph2	Au-sputtered	0.542 mm	S-0.5	0.557 µm	9.24 mm
RJ_L_Saph	Au-sputtered	1.769 mm	S-1.8	0.283 µm	8.55 mm

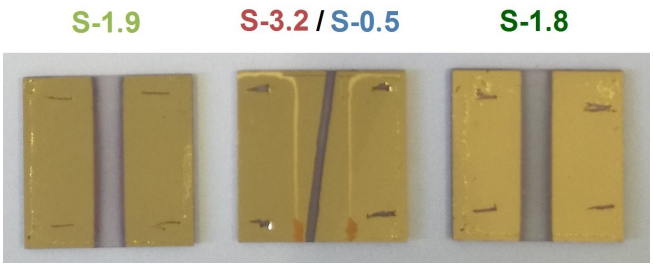

Figure 56: Samples for the in-plane measurements (S-0.5 was produced using S-3.2)

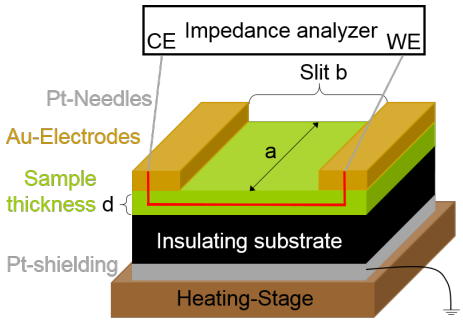

Figure 57: In-plane setup and sample dimensions

- The in-plane setup turned out to be very practical for our characterization, featuring large electrode areas, so the platinum needles could easily be contacted on a different spot if the the gold electrode got pierced while contacting.

5 Results & Discussion

5.1 Electrochemical characterization under temperature variation (350°C-600°C)

Impedance measurements for different temperatures were required to create an Arrhenius plot, a diagram plotting the logarithm of a variable against the inverse temperature. As a first test, sample S-1.9 was heated to 170 °C, but the impedance analyzer produced values greater than $10^{13}\,\Omega$ which is unsuitable for normal measurements. In figure 58 the spectra for 170 °C (black), room temperature (red and blue) and pure Al_2O_3 substrate (green) are displayed. After decontacting, the set-temperature of the furnace was changed to 500 °C. At this temperature, the impedance analyzer produced a semicircle, indicating that the measurement was successful, see figure 59.

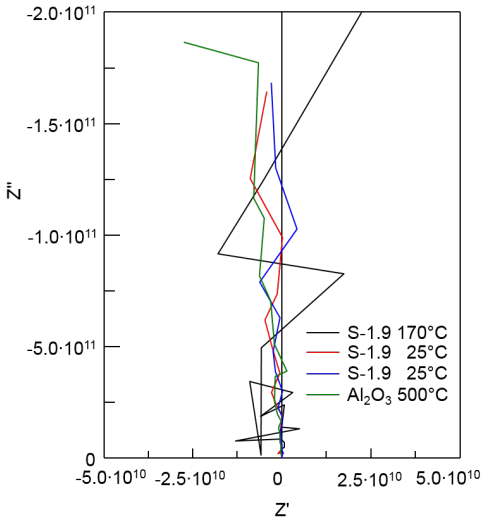

Figure 58: Baseline at room temperature and blind test of pure substrate

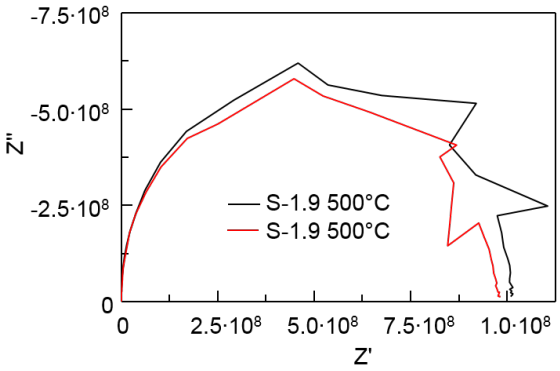

Figure 59: Impedance spectra showing only one semicircle, thus proving our concept of dominant solid-vapor interface and negligible contact to the electrode

According to our sample design using a mesoporous layer with high surface area, we expected to eliminate the contact resistance with the electrode while allowing a maximum interface with the surrounding gas phase. As figure 59 shows only one semicircle and no offset on the abscissa in the nyquist plot, the acquired data proved our concept.

We had to cope with a temperature invariance due to relative film thickness and therefore differing distance to the heating stage. However, the film thicknesses only accounts for roughly 1 ‰ of the substrate thickness (500 µm) and therefore we assume that temperature variations due to different film thickness can be neglected.

5.1.1 Peculiarities associated with reaching temperature equilibrium

For the Arrhenius plot, five to seven temperatures were measured, for details see table 17. For each temperature, a set of ten measurements was performed, and after the elimination of unreliable values (acquired before the temperature equilibrium was reached) the average resistance was calculated.

Table 17: Set temperatures T_{set} for the EIS measurements to calculate the Arrhenius diagram

Sample	$T_{set}1$	T_{set} 2	T_{set} 3	T_{set} 4	T_{set} 5	T_{set} 6	T_{set} 7	T_{set} 8	T_{set} 9
S-1.9			400 °C		450 °C		500 °C	550 °C	600 °C
S-3.2			400 °C		450 °C		500 °C	550 °C	600 °C
S-3.2_rep	350 °C			425 °C		475 °C		525 °C	575 °C
S-1.8		375 °C	400 °C	425 °C	450 °C	475 °C	500 °C		
S-0.5	350 °C	375 °C	400 °C	425 °C	450 °C	475 °C	500 °C		

In the asymetrically heated measurement setup [38] temperature equilibrium was usually reached within ten to twenty minutes. In order to verify if the temperature equilibrium was reached, the impedance spectra were recorded in 3.5 min intervals. Figure 60 presents the impedance spectra of sample S-1.9 measured at 400 °C. The red spectrum 002 is bending inward at the end (lower frequencies) which is very typical for a temperature increase while the measurement is performed. After 50 min, the spectra three to eight resulted in the same resistance value, which means, that temperature equilibrium was reached and the sample was stable at 400 °C set temperature.

The same sample measured at 600 °C (figure 61) showed a completely different behavior. Instead of bending inward, the spectra are bent outward a little bit, which would indicate a temperature decrease or a resistance increase at constant temperature. Even after 74 min there was no temperature equilibrium reached, but the semicircles were growing in size with time.

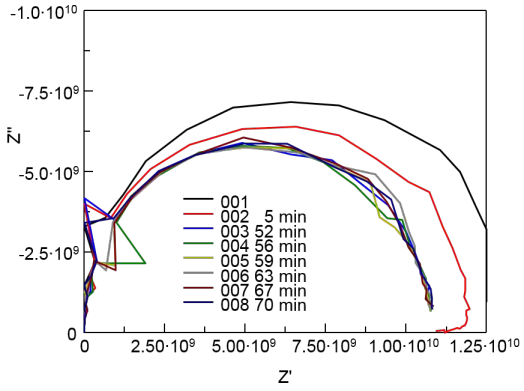

Figure 60: Impedance spectra of sample S-1.9 at 400 °C. After 50 min temperature equilibrium was reached.

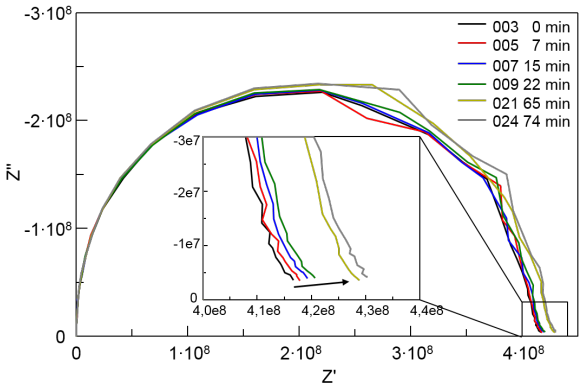

Figure 61: Impedance spectra of sample S-1.9 at 600 °C. There is no temperature equilibrium, the values are changing continuously.

In figure 62 the resistance of the impedance spectra presented above are plotted versus time of measurement to demonstrate the temperature equilibrium clearly visible for the measurement at 400 °C. Interestingly, the resistance increase over time observed at 600 °C is linear, which suggests a rate limiting step like the surface reaction $4e^- + V_O^{\bullet\bullet} + O_{2_{(g)}} = O_O + O^{2-}_{(ads)}$[62] to be responsible for this phenomenon. By consuming electrons as well as oxygen vacancies the amount of free charge carriers is reduced by the adsorption of oxygen, thus increasing the measured impedance. We observed the same behavior for the sample S-3.2 as well. The phenomenon increased with temperature, so we call it "aging" within this thesis; it will be discussed in more detail in chapter 5.5.

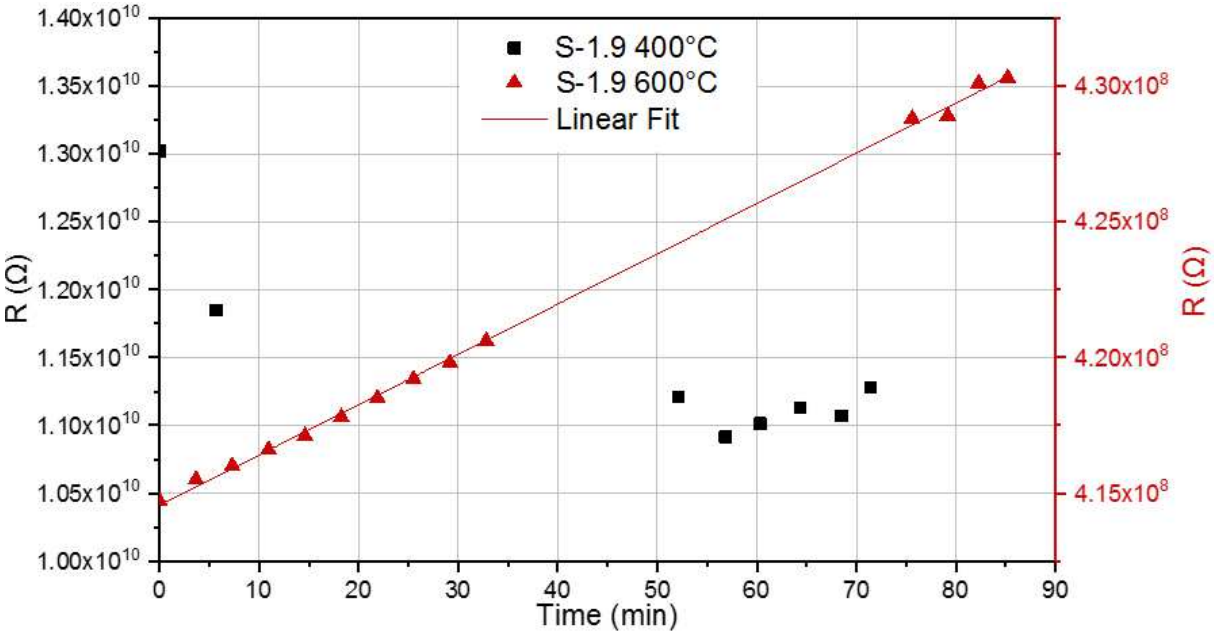

Figure 62: Resistance versus time of measurement plot of S-1.9. At 400 °C a temperature equilibrium is reached after 50 min while the resistance is increasing linearly at 600 °C.

In order to maintain reproducibility of the measurements the diffusion constant of $V_{O_{Surf}}^{\bullet\bullet}$ and surface reaction rate were kept low. Therefore the samples S-1.8 and S-0.5 were heated up to a maximum of 500 °C for the Arrhenius plot. For the electrochemical characterizations at constant temperature, described from chapter 5.3 onwards, the set temperature was chosen to be 350 °C in order to minimalize the thermal impact even more.

- At 400 °C temperature equilibrium is reached within considerably short time.
- At 600 °C there is no temperature equilibrium, but the resistance is increasing linearly with time.
- According to our hypothesis, oxygen vacancies $V_{O_{Surf}}^{\bullet\bullet}$ originally located at the surface as well as electrons are consumed by the surface reaction which leads to the linear resistance increase.

5.1.2 Arrhenius Diagram

The Arrhenius plot (figure 63) shows the effective conductivity of all electrochemically characterized samples in the temperature range 350-600°C. The data points of all samples heated up only once are lying parallel, resulting in very similar activation energies, also presented in figure 64 (b). The repetition measurement S-3.2_rep (violet squares) resulted in significantly lower conductivity compared to the first one (red circles), as well as in a steeper slope. This is related to the aging mentioned above.

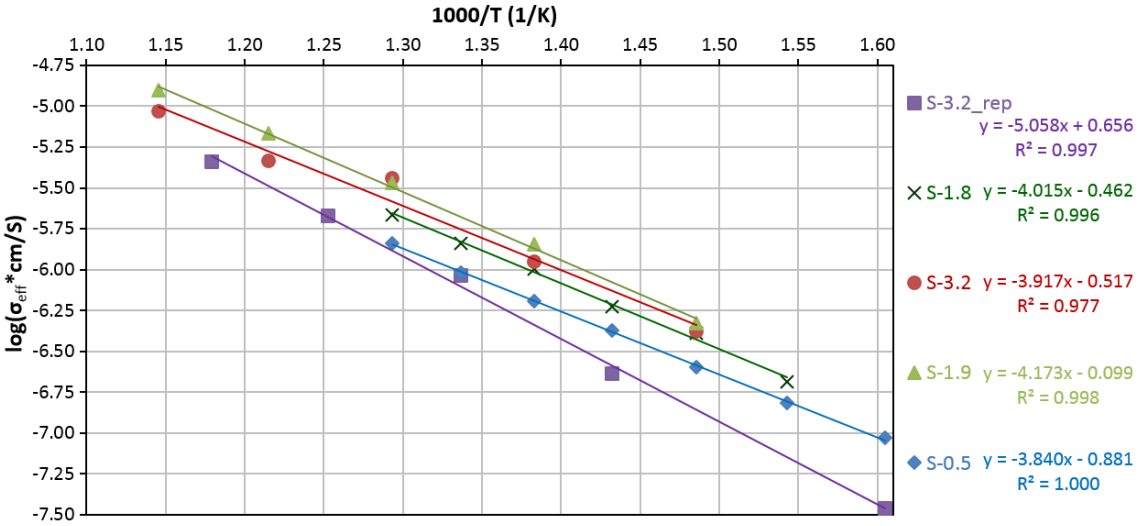

Figure 63: Arrhenius plot of all electrochemically characterized samples showing effective conductivity σ_{eff}.

In Table 18, the resistance R, the effective conductivity σ_{eff}, and the activation energy E_A of the samples presented in the Arrhenius plot are listed. All these parameters were calculated as described in chapter 3.3.5. Due to the limited temperature data available, the values of R and σ_{eff} were calculated using linear intrapolation for 400 °C and linear extrapolation for 350 °C. The activation energies found in literature vary a lot, depending on the sample manufacturing method and measuring conditions.

For $\alpha - Nb_2O_5$ single crystals produced by plasma torch fusion in the dimensions of 6 mm diameter and 1 mm thickness, Chen and Swalin [19] found E_A values of 1.4 eV for a defect controlled mechanism measured above 800 °C and 0.4 eV for a surface reaction controlled mechanism observed below 800 °C (DC measurements). Atta et al. [11] obtained even lower activation energies conducting DC measurements on 1-6 µm thick sputtered Nb_2O_5 films on substrates. They suggest Mott's variable range hopping conduction mechanism with an E_A of 0.16 eV (50-90°C) and the phonon-assisted hopping model given by Mott for 100-210 °C (0.87 eV). Oxygen diffusion measurements on 100 nm thick sputtered samples by Nakamura et al. [45] in the temperature range of 230-380 °C led to an E_A of 1.0 eV, they suggested single atomic jump of oxygen ions mediated via vacancy-like defects.

The reference by Graca et al. [31] for Nb_2O_5 powders prepared by sol-gel method found activation energies around 0.58 eV measuring the conductivity of pressed pellets and concluded that the charge carriers responsible for the DC and AC conduction are not the same.

The activation energy of the repetition measurement fits to the value found by diffusion measurements [45], while the E_A values for the rest of our samples are considerably lower than 1.0 eV but also higher than the reference for powders [31] and the surface reaction controlled mechanism [19].

It is likely that our samples have both the defect controlled and surface reaction controlled conduction mechanism, leading to an activation energy between these two, but in future it would be beneficial to support this with theoretical simulations.

Table 18: Extrapolated (350 °C) and intrapolated (400 °C) R and σ_{eff} values of the electrochemically characterized samples, as well as activation energy E_A.

Sample	$R_{350\,°C}$ [Ω]	σ_{eff} at 350 °C [S/cm]	$R_{400\,°C}$ [Ω]	σ_{eff} at 400 °C [S/cm]	E_A [eV]
S-1.9	3.18E+10	1.64E-07	1.11E+10	4.71E-07	0.827
S-3.2	3.55E+10	1.77E-07	1.49E+10	4.21E-07	0.776
S-3.2_rep	3.10E+11	3.47E-08	4.31E+10	1.45E-07	1.002
S-0.5	1.13E+10	9.31E-08	4.17E+09	2.52E-07	0.761
S-1.8	5.88E+10	1.24E-07	1.78E+10	4.10E-07	0.795

The parameters E_A and σ_{eff} at 400 °C are plotted against the slit width in figure 64. For σ_{eff}, figure 64 (a), following the arrows, we see that aging the sample by heating it up twice (to 600 °C and 575 °C), led to a drop of effective conductivity to almost one third. By reducing the slit width by a factor of six (3.2 → 0.5), σ_{eff} is raised by a factor smaller than two. Considering as well the low difference in σ_{eff} between sample S-1.9 and S-3.2 compared to the slit width, we concluded that the slit width only has a small impact compared to aging at elevated temperatures.

The comparison of S-1.9 to S-1.8 with almost identical slit width but different film properties (S-1.8 had cracks) revealed that also fissures destroying surface continuity have an impact on σ_{eff} as well as on E_A, see figure 64 (b). Interestingly, aging also had an impact on E_A which could not be explained so far within this work.

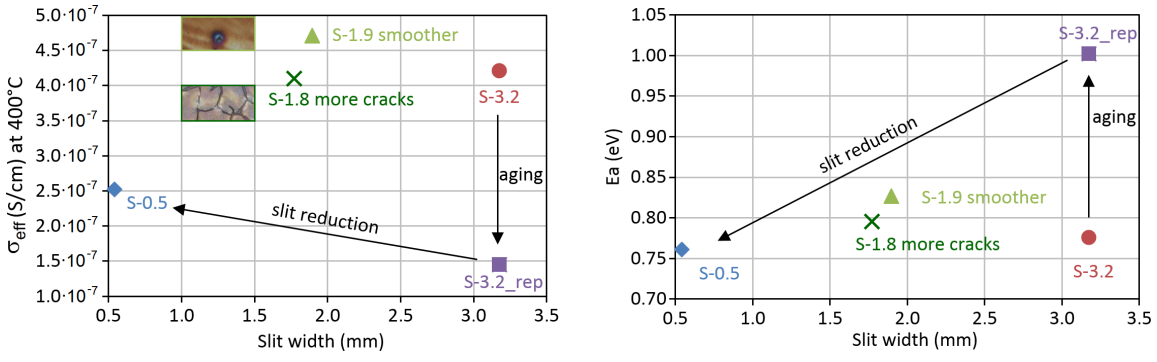

(a) slit width vs. σ_{eff} at 400°C

(b) slit width vs. activation energy

Figure 64: The images illustrate the findings of the Arrhenius diagram: Aging the sample by heating it to temperatures higher than 450 °C reduces σ_{eff} very much, while the slit width only has a minor impact. Fissures reduce σ_{eff} as well as E_A and are therefore dominating the properties more than the slit width.

- Aging and fissures have a higher influence on the effective conductivity than the slit width.
- The samples show similar activation energies that are considerable lower than reporter literature values. Aging significantly increases E_A.

5.2 Comparability and reproducibility of the samples

The samples S-1.9 and S-3.2 were produced simultaneously in the same batch with the intention to produce two identical, comparable samples. Only the slit width was altered to obtain different active surface for the EIS under ambient atmosphere variation and UV-irradiation. However, profilometry revealed differing film thickness and the characterizations in chapter 5.1 unfolded that temperatures above 450 °C led to aging of the sample.

In order to compare these samples, where more than one parameter was varied, the formula for the calculation of σ_{eff} (equation (5)) was used to form the resistance fraction $x = \frac{R_1}{R_2}$ and the fraction of the geometric factor $y = \frac{b_1 \cdot A_2}{b_2 \cdot A_1}$ according to equation (7). In this manner, two dimensionless numbers were acquired.

$$\frac{\sigma_1}{\sigma_2} = \frac{b_1 \cdot A_2}{b_2 \cdot A_1} * \frac{R_2}{R_1} = 1 \tag{7}$$

According to theoretical considerations, those indicators should be equal for samples of the same film quality (homogeneity, fissures, aging). To find out, whether or not this consideration is applicable in the present study, the parameters listed in Table 16 were used to calculate the according fraction for each temperature available. The average values are presented in Table 19.

Table 19: Comparison of the electrochemical samples

Sample name	Resistance fraction x	Geometric factor y	x/y
S-1.8 : S-0.5	4.75±0.37	6.94	0.68±0.07
S-1.9 : S-0.5	2.46±0.33	4.97	0.50±0.09
S-3.2 : S-0.5	3.06±0.49	5.96	0.51±0.12
S-1.9 : S-1.8	0.53±0.07	0.72	0.74±0.14
S-3.2 : S-1.8	0.80±0.15	0.86	0.79±0.24
S-3.2 : S-1.9	1.28±0.19	1.20	1.06±0.24

In the first three rows of Table 19 we see the comparison of the samples with widths bigger than 1.5 mm to the sample with 0.5 mm slit. Consequently, the geometric factor y is very high. The resistance fraction x however is smaller, indicating that the conductivity of the three first mentioned films is higher. This was also presented in the results of the

Arrhenius diagram, figure 64 (a) and could be explained by the fact, that sample S-0.5 was produced by altering sample S-3.2, which was heated to 600 °C twice. Due to the film aging at elevated temperatures discussed above the conductivity of the sample had already decreased before the 0.5 mm width sample was produced.

In line four and five the two samples with more homogeneous films are compared to S-1.8 with more cracks. Consequently, we can see a lower resistance fraction x compared to the geometric factor y. Therefore, the index $^{x}/_{y}$ is below 1, similar to the indices in the first three rows , but not to the same extent.

The last line compares the most similar samples, produced simultaneously in the same batch, with the slit width as the only varying parameter. When the standard deviation is taken into account the two fractions are equal, resulting in an index of exactly 1, thus confirming the theoretical considerations. Hence, inhomogenity, fissures, pores and particles were distributed statistically and the resulting films were indeed comparable.

However, sample S-0.5, used for the following studies, is not directly comparable to S-1.9 anymore, due to the heat treatment (aging). Therefore, relative values like the percentage of $R_{initial}$ or R_{max} are used or reference values are highlighted to compare the trends but no absolute values are used.

Regarding reproducibility, sample S-1.8 derived from a different batch and therefore had different film properties (cracks). Consequently, reproducibility still hast to be improved.

- By introducing the index $^{x}/_{y}$ it was possible to compare the different samples which led to the same conclusions as the arrhenius diagram: S-0.5 lost quality due to aging, S-1.8 is influenced by cracks and S-3.2 is comparable to S-1.9.
- Comparability of absolute values is only possible within the same sample. Due to aging and external influences, the comparison between samples is only possible for relative values and trends.
- Reproducibility is very challenging and can only be achieved, if all parameters during the film production are carefully controlled and fixed to the same parameters.

5.3 Electrochemical characterizations at 350 °C

This chapter describes the influence of p_{O_2} variations and UV-irradiation on the samples S-1.9 and S-0.5 is studied. Measurements under air were performed with the open setup, for p_{O_2} variations the measurement chamber was closed with the lid (closed setup), evacuated to $60 * 10^{-3}\, mbar$ and flushed with nitrogen. The process was repeated twice before the measurement was started. For the experiments under UV-irradiation we used a LED lamp with 365 nm and 11 W, which was positioned on top of the glass window in the lid.

The chronology of the experiments at 350 °C is visible in figures 72-75 in the appendix. In case of sample S-1.9 the measurements under p_{O_2} variation were carried out prior to

studying the aging under air for 1000 min and experiments under UV-irradiation. Sample S-0.5 was first studied under UV and air, only thereafter the p_{O_2} was changed. Therefore, the initial deviation of the film properties due to aging was further enlarged due to the external influences like UV, vacuum and nitrogen in different chronology. Consequently, the absolute values changed, but nevertheless, the studied phenomena always showed the same trends.

- The order of treatments had a significant impact on the conductivity but not on the trends of conductivity changes, which were still clearly visible.

5.3.1 Ambient atmosphere (p_{O_2}) variation

Dry nitrogen (N_2 dry) Figure 65 shows the transient changes in conductivity upon changing the atmosphere to nitrogen. We can see an increase during evacuation and for S-1.9 a pretty rapid regression (during 100 min) to the initial value, measured directly before the N_2 measurement and highlighted as "reference". For S-0.5 we can see that some enhanced conductivity remained for some time. The experiment (1) was stopped after two hours and repeated (2) where the reference (previous experiment under air) was reached after 28 h.

The conductivity increase due to evacuation was expected due to the oxygen partial pressure dependency $\sigma = p_{O_2}^{-0.24\pm0.01}$ described by Greener et al. [33], based on the induction of oxygen vacancies ($V_{O_{Surf}}^{\bullet\bullet}$). The σ_{eff} decrease after flushing with nitrogen, which should not change the oxygen partial pressure, let us conclude that nitrogen adsorption changed the space charge region and hence hindered the surface conduction mechanism.

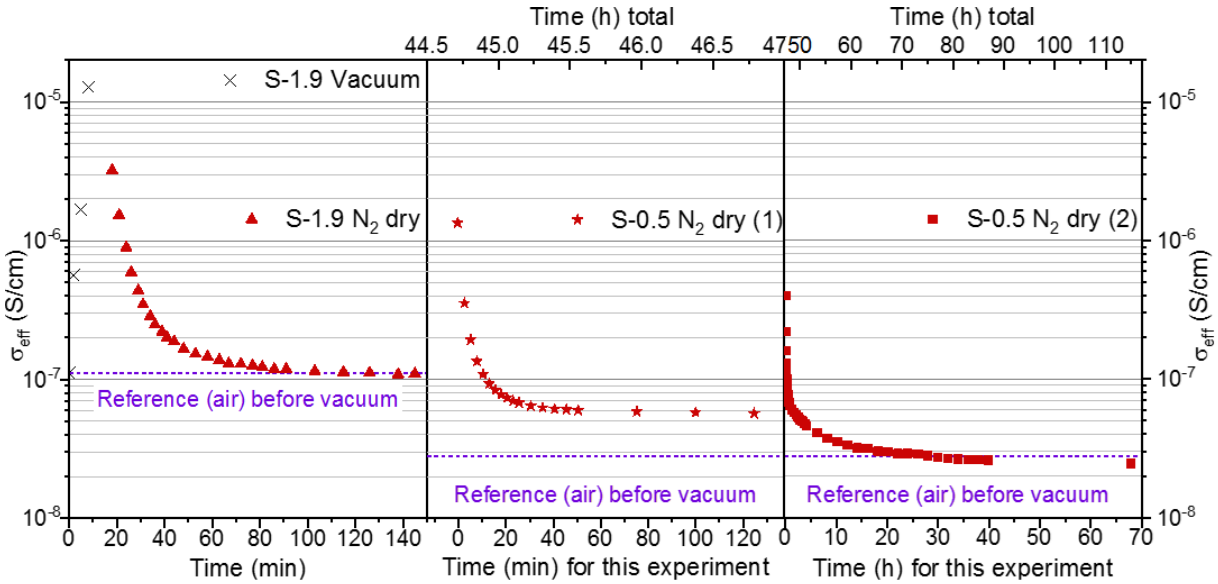

Figure 65: Conductivity rise due to evacuation and relaxation to original value (in ambient air) under N_2 dry atmosphere.

Humidified nitrogen (N_2 wet) In order to create a humidified nitrogen atmosphere (N_2 wet, green markers) without evacuation the nitrogen tube was unplugged and connected to a humidifier, consisting of two gas washing bottles filled with water. For the experiment with humidified nitrogen (N_2 wet after vacuum, blue markers) the measurement chamber was three times evacuated to $60 * 10^{-3}\,mbar$ and afterwards flushed with humidified nitrogen.

In figure 66 the resistance graph of sample S-1.9 is displayed while figure 67 presents the results for S-0.5. For both samples we can see a sudden drop of resistance by one order of magnitude or more, compared to the reference measurements (red markers). The minimum was reached after 10-20 min, then the resistance rose almost linearly, however the reference was not reached even within 2.5 h. By this behavior we see, that humidity enables good surface conductivity while dry nitrogen blocks it.

Upon evacuation, the resistance was reduced further, thus confirming that using vacuum the p_{O_2} is lower than by just flushing with nitrogen. However, the reduction only lasted for roughly 50 min. For S-1.9 the steady increase over time was linear from the beginning, for S-0.5 the data points were curved and after 2 h the trend was almost linear. In this manner, the resistance before vacuum was reached after 85 min respectively 120 min, whereas the process to reach the value after N_2 dry took 16 h.

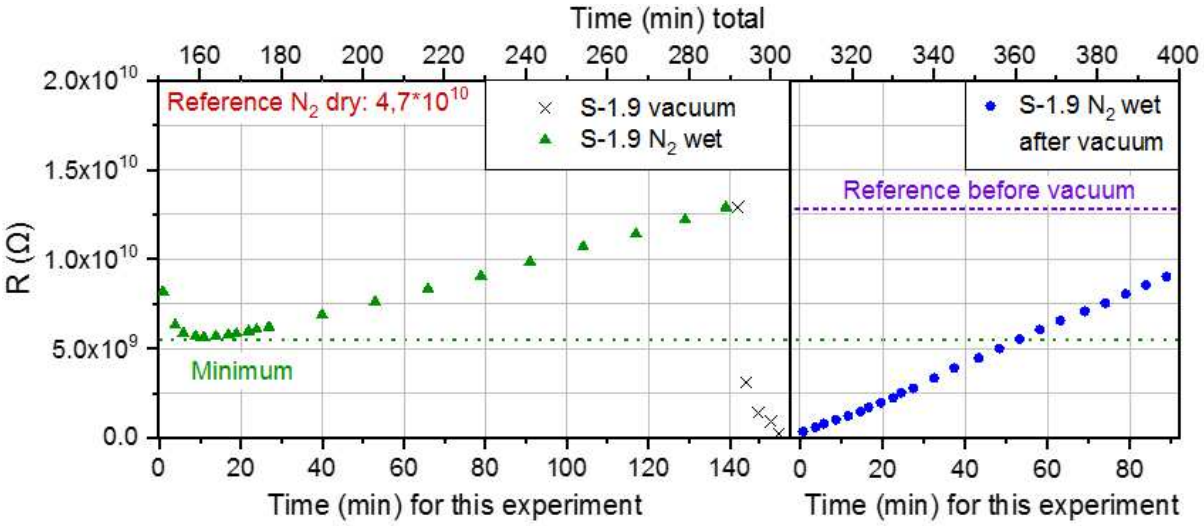

Figure 66: Resistance drop of sample S-1.9 due to changing atmosphere to N_2 wet (green) and relaxation after vacuum (blue).

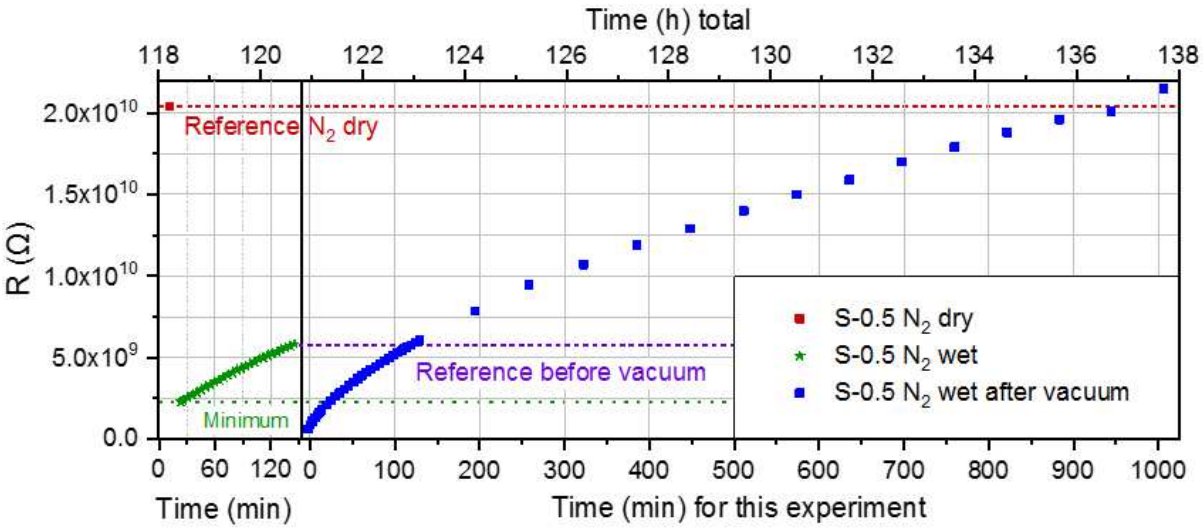

Figure 67: Resistance drop of sample S-0.5 due to changing atmosphere to N_2 wet (green) and relaxation after vacuum (blue).

Compared to the measurements in dry nitrogen atmosphere, where we observed an immediate increase in resistance (within roughly 20 min), the samples treated in humidified nitrogen showed only the long-term effect of steady increase over time. The near-linear nature suggests, that this effect is based on the surface reaction and $V_{O_{Surf}}^{\bullet\bullet}$ diffusion into the bulk material, which were already observed at higher temperatures during the aging process. Obviously, at 350 °C set temperature the aging process is present, it is just so slow that it was not detected in the beginning during the temperature equilibrium studies.

In summary, water plays a key role in the process underlying the effect of sudden conductivity gain and steady versus rapid loss, but could not be investigated further within this thesis.

- Evacuation leads to an increase in conductivity of more than two orders of magnitude.
- In dry nitrogen atmosphere the conductivity drops immediately and regresses to the original value depending on the sample within 2-28 hours
- Humidified nitrogen leads to conductivity increase without evacuation.
- The near-linear behavior suggests that aging is based on the surface reaction and $V_{O_{Surf}}^{\bullet\bullet}$ diffusion.

5.3.2 EIS under UV-irradiation

In order to test the effect of UV-irradiation, a reference measurement under air atmosphere at 350 °C was carried out first in the dark. Then the LED was switched on and spectra were acquired until the change in semicircle size was imperceptible and consequently an equilibrium was reached. Afterwards, the lamp was switched off and spectra were recorded in regular intervals until the initial reference resistance value was reached.

Upon UV irradiation, the resistance decreased from $1.47 \cdot 10^{10}\ \Omega$ to $9.42 \cdot 10^{9}\ \Omega$ and reached a stable value after about 7.5 min, see figure 68 (a).

After turning off the light source, the resistance immediately increased from $8.38 \cdot 10^{9}\ \Omega$ to $9.49 \cdot 10^{9}\ \Omega$, and slowly augmented to the initial value of $1.47 \cdot 10^{10}\ \Omega$ within 139 min, presented in figure 68 (b).

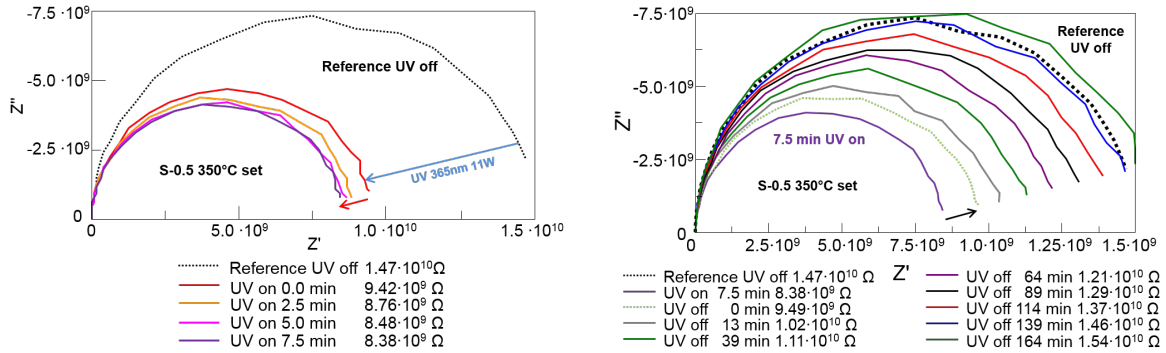

(a) Resistance drop due to UV-irradiation

(b) Relaxation after switching off the UV lamp

Figure 68: Impedance spectra of S-0.5 under UV-irradiation in ambient air

In order to understand what is happening under UV-irradiation, the time constant τ was calculated using the peak frequency ω_p according to equation (8).

$$\tau_n = \frac{1}{2\pi\omega_p} \tag{8}$$

In figure 69 the time constant as well as the absolute resistance and capacitance are plotted versus time to demonstrate the trend of these parameters. The timespan of UV-irradiation is highlighted with a grey box underlying the measurement points. We can see that τ (black) and R (blue) dropped when the UV lamp was switched on and decreased under UV-irradiation. After deactivating the lamp the time constant rose linearly according to the resistance increase over time. Again this linear change is indicative of a surface reaction limited process (see aging, chapter 5.5). The capacitance (green) was decreased by UV-irradiation by a small amount but stayed unaffected by the aging process.

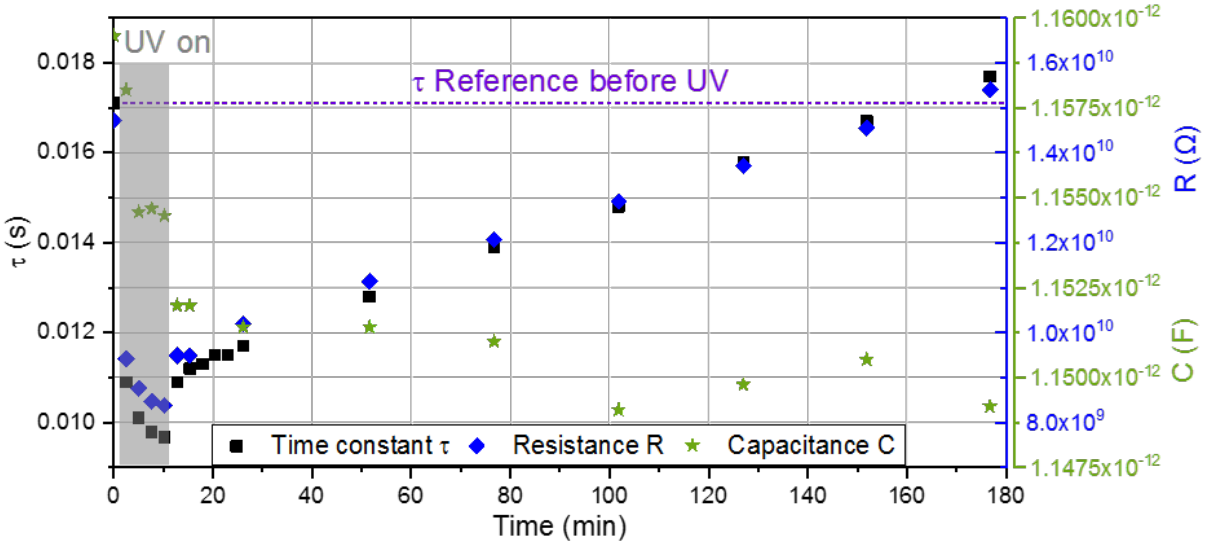

Figure 69: Trend of time constant, resistance and capacitance of S-0.5 under UV-irradiation in ambient air

For sample S-1.9 one experiment under UV-irradiation was performed, S-0.5 was illuminated twice, see figure 70. Depending on the initial value, the conductivity rose immediately after starting the UV lamp by 108 % (S-1.9), respectively 51-56 % (S-0.5). The corresponding values for resistance as well as analysis after which time σ_{eff}^{max} respectively R_{min} was reached are listed in table 20.

Table 20: Resistance drop due to UV-irradiation

	S-1.9 UV		S-0.5 UV (1)		S-0.5 UV (2)	
Initial Resistance	$1.53*10^{11}\,\Omega$	100 %	$1.47*10^{10}\,\Omega$	100 %	$3.76*10^{10}\,\Omega$	100 %
Resistance after 8 min	$5.30*10^{10}\,\Omega$	34.7 %	$8.48*10^{9}\,\Omega$	57.6 %	$2.07*10^{10}\,\Omega$	55.0 %
R_{min} reached after	68 min		experiment aborted		103 min	
Resistance minimum	$3.68*10^{10}\,\Omega$	24.2 %	-	-	$1.56*10^{10}\,\Omega$	41.6 %

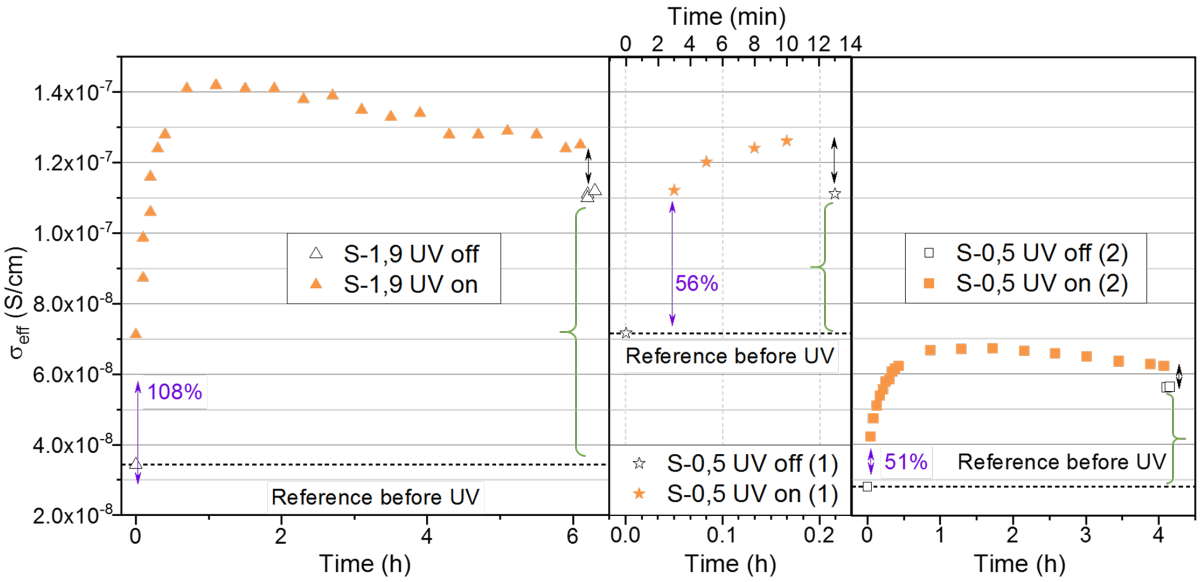

Figure 70: Effect of UV-irradiation (365 nm and 11 W) on sample S-1.9 and S-0.5

The final conductivity maximum was reached after 1-1.5 hours and was 314 % (S-1.9) respectively 140 % (S-0.5) higher than without UV-irradiation. Thus, the UV effect is slower and less effective, in terms of σ_{eff}^{max} achieved, than changing the ambient atmosphere (p_{O_2}). In terms of long-term stability, the main benefit stayed within the measurement period of 4-6 h, only a small linear decrease over time (probably aging) was observed. When the UV lamp was switched off, the resistance rose instantly by a small amount (black arrows) but still lay far below the reference before UV, which is really cool.

It is likely that the UV impact is not completely reversible due to a kinetic effect of the $V_O^{\bullet\bullet}$ diffusion and surface reaction, which could be investigated more detailled by measuring hysteresis curves.

Regarding the underlying mechanism we presume that the space charge is influenced by electron trapping (immediate effect, reversible) as well as inducing $V_O^{\bullet\bullet}$ at the surface or impeding the surface reaction, which is a slower process competing with diffusion and therefore probably responsible for the maximum visible in the graphs. The conductivity gain after switching off the UV lamp compared to the reference before UV (indicated by the green brackets) may arise from a chemical change of the surface termination during exposure to UV light.

- Switching on the UV lamp leads to a leap in conductivity, switching off to a sudden decrease. This reversible process may be due to influencing the space charge by electron trapping and chemical change of the surface termination.
- UV-irradiation leads furthermore to a steady increase in conductivity until a maximum is reached after 1-1.5 h. This slower effect presumably is a competition of inducing $V_{O_{Surf}}^{\bullet\bullet}$ and $V_O^{\bullet\bullet}$ diffusion into the bulk (aging).

5.4 Comparison of parameters influencing σ_{eff}^{max} reversibly

As discussed in the previous chapters. σ_{eff}^{max} could be influenced by changing the p_{O_2} and by UV-irradiation. but not completely reversible. In figure 71 the measurements are plotted in their order of influence on the conductivity. We can see that UV-irradiation has a rather small impact of increasing σ_{eff} by a factor of 1,8 to 4 compared to flushing the measurement chamber with humidified nitrogen (*8-9). Changing the ambient atmosphere by evacuation and flushing with N_2 dry/wet (superposition of both effects) influenced σ_{eff} even more. but less than evacuation itself.

Obviously, filling the measurement chamber with gas, thus covering the sample surface with more molecules than in vacuum, is influencing the space charge region in relation to the humidity content of the gas, while evacuation leads to absence of water and oxygen simultaneously, which could explain the high impact of vacuum. The studied material could potentially be used as a humidity sensor.

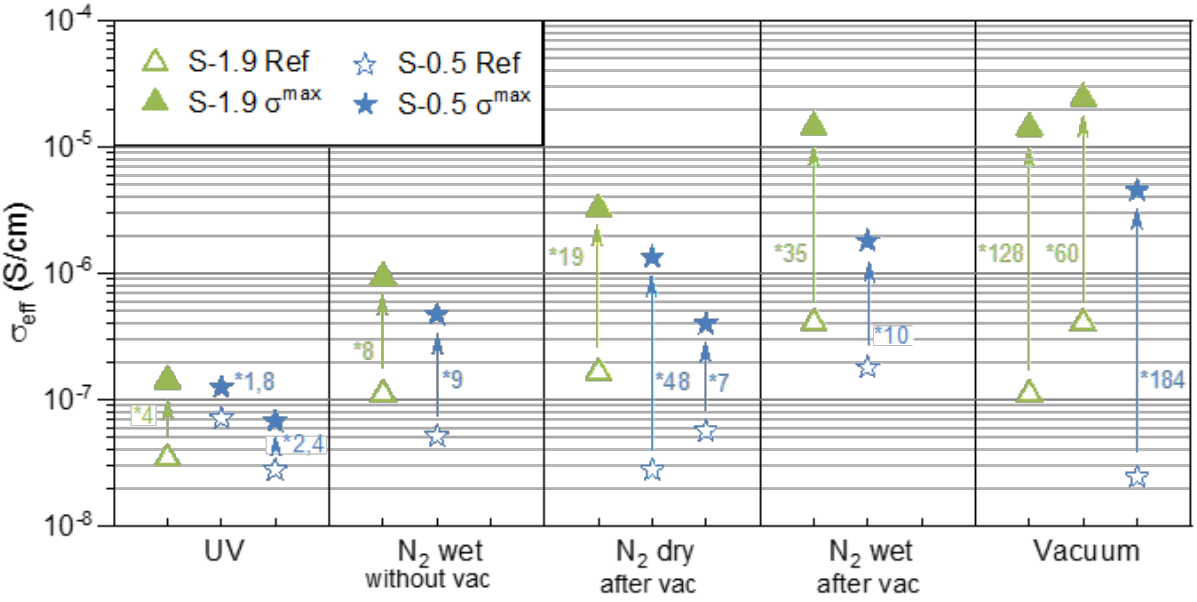

Figure 71: Comparison of parameters influencing σ_{eff}^{max} reversibly

- UV-irradiation and changing the ambient atmosphere to N_2 wet have a rather modest influence on σ_{eff} compared to evacuation.
- The humidity level is connected to σ_{eff}. Maybe the studied material could be used for humidity sensing purposes.

5.5 Aging (time dependent behavior)

In almost every single experiment, a linear increase of resistance over time (aging) could be observed, with slightly differing slope. All the performed experiments are plotted in chronological order in figure 72-75 in the appendix. These graphs showing relative resistance versus time (min) were fitted linearly in order to extract information about the inclination. The slopes converted into percentage per hour are listed in table 21.

Table 21: Calculated slope of resistance-curve [%/h]

Sample	S-1.9	S-0.5 (1)	S-0.5 (2)	S-0.5 (2) long-term
Air after N_2 wet	8.8 %/h		-	
Air directly after UV	-	17.4 %/h	14.1 %/h	
Air 10/6 h after UV	-	9.5 %/h	5.8 %/h	
N_2 dry after 1 h	12.7 %/h	8.0 %/h	11.4 %/h	1.8 %/h
N_2 wet	10.9 %/h	14.1 %/h	-	
N_2 wet after vacuum	18.8 %/h	9.5 %/h	-	
UV	3.17 %/h	-	4.8 %/h	

The interpretation of the data is not trivial due to different experiment chronology. The measurement under air for sample S-1.9 seemed rather uninfluenced two hours after the N_2 wet measurement. Therefore, the slope of 8.8 %/h was regarded as reference. For sample S-0.5 the influence of the UV experiment probably lasted for 10 h (1) respectively 6 h (2), because the slope changed from 17.4/14.1 %/h to 9.5/5.8 %/h. A potential interpretation of this behavior could be that the beneficial impact during UV-irradiation (electron trapping), proposed in chapter 5.3.2, is reversed. According to this hypothesis the slope would be steeper while the induced additional $V_{O_{Surf}}^{\bullet\bullet}$ are quenched, afterwards the normal aging process of $V_O^{\bullet\bullet}$ diffusion into the bulk and surface reaction would take place with flatter slope.

The slopes for nitrogen atmosphere are scattered around the values of air and therefore probably are due to the same aging process. It is interesting to see the slope of the N_2 dry long-term experiment (14-68 h) to be very flat, even below the slope under UV-irradiation. Either the nitrogen atmosphere has a beneficial impact on the aging process or the $V_O^{\bullet\bullet}$ diffusion process already slowed down due to saturation, since the sample was kept at 350 °C already for 63 h at this time or the surface reaction reached maximum adsorption. In future experiments one could vary the oxygen partial pressure and humidiy in more extensive experiments to confirm this hypothesis.

- The aging process was found to increase the resistance by about 10 %/h.
- UV-irradiation decreases the slope to roughly 3-5 %/h.
- After switching off the UV lamp the respective slope was higher for 6-10 h, supposedly the beneficial effect is reversed.
- The long-term N_2 experiment after 14 h suggests a beneficial long-term effect of nitrogen atmosphere or $V_O^{\bullet\bullet}$ saturation in the bulk and therefore slower diffusion or the surface reaction reached maximum adsorption

6 Conclusion & Summary

Thin film optimization The goal of this thesis was to design a model system with dominant solid-vapor interface and negligible contact to the electrode. We chose to produce thin films with mesoporosity and ulta thin walls as well as good film properties concerning cracks, particles and coverage. Therefore, we optimized the precursor solution and parameters until we could synthesize films with only little fissures and particles statistically distributed on glass substrates. The best results were obtained using a P123:Nb ratio of 0.737 and two centrifugation steps prior to spin coating with 2,000-4,000 rpm, procedure is listed in table 15 batch RJ_J; the sample preparation is illustrated in figure 19.

The heat treatment for polymer removal (furnace parameters see table 12) led to a shrinkage in film thickness of $55 \pm 4\,\%$ and by calcination another $13 \pm 8\,\%$. Fissure formation only took place during polymer removal around particles and we did not notice any crack propagation during calcination. We observed worm-like [63] structures for amorphous samples produced at a RH level of 25 %, the calcination process however led to a loss of porosity and grain growth.

Samples for EIS Concerning the electrochemical measurement setups mentioned in chapter 3.3.5, neither sputtered micro-electrodes nor gold paste electrodes were suitable for cross-plane measurements on FTO substrate (figure 23). Therefore, we produced films on isolating substrate for the electrochemical characterization via in-plane measurements (figure 24). Unfortunately, the availability was limited and the surface was super hydrophile, supposedly due to residues of polishing auxiliary agents. The compromise was using sapphire single crystals, thoroughly cleaned twice according to the procedure described in chapter 3.2.1, and skipping the EISA process. In the end we managed to fabricate four samples with different slit width (details described in chapter 4.3.5) on sapphire substrate and characterized them electrochemically .

Electrochemical characterization We performed impedance measurements in the temperature range of 350 °C to 600 °C in order to plot an Arrhenius diagram (figure 63). The spectra showed only one semicircle, thus proving our concept that we produced samples with dominant solid-vapor interface and negligible contact to the electrode. The activation energies for all in-plane samples were calculated using the slope of the Arrhenius diagram and were scattered around 0.78 eV. This values is lower than the E_A of bulk conductivity [33] and oxygen diffusion [45] but higher than pure surface reaction controlled conductivity [19]. We therefore presume to have a mixed defect and surface controlled reaction mechanisms present in our samples.

The analysis of conductivity according to slit width, presented in figure 64, revealed that the slit width only has a minor impact on σ_{eff} compared to film properties (fissures) and aging the sample. The process we called aging is a linear increase of resistance over time rather than a temperature equilibrium found at temperatures above 450 °C as well as at 350 °C in long-term experiments. According to our hypothesis, oxygen vacancies $V_{O_{Surf}}^{\bullet\bullet}$ originally located at the surface as well as electrons are consumed by the surface reaction $4e^- + V_O^{\bullet\bullet} + O_{2_{(g)}} = O_O + O_{(ads)}^{2-}$[62] (adsorption of oxygen). This reduction of

free charge carriers paired with pore collapse and grain growth reducing the surface are leading to the aging phenomenon.

Apart from temperature (aging), we observed and varied three more parameters that affected σ_{eff} (and therefore $V_{O_{Surf}}^{\bullet\bullet}$):

- UV-irradiation (365 nm and 11 W)
- Variation of p_{O_2} and humidity (humidified- versus dry-nitrogen gas atmosphere)
- Vacuum

All of these resulted in an instant increase of σ_{eff} by more than one order of magnitude as a short-term effect, some also had a beneficial long-term impact.

The chronology of the experiments under UV-irradiation, nitrogen atmosphere and vacuum also influenced the results which complicated interpretation and comparability. Despite these obstacles, the same trends were observed for all the different samples studied. Concerning comparability between the samples it was found that $x/y = 1$ (chapter 5.2) is only valid for the samples produced within the same batch. This underlines that reproducibility is very challenging and can only be achieved, if all parameters during the film production are carefully controlled and fixed to the same values.

7 Outlook

This thesis revealed that mesoporous Nb_2O_5 films can be synthesized on sapphire substrate in sufficient quality to conduct EIS measurements leading to interesting results. For further research of the subject we collected some suggestions that should be investigated.

Substrate preparation Our sapphire single crystals in combination with our cleaning procedure were not optimal for the EISA process (still attracting humidity/solvent from the ambient atmosphere). Improvements could be achieved by:

- finding a different non-conductive substrate with more fitting surface properties
- improving the cleaning procedure, e.g. different solvents, abbrasives, burning the substrate for 24 h at 1,000 °C to remove organic residues of polishing auxiliary agents

Mesoporous thin film synthesis The EISA process did not work properly and was therefore skipped, leading to a non ordered mesoporous film. Porosity was lost during sintering (due to inducing crystallinity). Therefore, we suggest to:

- study the EISA process on sapphire in order to optimize the ordered mesoporous structure of the thin film
- replace P123 by a polymer building bigger mesopores like Poly(isoprene)-*block*-poly(styrene)-*block*-poly(ethylene oxide) (ISO) [24]
- incorporate a carbon filling step prior to calcination to prevent pore collapse and obtain crystalline mesoporous films
- improve the control of all parameters during film synthesis in order to obtain reproducible samples for electrochemical characterization

Characterization In terms of possible characterizations a wide variety would be interesting, including:

- compare the shrinkage (figure 35) of the mesoporous films to Nb_2O_5 films produced via the same sol gel process excluding the polymer (P123)
- study if the fissures heal or extend upon temperature dependent measurements
- check the actual porosity of the mesoporous films, e.g with BET
- test the long-term stability of the samples, e.g. repeat the same measurement multible times with some days or a week time inbetween
- study the p_{O_2} variation (air/vacuum, air/N_2) more closely
- measure hysteresis curves
- conduct in-situ optical measurements e.g. raman

- test if the defects induced by UV or vacuum can be "frozen" by cooling to room temperature and measurements after heating up again
- study adsorbates at the surface
- investigate on the role of humidity
- conduct measurements of humidified air with and without UV-irradiation
- investigate on the hypothesis that the $V_O^{\bullet\bullet}$ diffusion process slows down
- support the theory of defect controlled and surface reaction controlled conduction mechanism with theoretical simulations

Experiment chronology

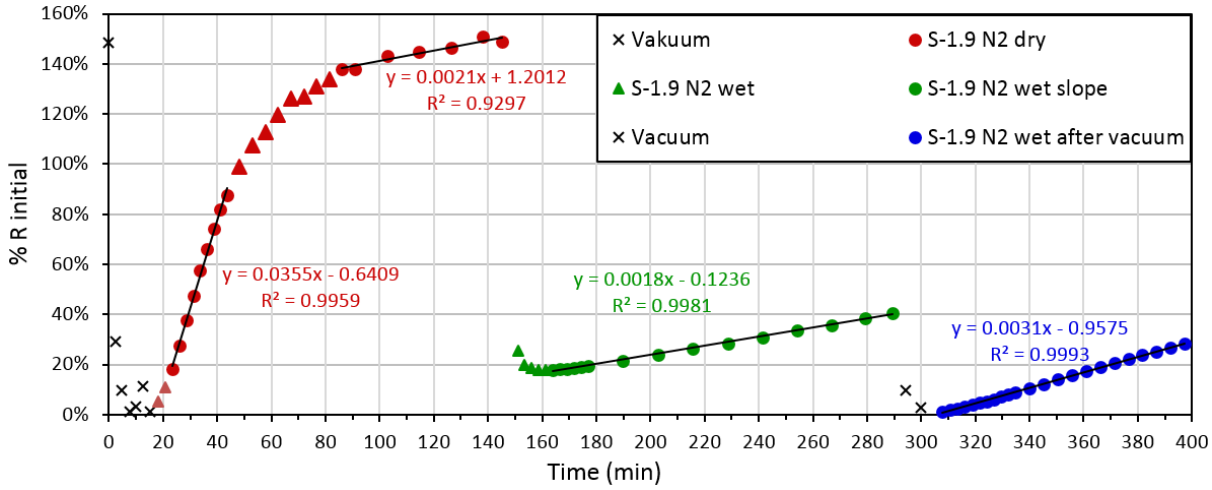

Figure 72: Chronology of the experiments performed on sample S-1.9 as well as linear fits for the slopes.

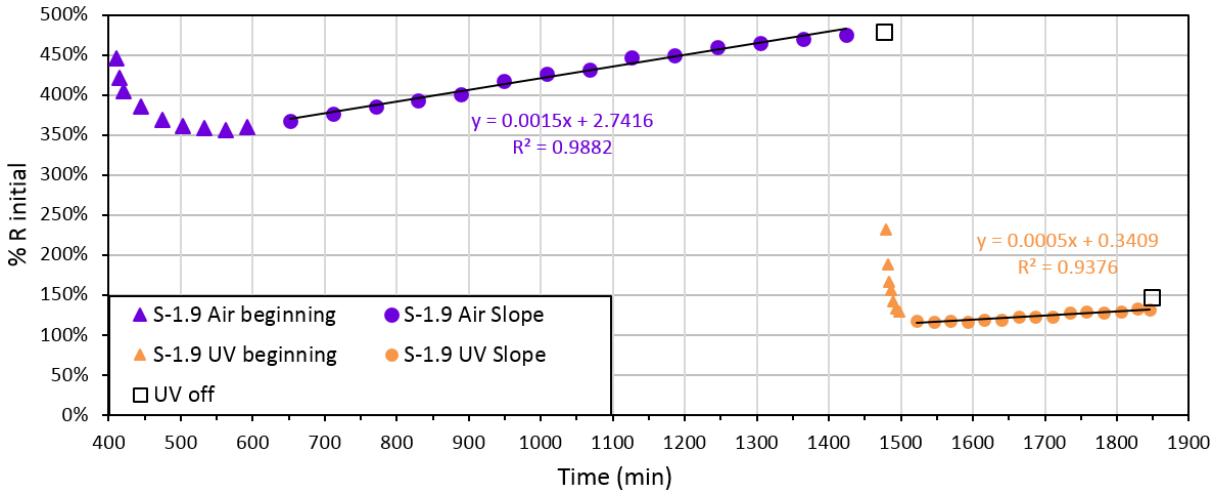

Figure 73: Chronology of the experiments performed on sample S-1.9 as well as linear fits for the slopes.

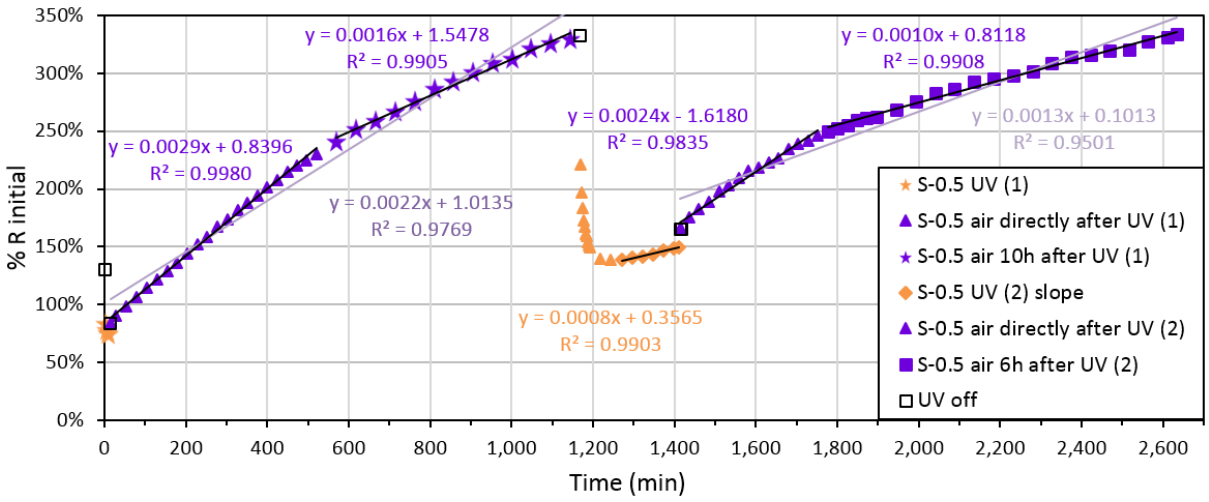

Figure 74: Chronology of the experiments performed on sample S-0.5 as well as linear fits for the slopes.

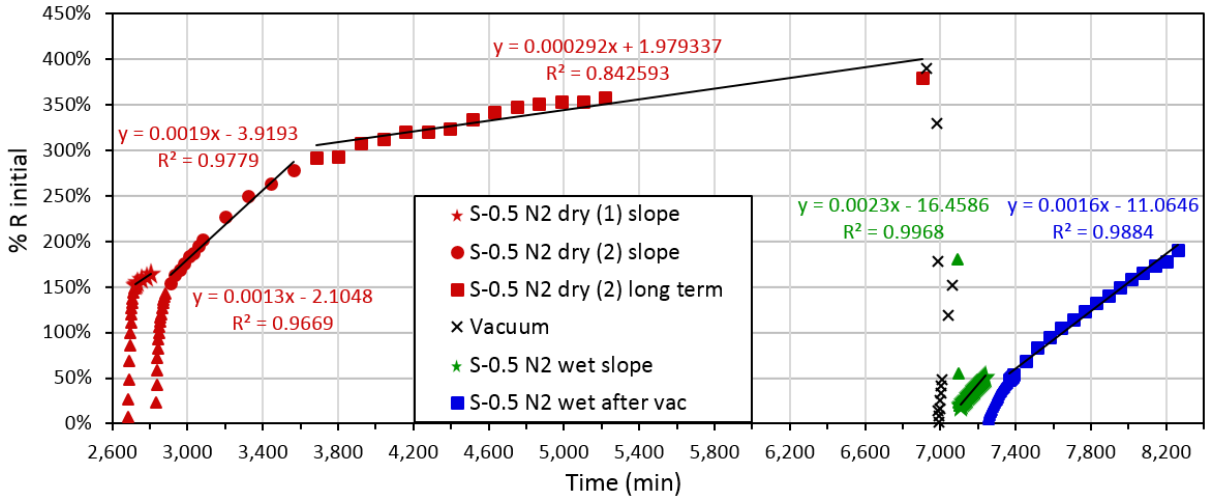

Figure 75: Chronology of the experiments performed on sample S-0.5 as well as linear fits for the slopes.

List of Figures

References

[1] Converter measurement unit conversion: tonne of oil equivalent. https://www.convertunits.com/info/tonne+of+oil+equivalent. (Accessed 2019-05-21). 1.1

[2] impedance, z. In *IUPAC Compendium of Chemical Terminology*. IUPAC. 2.4

[3] Merriam-webster dictionary. (Accessed 2019-07-19). 1.4

[4] Sustainable development goal 7. https://sustainabledevelopment.un.org/sdg7. (Accessed 2019-05-23). 1.1

[5] Sustainable development goals. https://sustainabledevelopment.un.org/sdgs. (Accessed 2019-05-03). 1, 4, 7

[6] Thermo scientific slides. https://www.msg-praxisbedarf.de/. (Accessed 2019-05-22). 4

[7] World energy outlook, total primary energy demand in the sustainable develomente scenario. https://www.iea.org/weo/. (Accessed 2019-06-05). 5, 7

[8] Meet the doughnut: the new economic model that could help end inequality. "https://www.weforum.org/agenda/2017/04/the-new-economic-model-that-could-end-inequality-doughnut", Apr. 2017. (Accessed 2019-05-03). 3b

[9] Sputter coater principles. https://www.emsdiasum.com/microscopy/technical/datasheet/, 2019. (Accessed 2019-05-22). 3.2.6

[10] Aegerter, M. A. Sol–gel niobium pentoxide: A promising material for electrochromic coatings, batteries, nanocrystalline solar cells and catalysis. *Solar Energy Materials and Solar Cells 68*, 3-4 (jun 2001), 401–422. 15, 7

[11] Atta, A., El-Nahass, M., Hassanien, A., Elsabawy, K. M., El-Raheem, M. A., Alhuthali, A., Alomariy, S. E., and Algamdi, M. Effect of thermal annealing on structural, optical and electrical properties of transparent nb2o5 thin films. *Materials Today Communications 13* (dec 2017), 112–118. 5.1.2

[12] Ayudhya, S. K. N., Soottitantawat, A., Praserthdam, P., and Satayaprasert, C. Effect of aging on the properties of mesoporous niobium oxide. *Materials Chemistry and Physics 110*, 2-3 (aug 2008), 387–392. 4.1

[13] Barsukov, Y., Barsoukov, E., and Macdonald, J. R. *Impedance Spectroscopy: Theory, Experiment, and Applications*, 2nd edition ed. A John Wiley & Sons, Inc., 2005. 2.4.1

[14] Bornside, D. E., Macosko, C. W., and Scriven, L. E. Spin coating: One-dimensional model. *Journal of Applied Physics 66*, 11 (dec 1989), 5185–5193. 3.2.3

[15] Bourzac, K. News feature: Liquid sunlight. *Proceedings of the National Academy of Sciences 113*, 17 (apr 2016), 4545–4548. 1.2

[16] Brauer, G. Die oxyde des niobs. *Zeitschrift fi¿œr anorganische und allgemeine Chemie 248*, 1 (sep 1941), 1–31. 2.2

[17] Brinker, C. J., Lu, Y., Sellinger, A., and Fan, H. Evaporation-induced self-assembly: Nanostructures made easy. *Advanced Materials 11*, 7 (may 1999), 579–585. 2.1.1

[18] Bruker Corporation. *DektakXT Stylus Profilometer User Manual*. 2650 East Elvira RoadTucson, Arizona 85756, Mar. 2011. 3.3.4

[19] Chen, W., and Swalin, R. Studies on the defect structure of -nb2o5. *Journal of Physics and Chemistry of Solids 27*, 1 (jan 1966), 57–64. 2.3.1, 5.1.2, 6

[20] Crabtree, G. W., and Lewis, N. S. Solar energy conversion. *Physics Today 60*, 3 (mar 2007), 37–42. 1.1, 7, 7

[21] Dalle, K. E., Warnan, J., Leung, J. J., Reuillard, B., Karmel, I. S., and Reisner, E. Electro- and solar-driven fuel synthesis with first row transition metal complexes. *Chemical Reviews 119*, 4 (feb 2019), 2752–2875. 8, 7

[22] David B. Williams, C. B. C. *Transmission Electron Microscopy*. Springer-Verlag New York Inc., 2009. 3.3.1

[23] Davis, M. E. Ordered porous materials for emerging applications. *Nature 417*, 6891 (jun 2002), 813–821. 2.1

[24] Doerr, T. S., Deilmann, L., Haselmann, G., Cherevan, A., Zhang, P., Blaha, P., de Oliveira, P. W., Kraus, T., and Eder, D. Ordered mesoporous TiO2 gyroids: Effects of pore architecture and nb-doping on photocatalytic hydrogen evolution under UV and visible irradiation. *Advanced Energy Materials 8*, 36 (nov 2018), 1802566. 2.1.1, 7

[25] Fan, J., Boettcher, S. W., Tsung, C.-K., Shi, Q., Schierhorn, M., and Stucky, G. D. Field-directed and confined molecular assembly of mesostructured materials: Basic principles and new opportunities†. *Chemistry of Materials 20*, 3 (feb 2008), 909–921. 2.1.1

[26] FUJISHIMA, A., ZHANG, X., and TRYK, D. TiO2 photocatalysis and related surface phenomena. *Surface Science Reports 63*, 12 (dec 2008), 515–582. 1.2

[27] Gabbott, P., Ed. *Principles and Applications of Thermal Analysis*. Wiley-Blackwell, 2008. 3.3.2

[28] Gao, L., and McCarthy, T. J. How wenzel and cassie were wrong. *Langmuir 23*, 7 (mar 2007), 3762–3765. 3.3.3

[29] Goldstein, J., Newbury, D., Joy, D., Lyman, C., Echlin, P., Lifshin, E., Sawyer, L., and Michael, J. *Scanning Electron Microscopy and X-Ray Microanalysis*. Springer Science+Business Media New York, 2003. 3.2.6

[30] Goodhew, P. J., Humphreys, J., and Beanland, R. *Electron Microscopy and Analysis, Third Edition*. Crc Press, 2000. 3.3.1

[31] Graça, M., Meireles, A., Nico, C., and Valente, M. Nb2o5 nanosize powders prepared by sol–gel – structure, morphology and dielectric properties. *Journal of Alloys and Compounds 553* (mar 2013), 177–182. 5.1.2

[32] Graetzel, M. Solar energy conversion by dye-sensitized photovoltaic cells. *Inorganic Chemistry 44*, 20 (oct 2005), 6841–6851. 2.1

[33] Greener, E. H., Whitmore, D. H., and Fine, M. E. Electrical conductivity of near-stoichiometric -nb2o5. *The Journal of Chemical Physics 34*, 3 (mar 1961), 1017–1023. 2.2, 2.3.1, 5.3.1, 6

[34] Gust, D., Moore, T. A., and Moore, A. L. Solar fuels via artificial photosynthesis. *Accounts of Chemical Research 42*, 12 (dec 2009), 1890–1898. 1.2

[35] Haber, J. Manual on catalyst characterization. *Pure and Applied Chemistry 63*, 9 (1991), 1227–1246. 2.1

[36] Hashemzadeh, F., Rahimi, R., and Ghaffarinejad, A. Mesoporous nanostructures of nb2o5 obtained by an EISA route for the treatment of malachite green dye-contaminated aqueous solution under UV and visible light irradiation. *Ceramics International 40*, 7 (aug 2014), 9817–9829. 3.2.4, 4.1

[37] Hornak, J. P., Ed. *Encyclopedia of Imaging Science and Technology*. John Wiley & Sons, Inc., jan 2002. 3.3.1

[38] Huber, T., Opitz, A., Kubicek, M., Hutter, H., and Fleig, J. Temperature gradients in microelectrode measurements: Relevance and solutions for studies of SOFC electrode materials. *Solid State Ionics 268* (dec 2014), 82–93. 1.3, 3.3.5, 25, 5.1.1, 7

[39] Ismail, A. A., and Bahnemann, D. W. Mesoporous titania photocatalysts: preparation, characterization and reaction mechanisms. *Journal of Materials Chemistry 21*, 32 (2011), 11686. 2.1

[40] Kroeger, F., and Vink, H. Relations between the concentrations of imperfections in crystalline solids. In *Solid State Physics*. Elsevier, 1956, pp. 307–435. 2.3

[41] Lee, B., Lu, D., Kondo, J. N., and Domen, K. Three-dimensionally ordered mesoporous niobium oxide. *Journal of the American Chemical Society 124*, 38 (sep 2002), 11256–11257. 4.1, 4.2

[42] Lee, J., Orilall, M. C., Warren, S. C., Kamperman, M., DiSalvo, F. J., and Wiesner, U. Direct access to thermally stable and highly crystalline mesoporous transition-metal oxides with uniform pores. *Nature Materials 7*, 3 (jan 2008), 222–228. 2.1.1

[43] Li, Y., Tan, B., and Wu, Y. Mesoporous Co3O4 nanowire arrays for lithium ion batteries with high capacity and rate capability. *Nano Letters 8*, 1 (jan 2008), 265–270. 2.1

[44] Macdonald, J. R. Impedance spectroscopy. *Annals of Biomedical Engineering 20*, 3 (may 1992), 289–305. 2.4.1

[45] Nakamura, R., Toda, T., Tsukui, S., Tane, M., Ishimaru, M., Suzuki, T., and Nakajima, H. Diffusion of oxygen in amorphous al2o3, ta2o5, and nb2o5. *Journal of Applied Physics 116*, 3 (jul 2014), 033504. 5.1.2, 6

[46] Network, G. F. NFA 2019 Free Public Data Set. (Access 2019-05-03). 1, 1, 7

[47] Nico, C., Monteiro, T., and Graça, M. Niobium oxides and niobates physical properties: Review and prospects. *Progress in Materials Science 80* (jul 2016), 1–37. 15, 2.2, 4, 7

[48] Orilall, M. C., and Wiesner, U. Block copolymer based composition and morphology control in nanostructured hybrid materials for energy conversion and storage: solar cells, batteries, and fuel cells. *Chem. Soc. Rev. 40*, 2 (2011), 520–535. 12, 7

[49] Ostwald, W. Definition der katalyse. *Zeitschrift für physikalische Chemie 15* (1894), 705–706. 1.2

[50] Petkovich, N. D., and Stein, A. Controlling macro- and mesostructures with hierarchical porosity through combined hard and soft templating. *Chem. Soc. Rev. 42*, 9 (2013), 3721–3739. 2.1.1, 10, 2.1.1, 2.1.1, 13, 2.1.1, 7

[51] Ravelli, D., Dondi, D., Fagnoni, M., and Albini, A. Photocatalysis. a multi-faceted concept for green chemistry. *Chemical Society Reviews 38*, 7 (2009), 1999. 1.2, 9, 7

[52] Raworth, K. A safe and just space for humanity: Can we live within the doughnut. *Oxfam Policy Pract. Clim. Change Resil 8* (01 2012). 1, 3a

[53] REN21. Total technical renewable energy potential in ej/yr for 2050, 2017. Paris, REN21 Secretariat. 1.1, 6, 7

[54] Ristić, M., Popović, S., and Musić, S. Sol–gel synthesis and characterization of nb2o5 powders. *Materials Letters 58*, 21 (aug 2004), 2658–2663. 4.2.1

[55] Rockstroem, J., Steffen, W., Noone, K., Persson, Ã., III, F. S. C., Lambin, E., Lenton, T. M., Scheffer, M., Folke, C., Schellnhuber, H., Nykvist, B., Wit, C. A. D., Hughes, T., van der Leeuw, S., Rodhe, H., Soerlin, S., Snyder, P. K., Costanza, R., Svedin, U., Falkenmark, M., Karlberg, L., Corell, R. W., Fabry, V. J., Hansen, J., Walker, B., Liverman, D., Richardson, K., Crutzen, P., and Foley., J. Planetary boundaries: Exploring the safe operating space for humanity. *Ecology and Society 14(2)* (2009). 1

[56] Steffen, W., Richardson, K., Rockstrom, J., Cornell, S. E., Fetzer, I., Bennett, E. M., Biggs, R., Carpenter, S. R., de Vries, W., de Wit, C. A., Folke, C., Gerten, D., Heinke, J., Mace, G. M., Persson, L. M., Ramanathan, V., Reyers, B., and Sorlin, S. Planetary boundaries: Guiding human development on a changing planet. *Science 347*, 6223 (jan 2015), 1259855–1259855. 1, 2, 7

[57] Stokes, R. H., and Robinson, R. A. Standard solutions for humidity control at 25° c. *Industrial & Engineering Chemistry 41*, 9 (sep 1949), 2013–2013. 4.2.5, 4.2.6

[58] Susan R. Mikkelsen, E. C. Centrifugation methods. In *Bioanalytical Chemistry*. John Wiley & Sons, Inc., 2004, pp. 247–267. 3.2.2

[59] Tilley. *Defects in Solids*. John Wiley & Sons, 2008. 2.3, 16, 2.3, 17, 7

[60] Wanka, G., Hoffmann, H., and Ulbricht, W. Phase diagrams and aggregation behavior of poly(oxyethylene)-poly(oxypropylene)-poly(oxyethylene) triblock copolymers in aqueous solutions. *Macromolecules 27*, 15 (jul 1994), 4145–4159. 14, 7

[61] Warren, S. C., and Wiesner, U. Self-assembled ordered mesoporous metals. *Pure and Applied Chemistry 81*, 1 (jan 2009), 73–84. 11, 2.1.1, 7

[62] Williams, D. E., and Rahman, A. Z. M. S. Metal-oxide-based gas sensors 73. In *Reference Module in Materials Science and Materials Engineering*. Elsevier, 2017. (document), 5.1.1, 6

[63] Ye, L., Xie, S., Yue, B., Qian, L., Feng, S., Tsang, S. C., Li, Y., and He, H. Crystalline three-dimensional cubic mesoporous niobium oxide. *CrystEngComm 12*, 2 (2010), 344–347. 4.1, 4.2.6, 42, 4.2.6, 6, 7

[64] Yuan, L., and Guliants, V. V. Mesoporous niobium oxides with tailored pore structures. *Journal of Materials Science 43*, 18 (sep 2008), 6278–6284. 4.1

[65] Zhang, B., and Sun, L. Artificial photosynthesis: opportunities and challenges of molecular catalysts. *Chemical Society Reviews 48*, 7 (2019), 2216–2264. 1.2